

HIGH PERFORMANCE FOCAL PLANE ARRAY TECHNOLOGIES FROM  
SHORT TO LONG WAVELENGTH INFRARED BANDS

A THESIS SUBMITTED TO  
THE GRADUATE SCHOOL OF NATURAL AND APPLIED SCIENCES  
OF  
MIDDLE EAST TECHNICAL UNIVERSITY

BY

YETKİN ARSLAN

IN PARTIAL FULFILLMENT OF THE REQUIREMENTS  
FOR  
THE DEGREE OF DOCTOR OF PHILOSOPHY  
IN  
ELECTRICAL AND ELECTRONICS ENGINEERING

SEPTEMBER 2014



Approval of the thesis:

**HIGH PERFORMANCE FOCAL PLANE ARRAY TECHNOLOGIES FROM  
SHORT TO LONG WAVELENGTH INFRARED BANDS**

submitted by **YETKİN ARSLAN** in partial fulfillment of the requirements for the degree of  
**Doctor of Philosophy in Electrical and Electronics Engineering Department, Middle East  
Technical University** by,

Prof. Dr. Canan ÖZGEN

Dean, Graduate School of **Natural and Applied Sciences**

\_\_\_\_\_

Prof. Dr. Gönül TURHAN SAYAN

Head of Department, **Electrical and Electronics Engineering**

\_\_\_\_\_

Prof. Dr. Cengiz BEŞİKCİ

Supervisor, **Electrical and Electronics Engineering Dept., METU**

\_\_\_\_\_

**Examining Committee Members:**

Prof. Dr. Nevzat G. GENÇER

Electrical and Electronics Engineering Dept., METU

\_\_\_\_\_

Prof. Dr. Cengiz BEŞİKCİ

Electrical and Electronics Engineering Dept., METU

\_\_\_\_\_

Prof. Dr. Mehmet PARLAK

Physics Dept., METU

\_\_\_\_\_

Prof. Dr. Yüksel ERGÜN

Physics Dept., Anadolu University

\_\_\_\_\_

Assist. Prof. Dr. Serdar KOCAMAN

Electrical and Electronics Engineering Dept., METU

\_\_\_\_\_

Date: 05.09.2014

**I hereby declare that all information in this document has been obtained and presented in accordance with academic rules and ethical conduct. I also declare that, as required by these rules and conduct, I have fully cited and referenced all material and results that are not original to this work.**

Name, Last name : Yetkin ARSLAN

Signature :

## ABSTRACT

### HIGH PERFORMANCE FOCAL PLANE ARRAY TECHNOLOGIES FROM SHORT TO LONG WAVELENGTH INFRARED BANDS

ARSLAN, Yetkin

Ph.D., Department of Electrical and Electronics Engineering

Supervisor: Prof. Dr. Cengiz BEŞİKCI

Sept. 2014, 182 pages

This thesis work covers the development of three different state of the art infrared sensor technologies: quantum well infrared photodetectors (QWIPs), HgCdTe sensors and extended InGaAs photodetectors. QWIP is the leading member of the quantum structure infrared photodetector family providing excellent uniformity and stability with field proven performance. The utilization of the InP/In<sub>0.48</sub>Ga<sub>0.52</sub>As multi-quantum well structure (instead of the standard AlGaAs/GaAs material system) for the implementation of large format (640x512 format, 25 µm pitch) long wavelength infrared (LWIR) QWIP focal plane arrays (FPAs) and the careful design of the detector structure yielded a quantum efficiency as high as 31% in the diffraction grating coupled FPA pixels, which is almost an order of magnitude larger than the pixel quantum efficiency of a standard AlGaAs/GaAs QWIP FPA. The noise equivalent temperature difference of the FPA with  $f/2$  optics is 30 mK with an integration time as low as 1 ms at 67 K. Above 20%

conversion efficiency of the FPA allows desirable thermal imaging with integration times as low as several hundred  $\mu\text{s}$ . The results demonstrate that the main limitations of the standard QWIP technology can be overcome through the utilization of alternative material systems and proper FPA processing techniques.

HgCdTe is the material of choice for high-end infrared imaging systems, offering high flexibility and still unmatched performance. In this work, complete production cycles for photovoltaic HgCdTe focal plane arrays are developed starting from the molecular beam epitaxy (MBE) growth of the material. The dynamic resistance-area product of the developed LWIR HgCdTe FPA ( $\sim 10 \mu\text{m}$  cut-off wavelength) pixels is as high as  $\sim 2000 \Omega\text{-cm}^2$  at 78 K. The peak detectivity of the pixels is as high as  $1.28 \times 10^{11} \text{ cm}\sqrt{\text{Hz}}/\text{W}$  with  $f/l$  optics which is comparable to that of the best LWIR HgCdTe detectors with similar cut-off wavelength.

We have also developed the procedures to implement a solid source (MBE) grown large format (640x512) extended short wavelength infrared (SWIR)  $\text{In}_{0.83}\text{Ga}_{0.17}\text{As}$  sensor with desirable performance at both pixel and FPA levels. The FPA pixels in the mesa structure grown in our laboratory on a graded AlInAs buffer layer with  $2.65 \mu\text{m}$  300 K cut-off wavelength exhibited 300 and 200 K peak detectivities as high as  $\sim 2.5 \times 10^{10}$  and  $\sim 1 \times 10^{12} \text{ cm}\sqrt{\text{Hz}}/\text{W}$  which are both equivalent to the theoretical limits set by the Johnson noise of the detector. Dark current analysis of the pixels displayed no considerable tunneling component with the dark current being dominated by generation-recombination and shunt leakage mechanisms above 200 K up to a reverse bias voltage of 3 V. Moreover, the noise measurements displayed no  $1/f$  noise in the FPA pixels. In spite of the large lattice mismatch, the FPA yielded very good response linearity, as well as impressively good responsivity nonuniformity and pixel operability of 5.5 % and 99.8 %, which are among the best results reported for extended InGaAs FPAs with similar cut-off wavelengths. These results demonstrate the feasibility of the InGaAs SWIR FPA technology with extended cut-off wavelengths as high as  $\sim 2.7 \mu\text{m}$  as an alternative to SWIR HgCdTe FPAs with higher production cost.

**Keywords:** Infrared Photodetectors, Focal Plane Arrays,

## ÖZ

### KISADAN UZUN DALGA BOYU KIZILÖTESİ BANDINA KADAR YÜKSEK PERFORMANSLI ODAK DÜZLEM DİZİNİ TEKNOLOJİLERİ

ARSLAN, Yetkin

Doktora, Elektrik ve Elektronik Mühendisliği Bölümü

Tez Yöneticisi: Prof. Dr. Cengiz BEŞİKCİ

Eylül 2014, 182 sayfa

Bu tez çalışması üç değişik modern kızılötesi sensör teknolojisinin geliştirilmesini içermektedir: Kuantum Kuyulu Kızılötesi Fotodedektörler (KKKF), HgCdTe sensörler ve uzatılmış InGaAs fotodedektörler. Standart AlGaAs/GaAs malzeme sistemi yerine InP/In<sub>0.48</sub>Ga<sub>0.52</sub>As çoklu kuantum kuyulu yapılarının geniş formatlı (640x512 format, 25 µm piksel adımı) uzun dalga boyu kızılötesi (UDK) KKKF odak düzlem dizinlerinin (ODD) gerçekleştirilmesinde kullanılması ve dedektör yapısının dikkatli tasarımı, kırınım ızgaralı ODD piksellerinde %31 gibi bir yüksek bir kuantum verimliliğiyle sonuçlanmıştır ki bu değer standart AlGaAs/GaAs KKKF ODD'lerinin piksel kuantum verimliliğinden neredeyse 10 kat yüksektir. ODD'nin gürültü eşdeğer sıcaklık farkı  $f/2$  optik açıklık ve 1 ms kadar düşük bir entegrasyon süresiyle 67 K çalışma sıcaklığında 30 mK olmuştur. ODD'nin sağladığı %20'den fazla çevrim kazancı yüz mikrosaniyeler mertebesinde düşük entegrasyon süreleriyle cazip termal görüntüleme yapılmasına elvermektedir. Sonuçlar göstermektedir ki standart KKKF teknolojisinin temel

kısıtlamaları alternatif malzeme sistemlerinin kullanılması ve doğru ODD üretim tekniklerinin kullanılmasıyla aşılabilecektir.

HgCdTe gelişmiş kızılötesi görüntüleme sistemleri için tercih edilen, yüksek esneklik ve rakipsiz performans sunan malzemedir. Bu çalışmada fotovoltik HgCdTe ODK'larının malzemenin moleküler ışın epitaksisi (MBE) yöntemiyle üretilmesiyle başlayan üretim döngüsü baştan sonra geliştirilmiştir. Geliştirilen UDK HgCdTe ODD'lerinin (~10 µm kesim dalgaboyuna sahip) dinamik direnç-alan çarpımları 78 K sıcaklıkta ~2000 Ω-cm<sup>2</sup> kadar yüksek olmuştur. Piksellerin  $f/I$  optik açıklıkla tepe dedektivite değerleri  $1.28 \times 10^{11}$  cm $\sqrt{\text{Hz}}/W$  kadar yüksek olmuştur ki bu değerler benzer kesim dalgaboyuna sahip mevcut en iyi UDK HgCdTe dedektörlerinkiyle karşılaştırılabilir.

Ek olarak, piksel ve ODD seviyesinde cazip performansa sahip, katı kaynaklı MBE yöntemiyle büyütülmüş, geniş formatlı (640x512), uzatılmış kısa dalga boyu kızılötesi (KDK) In<sub>0.83</sub>Ga<sub>0.17</sub>As sensör üretim süreçleri geliştirilmiştir. Kompozisyonu doğrusal olarak değişen AlInAs tampon katman üzerine laboratuvarımızda büyütülen, mesa yapısında ODD pikselleri, 300 K sıcaklığında 2.65 µm kesim dalgaboyuna sahip olup, 300 K ve 200 K tepe dedektiviteleri ~2.5x10<sup>10</sup> and ~1x10<sup>12</sup> cm $\sqrt{\text{Hz}}/W$  olmakla beraber her iki değerde Johnson gürültüsü tarafından belirlenen teorik limite eşdeğerdir. Piksellerin karanlık akım analizi sonucunda karanlık akım 200 K sıcaklığa ve 3 V ters eğilme gerilimine kadar jenerasyon-rekombinasyon ve paralel kaçak akım bileşenleri tarafından belirlenmekte olup kaydadeğer bir tünelleme bileşeni görülmemiştir. Ayrıca ODD pikselleri gürültü ölçümlerinde 1/f tipi gürültü bileşeni göstermemiştir. Yüksek örgü uyumsuzluğuna rağmen ODD çok iyi tepkisellik doğrusallığı vermiş olup, etkileyici bir tepkisellik dağınıklığı (% 5.5) ve piksel çalışma oranı (% 99.8) göstermiştir ki bu değerler benzer kesim dalga boyuna sahip uzatılmış InGaAs ODD'ler için raporlanmış en iyi değerler arasındadır. Bu sonuçlar yüksek üretim maliyetli KDK HgCdTe ODD'lere karşı bir alternatif olarak 2.7 µm'ye kadar uzatılmış kesim dalgaboyuna sahip InGaAs KDK ODD teknolojisinin uygulanabilirliğini göstermektedir.

**Anahtar Kelimeler:** Kızılötesi fotodedektörler, Odak düzlem dizinleri

To Irmak and Arya, for making my life beautiful

## ACKNOWLEDGMENTS

Last one-third of my life spent in this laboratory taught me so much that everything I know about electronics and physics are just negligible when compared. These years are the best life experience to me, more than a PhD. Before and more than everyone else, I need to acknowledge the director of this story, my advisor Prof. Dr. Cengiz Beşikci. Thank you for everything without any exception. Throughout these years I received the help, guidance and the lessons that no one else could and would provide.

I would like to thank, Prof. Dr. Nevzat Gençer, Prof. Dr. Mehmet Parlak, Prof. Dr. Yüksel Ergün and Assist. Prof. Dr. Serdar Kocaman for their valuable comments and being on my thesis committee. Additionally I would like to thank Prof. Dr. Tayfun Akın for sharing his facilities with us.

According to my last count, I worked with over 40 people in this lab. It was my pleasure to work with all of you but I need to name my seniors, Ümid Tümkaya, Selçuk Özer, Gökhan Demirci, Oray Orkun Cellek, Burak Aşıcı, Süleyman Umut Eker and Melih Kaldırım. This story started with you beautiful people.

I would like to thank to Mr. Özgür Şen for his supernatural efforts to keep the laboratory working. Your friendship is invaluable and your motivation is unbelievable.

I would like to thank Dr. Tahir Çolakoğlu as well for his valuable help during detector characterization.

I gratefully acknowledge the financial support and funding from

- ASELSAN Inc.,
- Research and Development Department of the Ministry of Defense,
- Scientific and Technical Research Council of Turkey (TÜBİTAK),
- Research and Development Department of Undersecretariat for Defense Industries throughout my studies.

I would like thank my two families, Özgür and Arslan families for their understanding and never ending support throughout my hard times.

Finally, Irmak and Arya thank you for your patience and giving me strength to keep going.

## TABLE OF CONTENTS

ABSTRACT .....	v
ÖZ.....	vii
ACKNOWLEDGMENTS.....	x
TABLE OF CONTENTS .....	xii
LIST OF FIGURES.....	xv
CHAPTERS	
1. INFRARED BANDS AND DETECTORS.....	1
1.1 Infrared Basics .....	2
1.1.1 Short History of Modern Infrared Detectors .....	2
1.1.2 Blackbody Radiation and Atmospheric Considerations.....	7
1.1.3 Infrared Imaging Basics .....	11
1.2 Detector Basics .....	16
1.2.1 Detector Types .....	16
1.2.2 Figures of Merit.....	22
1.3 Quantum Well Infrared Photodetectors .....	25
1.3.1 Responsivity, Quantum Efficiency and Gain .....	27
1.3.2 Dark Current.....	29
1.3.3 Noise.....	30
1.3.4 Light Coupling .....	31
1.3.5 Material Systems .....	34

1.3.6	Special QWIP Configurations.....	37
1.4	HgCdTe Photodiodes .....	38
1.4.1	Material System Properties .....	38
1.4.2	Device Architectures and Recent Advancements .....	42
2.	InGaAs/InP QWIPS .....	49
2.1	Impact of Device Gain on FPA Performance.....	50
2.2	Feasible LWIR QWIP Material Systems .....	54
2.3	InP Based QWIPs: The Origin of Superiority.....	56
2.4	InP/InGaAs Multi Quantum Well Epilayer Design.....	61
2.5	MBE Growth of InGaAs/InP QWIPs.....	63
2.6	InP/InGaAs QWIP Fabrication.....	67
2.7	Characterization Setups .....	72
2.7.1	I-V Measurements.....	72
2.7.2	Responsivity Spectrum Measurements .....	72
2.7.3	Responsivity and Detectivity Measurements .....	73
2.7.4	NETD Measurement .....	74
2.8	Preliminary Characterization of Epilayer Structures.....	75
2.9	Detailed Characterization at Pixel and FPA Level.....	76
3.	PERFORMANCE ENHANCEMENTS IN InGaAs/InP QWIPS.....	93
3.1	Diffraction Grating .....	93
3.2	Substrate Removal and Underfill .....	96
3.3	Anti-Reflection Coatings.....	100
3.4	Electromagnetic Simulations.....	103
4.	LWIR HgCdTe FOCAL PLANE ARRAYS .....	109

4.1	MBE Growth of HgCdTe .....	109
4.1.1	Growth Dynamics.....	110
4.1.2	MBE reactor for HgCdTe growth .....	111
4.1.3	Growth Procedure.....	113
4.1.4	Doping and Dopant Activation.....	120
4.2	HgCdTe Focal Plane Array Fabrication .....	121
4.2.1	Mesa Formation.....	121
4.2.2	Passivation.....	126
4.2.3	Ohmic Contact.....	127
4.2.4	UBM, Indium Bump Formation and Hybridization .....	127
4.3	Achieved Results and Discussions .....	127
4.3.1	Epilayer Structures .....	127
4.3.2	FPA Implementation and Characterization .....	130
5.	EXTENDED WAVELENGTH InGaAs SWIR FOCAL PLANE ARRAYS .....	133
5.1	Introduction.....	133
5.2	Epilayer Structure and MBE Growth .....	139
5.3	FPA Fabrication and Detailed Characterization .....	142
5.4	Conclusion .....	156
6.	CONCLUSIONS AND FURTHER WORK.....	157
	REFERENCES .....	161
	CURRICULUM VITAE .....	181

## LIST OF FIGURES

### FIGURES

<b>Figure 1.1.</b> Blackbody spectral radiance for two different temperatures. ....	8
<b>Figure 1.2.</b> Atmospheric transmission at sea level along a horizontal path of 2 km [29]. .....	9
<b>Figure 1.3.</b> Basic building blocks of an imager [30].....	12
<b>Figure 1.4.</b> Scanning and staring techniques in image formation [30]. ....	13
<b>Figure 1.5.</b> Direct injection readout circuit [34].....	15
<b>Figure 1.6.</b> Capacitive transimpedance amplifier circuit [34].....	15
<b>Figure 1.7.</b> Illustration of photoconductor type detector operation [34].....	18
<b>Figure 1.8.</b> The operation of p-n junction as a photon detector [34].....	19
<b>Figure 1.9.</b> Illustration of optical energy transitions in intrinsic and extrinsic detector structures [26].....	20
<b>Figure 1.10.</b> Staggered bandgap alignment and artificial bandgap of InGaSb/InAs material system used in the type-II superlattice detector structure [34]. ....	21
<b>Figure 1.11.</b> Illustration of MTF .....	24
<b>Figure 1.12.</b> Intersubband transitions in quantum wells .....	26
<b>Figure 1.13.</b> Conduction band diagram of a generic QWIP under bias [30].....	27
<b>Figure 1.14.</b> Illustration of dark current components in QWIP: thermionic emission (1), thermally assisted tunneling (2) and ground state tunneling (3) [30] .....	29
<b>Figure 1.15.</b> Schematic of a diffraction grating fabricated on top of a detector [38]....	32
<b>Figure 1.16.</b> Corrugation coupled QWIP pixel structure [50].....	33

<b>Figure 1.17.</b> Description of energy band alignment parameters .....	34
<b>Figure 1.18.</b> Cut-off versus Cd mole fraction in $\text{Hg}_{1-x}\text{Cd}_x\text{Te}$ .....	39
<b>Figure 1.19.</b> Intrinsic absorption spectrum of $\text{Hg}_{1-x}\text{Cd}_x\text{Te}$ [77] .....	40
<b>Figure 1.20.</b> Indium bump and loophole interconnects [79] .....	42
<b>Figure 1.21.</b> HDVIP architecture of DRS Technology [80].....	43
<b>Figure 1.22.</b> Two-color HDVIP architecture [80].....	44
<b>Figure 1.23.</b> Outdoor scene taken with 1280x720, 5 $\mu\text{m}$ pitch $\text{HgCdTe}$ FPA [81]. ....	44
<b>Figure 1.24.</b> Mesa architecture used by RVS [82]. .....	45
<b>Figure 1.25.</b> Outdoor scenes taken in LWIR (upper) and MWIR(lower) with RVS' 1280x720 20 $\mu\text{m}$ pitch two color FPA [82]. .....	46
<b>Figure 1.26.</b> Pseudoplanar structure by DEFIR (CEA-LETI & Sofradir) [84].....	47
<b>Figure 1.27.</b> Laboratory image taken with 10 $\mu\text{m}$ pitch MWIR FPA at 120 K [85].....	47
<b>Figure 2.1.</b> Noise and photo-electrons generated by a 20x20 $\mu\text{m}^2$ FPA pixel with different gains and background temperatures (a) $f/2$ aperture, (b) $f/4$ aperture [89] .....	53
<b>Figure 2.2.</b> Gain and sensitivity of a desirable QWIP with flexible characteristics adaptable to different conditions [89]. .....	54
<b>Figure 2.3.</b> Simulated drift distance vs. the average electric field for $\text{Al}_{0.3}\text{Ga}_{0.7}\text{As}/\text{GaAs}$ QWIP (circles). Upper data points (squares) show the results obtained after artificially increasing the $\Gamma - L$ energy separation equivalent to that in InP [90]. .....	58
<b>Figure 2.4.</b> Thermal images taken with the two FPAs under different conditions. In the case of the InP/InGaAs QWIP FPA, the detector bias is adjusted to have nearly half filled ROIC capacitors while looking at 300 K background. AlGaAs/GaAs QWIP FPA in the short (0.5 ms) integration mode is operating at a bias voltage providing the optimum detectivity [89]. .....	60
<b>Figure 2.5.</b> QWIP epilayer structure and design parameters.....	61
<b>Figure 2.6.</b> Typical growth chamber cross section for a vertical MBE system [105]...64	

<b>Figure 2.7.</b> Schematic cross-sectional view of As and P valved cracker cells [106].	65
<b>Figure 2.8.</b> The rocking curve of S4 epilayer structure.	67
<b>Figure 2.9.</b> SEM image of large area test detectors	68
<b>Figure 2.10.</b> FPA fabrication steps [30]	70
<b>Figure 2.11.</b> 25 $\mu\text{m}$ pitch mesa profile obtained with HBr:Br solution	71
<b>Figure 2.12.</b> Responsivity spectrum measurement setup	73
<b>Figure 2.13.</b> Responsivity and detectivity measurement setup	74
<b>Figure 2.14.</b> Normalized spectral responsivity of the InP/InGaAs and AlGaAs/GaAs QWIP test pixels [108].	77
<b>Figure 2.15.</b> I-V characteristics of fabricated InP/InGaAs QWIP test pixels and bias dependency of activation energy (inset) [108].	79
<b>Figure 2.16.</b> Dark and photocurrents of AlGaAs/GaAs and InP/InGaAs QWIP FPA pixels at 72 K [108].	81
<b>Figure 2.17.</b> Peak responsivity of the InP/InGaAs QWIP FPA pixels versus reverse bias voltage (mesa top negative) [108].	82
<b>Figure 2.18.</b> The peak detectivity of InP/InGaAs QWIP FPA pixels with $f/2$ aperture [108].	82
<b>Figure 2.19.</b> Noise and photoconductive gains of InP/InGaAs QWIP pixels [108].	83
<b>Figure 2.20.</b> Drift distances of InP/InGaAs and AlGaAs/GaAs QWIPs extracted from measurements [108].	85
<b>Figure 2.21.</b> I-V characteristics of the pixels fabricated with improper and improved passivation techniques [108].	86
<b>Figure 2.22.</b> Normalized NETD histogram of the InP/InGaAs QWIP FPA at 68 K and $V_{\text{bias}} = \sim 2.6$ V [108].	89
<b>Figure 2.23.</b> NETD of the InP/InGaAs QWIP FPA with half-filled ROIC capacitors and 300 K background at different operation temperatures [108].	89

**Figure 2.24.** Background limited NETD performance of the InP/InGaAs QWIP at low integration times .....90

**Figure 2.25.** Thermal images recorded with the InP/InGaAs QWIP FPA (a) at ~80 K, (b) at ~ 65 K. The second thermal image is recorded with 300  $\mu$ s integration time [108]. .....91

**Figure 3.1.** Responsivity of test detectors with different grating periods .....95

**Figure 3.2.** Dependence of responsivity enhancement on grating period .....95

**Figure 3.3.** Responsivity spectra of test detectors with different grating periods .....96

**Figure 3.4.** The FPA support pixels coupled to fanout substrate before and after substrate removal.....98

**Figure 3.5.** The responsivity spectrum of S5 with and without InP substrate .....98

**Figure 3.6.** The responsivity spectrum of S2 with and without InP substrate .....99

**Figure 3.7.** The responsivity spectrum of S2 with and without underfill.....100

**Figure 3.8.** Transmission of InP substrate with single side AR coating.....101

**Figure 3.9.** Spectral responsivity of S5 FPA support pixels before (left) and after (right) AR coating.....102

**Figure 3.10.** Black body responsivity of S5 FPA support pixel after AR coating .....103

**Figure 3.11.** SEM pictures of the actual and modelled pixel geometry .....104

**Figure 3.12.** Field solutions for 1 $\mu$ m (left) and 5 $\mu$ m (right) substrate thickness .....105

**Figure 3.13.** Parametric scan of substrate thickness in 6-12  $\mu$ m region.....106

**Figure 3.14.** Volume integration of  $E_z$  for wavelengths 8.1  $\mu$ m and 9.1 $\mu$ m .....107

**Figure 4.1.** Simplified schematic of HgCdTe MBE process [116]. .....110

**Figure 4.2.** Riber C21 reactor used in HgCdTe growths .....112

**Figure 4.3.** Initial spotty RHEED pattern due to excess tellurium [118] .....115

**Figure 4.4.** RHEED pattern from CdZnTe substrate after tellurium desorption [118]116

<b>Figure 4.5.</b> Ideal RHEED pattern during growth [118].....	116
<b>Figure 4.6.</b> RHEED pattern from a twinned surface [118] .....	117
<b>Figure 4.7.</b> RHEED pattern induced by insufficient Hg [118] .....	118
<b>Figure 4.8.</b> RHEED pattern from an unrecoverable rough surface [118] .....	118
<b>Figure 4.9.</b> RHEED pattern from a polycrystalline surface [118] .....	119
<b>Figure 4.10.</b> Cross-sections of etched stripes with HBr:Br (stripe widths underneath) .....	123
<b>Figure 4.11.</b> Etching profile obtained with BCl <sub>3</sub> /N <sub>2</sub> chemistry .....	125
<b>Figure 4.12.</b> Etching profiles obtained with low energy argon sputter .....	126
<b>Figure 4.13.</b> Responsivity versus absorber layer thickness ( $\lambda c=10 \mu\text{m}$ , 77 K) [122].	128
<b>Figure 4.14.</b> LWIR HgCdTe epilayer structure.....	129
<b>Figure 4.15.</b> 300 K FTIR transmission of typical LWIR HgCdTe epilayers.....	130
<b>Figure 4.16.</b> Dark and photocurrents of $\sim 10 \mu\text{m}$ cut-off LWIR photodiode.....	131
<b>Figure 4.17.</b> 320x256 HgCdTe FPA hybridized with ROIC .....	132
<b>Figure 4.18.</b> Thermal image recorded with 320x256 FPA fabricated with LWIR HgCdTe detector epilayer structure grown on Si substrate .....	132
<b>Figure 5.1.</b> Detector epilayer structure.....	140
<b>Figure 5.2.</b> Rocking curve of detector epilayer structure .....	141
<b>Figure 5.3.</b> Surface morphology of a lattice mismatched extended InGaAs photodiode epilayer structure.....	141
<b>Figure 5.4.</b> I-V characteristics of FPA pixels in the temperature range 160-300 K (10 K steps) .....	143
<b>Figure 5.5.</b> Dark current activation energy of FPA pixels .....	144
<b>Figure 5.6.</b> Variation of the R <sub>o</sub> A product with temperature.....	145
<b>Figure 5.7.</b> Dark current components at 300 K operation temperature.....	146

**Figure 5.8.** Dark current components at 200 K operation temperature .....146

**Figure 5.9.** Variation of G-R lifetime with temperature.....148

**Figure 5.10.** Dark current components between temperatures 220-270 K.....148

**Figure 5.11.** Variation of shunt resistance with temperature.....150

**Figure 5.12.** Spectral quantum efficiency of the FPA pixels .....151

**Figure 5.13.** Spectral detectivity of the FPA pixels.....151

**Figure 5.14.** Noise current spectral density of the FPA pixels at 200 K under 30 mV reverse bias .....152

**Figure 5.15.** Responsivity histogram of the FPA pixels.....153

**Figure 5.16.** Filled ROIC capacity versus source radiance .....154

**Figure 5.17.** Snapshot images yielded by the FPA (at ~180 K) with 1 point nonuniformity correction and without bad pixel replacement .....155

## **CHAPTER 1**

### **INFRARED BANDS AND DETECTORS**

Infrared (IR) photodetector technology is an active research topic driven by many applications from various fields. Higher performance, lower production/operation costs and better reliability requirements are pushing the technology to the excellence of the existing methods by discovering new techniques and materials. Under the influence of this fact, this thesis work is focused on the improvement of three major IR photodetector technologies: Quantum Well Infrared Photodetectors (QWIPs), HgCdTe sensors and extended InGaAs photodetectors. Development/improvement of each of these technologies is an extremely challenging work due to the nature of IR sensor technology involving sensor design, semiconductor material growth, material characterization, development of microfabrication/hybridization processes, integration with the dewar and testing. Indeed, one can easily say that a large format IR sensor array (focal plane array, FPA) is probably the most difficult semiconductor device to fabricate. It is for this reason that only very few research laboratories in the world are capable of manufacturing and hybridizing infrared FPAs.

Combining efforts toward the development and improvement of three different IR sensor technologies in a Ph.D. thesis study has unavoidably made this work quite extensive and difficult. However, it has also been very fruitful in terms of the scientific results achieved

throughout it. Due the large content of this study, only the results achieved with utmost scientific and technological importance will be presented and discussed in this thesis.

The thesis starts with introducing historical and technical background on infrared radiation and infrared detector fundamentals. This introduction is followed by a review of Quantum Well Infrared Photodetectors (QWIPs) and HgCdTe photodiodes. In this section, the current status of these technologies and present bottlenecks are described. The thesis continues with the presentation of the results of the research conducted in each of the aforementioned detector technologies. In the following two chapters, the investigation of the design parameters of InP/InGaAs QWIPs, the demonstration of a high quantum efficiency InP/InGaAs QWIP focal plane array (FPA) and an investigation of the structural performance enhancement of the QWIP detectors are presented. In the fourth chapter of the thesis, MBE synthesis of the HgCdTe material and the fabrication of photodiodes are described. Last research topic included in the thesis is the investigation of extended wavelength Shortwave Infrared (Ex-SWIR) InGaAs p-i-n photodiodes. Under this research topic, lattice mismatched MBE growth of the InGaAs p-i-n photodiode structures are conducted and photodiodes are fabricated with these materials. The characterization results both at discrete detector and FPA levels are presented in this chapter as well. Lastly, the thesis is finalized with a short summary of conducted work, obtained results and potential extension of the presented research work.

## **1.1 Infrared Basics**

### **1.1.1 Short History of Modern Infrared Detectors**

The term infrared, according to its modern definition, corresponds to the portion of electromagnetic spectrum starting from the nominal edge of the visible red light (700 nm / 430 THz / 1.7 eV) and covers up to the high energy end of the microwave region (1 mm / 300 GHz / 1.24 meV). The acquaintance of mankind with this part of the spectrum is more than two centuries old. The discovery of infrared radiation dates back to the experiments of Frederick William Herschel in February 11<sup>th</sup> 1800, where he measured the temperature of each color with a thermometer after passing the sunlight through a

prism [1], [2]. Studies on `calorific rays` (as Herschel called) remained limited in the next thirty years due to lack of sensitive and accurate detectors other than an ordinary thermometer. Thomas Johann Seebeck discovered the thermoelectric effect in 1826 [3], and four years later L. Nobili made the first thermocouple improving the electrical thermometer based on thermoelectric effect. Macedonio Melloni introduced the concept of thermopiles by connecting several bismuth-copper thermocouples in series. This series connection resulted in a linearly increased, therefore, measurable output voltage yielding a sensitivity that could detect the heat from a human at a distance of 10 meters [4]. In 1880, Samuel Pierpont Langley developed his first bolometer in which two thin ribbons of platinum foil were connected so as to form the two arms of a Wheatstone bridge. The sensitivity of Langley's bolometer was much greater than contemporary thermopiles. Furthermore, he continued to develop his bolometer for next 20 years and achieved 400 times better sensitivity than his initial instrument. His latest bolometer was able to detect the heat from a cow at a distance of 400 meters [5].

At the initial stages of IR detector development, there was no distinction of *thermal detectors* and *photon detectors*. The first photon effect, the photoconductivity of selenium, was described by Willoughby Smith in 1873 while he was experimenting with selenium as an insulator for submarine cables [6]. Theodore W. Case discovered the IR photoconductivity of some sulfur containing substances in 1917 [7] and developed the first IR photoconductor (thallous sulphide,  $Tl_2S$ ). Especially during World War II, significant amount of research and development on infrared imaging and related materials (lead salts primarily) has been conducted, and many products with military use emerged. In the post war period, rapid advances in the field has been made due to appearances of new narrow bandgap material systems. Appearing in the beginning of the 1950s, InSb drew attention due to its small bandgap and the fact that it can be synthesized in single crystal form using conventionally available techniques. In the same decade, ternary material systems  $InAs_xSb_{1-x}$ ,  $Pb_{1-x}Sn_xTe$  and  $Hg_{1-x}Cd_xTe$  were introduced. In 1959, reported results of Lawson and co-workers on mixed crystals of HgTe-CdTe [8] triggered the development of the ternary alloy HgCdTe which is the most common infrared detector material preferred in modern high performance systems. Lawson and

co-workers in Royal Radar Establishment England have disclosed this material system in a patent (1957), and they are now known as the inventors of HgCdTe. Having very favorable optical and electrical properties and providing unmatched degrees of freedom to designers, HgCdTe has been challenged by several other material systems. One of these rivals was PbSnTe which was explored in parallel until late 1970s. Research on infrared detection with PbSnTe and most IV-VI chalcogenides is then discontinued due to the very high dielectric constant limiting the frequency response and very high thermal coefficients of expansion restraining the coupling reliability with silicon readout circuitries. Aside from the progress in the material science, the development of new fabrication techniques strongly influenced the evolution of the infrared detectors. After the photolithography became available in early 1960s, it was used in implementation of infrared detector arrays. PbS, PbSe and InSb are the first materials used for fabrication of linear detector arrays. The first forward looking infrared (FLIR) system with a real production program employed extrinsic Ge:Hg linear arrays and was built in 1969 for Air Force B52 Aircrafts by Hughes. This system was using a 176 element detector array and was operating at 25 K with a two stage cooler [9]. The US common module HgCdTe linear arrays with 60, 120 or 180 elements have been used in many systems worldwide. In mid 1970s, intermediary systems (line scanning with time delayed integration function) appeared while mainstream attention turned to the second generation 2D photovoltaic detector arrays.

Again in 1970, first proposals of the “superlattices” have been published by Esaki et al. [10]. This idea was the seed for quantum well infrared photodetectors (QWIPs) and infrared detection with type-II superlattices. Early proposals of IR detection using intersubband transition in quantum wells were made by Chang et al. [11], Esaki and Sakaki [12] and Coon and Karunasiri [13]. The first experimental attempt was made in 1983 by L.C. Chui et al. [14]. Later on West and Eglash [15] reported the first detailed observation of intersubband transition in quantum wells. In 1987 Levine and co-workers from Bell Labs demonstrated the first QWIP which is the ancestor of modern designs [16]. Today benefiting from mature manufacturing technologies, QWIP is one of the few field proven infrared photon detector technologies which remained in use to this day.

After the seed from Esaki et al. in 1970, Sai-Halasz et al. [17, 18] gave birth to the idea of the broken band alignment and type-II superlattices in 1977-1978. From 1979 to mid 1990s, infrared detection with type-II superlattices evolved to maturity with theoretical and experimental works. In the period of 1996-2005, high performance detectors have been shown and focal plane arrays have been demonstrated. The strongest motivation in the field is the fact that type-II superlattice is the most mature technology which theoretically has potential to outperform HgCdTe. Even though theoretical predictions have not been met yet, in the period after 2005, type-II superlattice is an increasingly active research field with the emergence of advanced heterostructure designs and progress in the focal plane array technology [19].

After 1930s, the popularity of fast and high performance photon detectors has significantly suppressed the research on thermal detectors. Even though their development never ceased, being slower and less sensitive compared to photon detectors, thermal detectors have been significantly less exploited for military and commercial applications. On the other side, the cooling requirement and the resulting high cost/low reliability of the photon detector systems have been the major driving force of the research for better uncooled thermal detectors. A pneumatic infrared detector developed by Marcel J.E. Golay [20] and thermistor bolometers originally developed by Bell Telephone Laboratories [21, 22] are notable advances in 1940s and 1950s. The first non-scanned infrared passive imagers with thermal detectors appeared in 1960s. Evaporographs [23] and absorption edge image converters [24] were the first examples of such imaging devices which had disappeared over time. Another notable thermal detector type was the pyroelectric vidicon [25] which found some usage in firefighting and emergency service organizations. The development of uncooled infrared imagers for practical military applications started to find financial support from the US government in the beginning of 1970s [9]. Initial efforts were mainly concentrated on barium strontium titanate (BST) in Texas Instruments and micromachined vanadium oxide ( $\text{VO}_x$ ) microbolometers in Honeywell. Much of the research conducted in this field by many companies remained undisclosed until 1992 due to classified military contracts in the US. In the mid-1990s, amorphous silicon technology for bolometer fabrication has

appeared. BST technology and its replacement thin-film ferroelectric (TFFE) technology were discontinued in 2009 after changing hands between Texas Instruments, Raytheon and L-3 Communications. As of today, uncooled infrared detector market is dominated by VO<sub>x</sub> microbolometers, however, a-Si technology remains as a strong competitor with increasing share in the market [26].

Today, the development of third generation thermal imagers is underway and this generation is (somewhat loosely) characterized with the following highlights:

- large format arrays with high pixel counts,
- small pixel pitch and reduced array size,
- enhanced spectral capabilities (multi-color detection with spatial/temporal coherency)
- high operating temperature and lowered cooling/power requirements,
- enhanced on-chip functions, and so on.

After its initial discovery by William Herschel in 1800, infrared detection and detectors attracted more attention each day due to increased awareness of several facts:

- The thermal radiation which is a form of electromagnetic radiation generated by the thermal motion of charged particles in matter, is emitted mostly in the infrared region by room temperature objects. This thermal radiation is the main principle for passive thermal imaging which finds usage in many fields.
- A vast number of materials have signature absorptions/emissions in the infrared region. This fact makes infrared spectroscopy a useful tool for many characterization purposes.
- Slightly more than a half of the solar energy arriving on earth's surface is known to be in the form of infrared radiation [27]. Intuitively, the interaction of the infrared radiation with terrestrial existence is a major player in ecological equilibrium.
- Observation of space in infrared unveils tremendous amount of information about universe that is otherwise unobtainable. Cold objects or objects occluded by dust clouds can be observed in infrared wavelengths. Highly redshifted radiation from fast moving celestial objects falls into the infrared region as well [28].

Many applications rising from these facts have kept the attention on infrared detection alive over centuries. Some of the related physics and metrics are reviewed in the following sections.

### 1.1.2 Blackbody Radiation and Atmospheric Considerations

Incident radiation on an arbitrary material is subject to reflection, absorption and transmission processes. Once the ratios of these components are represented by unitless coefficients of absorbance ( $\alpha$ ), reflectance ( $\rho$ ) and transmittance ( $\tau$ ), Kirchhoff Law of Thermal radiation can be formulated as,

$$\alpha + \rho + \tau = 1 . \quad (1.1)$$

The term blackbody was introduced in 1860 by Gustav Kirchhoff and defined as an idealized body which perfectly absorbs all the incident electromagnetic radiation regardless of the frequency or angle of incidence ( $\rho = 0, \tau = 0$ ). At equilibrium, absorbed energy is re-emitted by *blackbody radiation*.

All baryonic matter (i.e. regular matter composed of atoms) with a temperature above absolute zero, emits electromagnetic radiation, and this radiation represents the continuous conversion of the body's thermal energy into electromagnetic energy. From a classical physics point of view, this radiation originates from the thermal motion of the charged particles inside the matter whereas from a statistical point of view this is spontaneous process of radiative distribution of entropy. This radiation is called thermal radiation or blackbody radiation. At thermodynamic equilibrium, energy loss by this emission is balanced by absorption processes.

Correct physical description of the blackbody radiation is first proposed by Max Planck in 1900 and was named after him as Planck's Law. Derivation of the energy distribution of the blackbody radiation bases on the statistics of a quantum confined photon gas. The blackbody radiation has a continuous frequency spectrum only determined by the absolute temperature of the body. According to Planck's law, spectral radiance  $L_{e\lambda}$  ( $\text{W}\cdot\text{sr}^{-1}\cdot\text{cm}^{-2}\cdot\mu\text{m}^{-1}$ ) of a blackbody is given by,

$$L_{e\lambda}(\lambda, T) = \frac{2hc^2}{\lambda^5} \frac{1}{e^{hc/\lambda k_B T} - 1} \quad (1.2)$$

where  $T$  is the blackbody's absolute temperature, and  $\lambda$  is the wavelength. Spectral radiance for two different blackbody temperatures are shown in **Figure 1.1**.

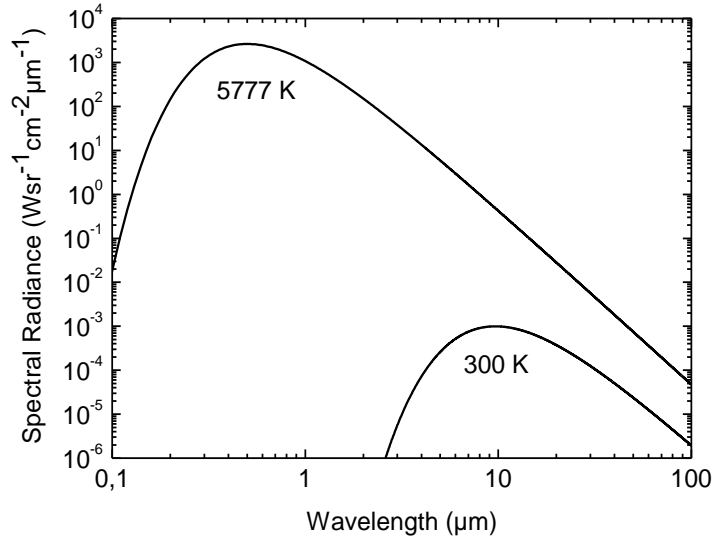


**Figure 1.1.** Blackbody spectral radiance for two different temperatures.

Radiance of the blackbody is not a function of direction. Therefore, a perfect blackbody is also a Lambertian radiator. There are several immediate consequences deduced from Planck's law. One of them is the Wien's displacement law which gives the peak emission wavelength ( $\lambda_{peak}$ ) for a given blackbody temperature  $T$ ,

$$\lambda_{peak} = \frac{2898 \mu m \cdot K}{T}. \quad (1.3)$$

Using this relation, one can easily see that near room temperature objects have peak emission around 10  $\mu m$ . Another useful relation is Stefan-Boltzman law which relates the radiant excitation  $M_e$  ( $W \cdot cm^{-2}$ ) of a blackbody to its temperature  $T$  as,

$$M_e = \sigma T^4 \quad (1.4)$$

where  $\sigma$  is a constant and has a value of  $5.67 \times 10^{-12} \text{ W} \cdot \text{cm}^{-2} \cdot \text{K}^{-4}$  for a perfect blackbody. This relation is useful to understand how strongly radiated power depends on the blackbody's temperature.

In practice, ordinary objects do not obey perfect blackbody definition and exhibit partially reflective and transparent properties. This deviation from perfect blackbody condition is characterized by the *emissivity* ( $\epsilon$ ) property of the object. The emissivity value ranges between 0 and 1 and signifies how much the object's radiative behavior resembles to a perfect blackbody. Emissivity is a strong function of object's thickness, surface conditions and observation wavelength.

In most of the cases, propagation medium for the blackbody radiation is air. While propagating through atmospheric contents, emitted radiation is subject to absorption and scattering processes. Atmospheric transmission depends on many parameters including weather conditions, altitude, humidity and air constituents. An example transmission curve along a 1600 m horizontal path at sea level is given in **Figure 1.2**.

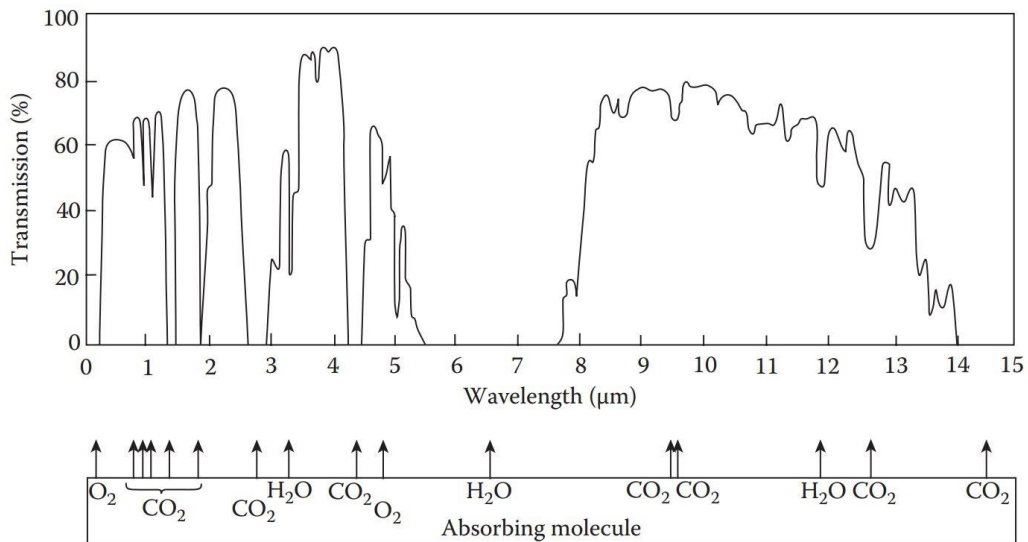


**Figure 1.2.** Atmospheric transmission at sea level along a horizontal path of 2 km [29].

Absorption by gaseous molecules (dominantly H<sub>2</sub>O and CO<sub>2</sub>) determines mostly the shape of the atmospheric transmission windows. These transmission windows also lead to subdivisions within the infrared region. The commonly used scheme is as follows:

- 0.7 – 1.4 μm, Near-infrared (NIR): Extends from the end of the visible portion of the spectrum to the water absorption band at around 1.38 μm. Fiber optic telecommunication and image intensifiers are important applications in this band.
- 1.4 – 3.0 μm, Short-wavelength infrared (SWIR): Water and ice have effective absorptions in this band. 1.55 μm wavelength is significant for long range telecommunication applications. Night glow, which is a natural ambient illumination available at nights, has considerable power in this band.
- 3 – 8 μm (or commonly 3 – 5 μm), Mid-wavelength infrared (MWIR): Significant radiation is emitted from hot objects (engines) and exhaust plumes at these wavelengths. This band is useful for heat seeking guidance and passive thermal imaging with sensitive detectors. Signature emissions from combustions and CO<sub>2</sub> permits special applications. Due to the nature of the thermal emission curves (see **Figure 1.1**) detection in MWIR band is expected to provide higher contrast than LWIR band.
- 8 – 12 μm, Long-wavelength infrared (LWIR): This region is known for its use in thermal imaging. Completely passive, long range thermal imaging is possible in this band through relatively large thermal radiation from near room temperature objects.
- 12 – 20 μm, Very long-wavelength infrared (VLWIR): VLWIR band is an extension of the LWIR band and provides certain advantages while imaging scenes colder than room temperature with reduced incoming photon flux. This band also finds astronomical applications.
- 20 – 1000 μm, Far-infrared, (FIR): This lowest energy subdivision of the infrared region is used in scientific (Terahertz lasers), astronomical (imaging of very cold heavenly bodies) and some medical applications (Far Infrared Sauna), but not limited to.

The atmospheric transmission in the LWIR band is dominated by molecular absorptions, and under most circumstances, LWIR window provides better transmission for short ranges (less than 10 km). Under high humidity and visual clarity (no scatterers) conditions, MWIR may provide better transmission particularly for ranges exceeding 10 km. Not being a thermal imaging window, SWIR may provide better transmission than the visible region especially under hazy and foggy weather conditions.

### **1.1.3 Infrared Imaging Basics**

Compared to visible imaging, infrared imaging may reveal more precious information on a scene and it may even enable scene inspection in cases where visible imaging is not possible.

Imaging in the visible region (400 – 700 nm) is basically the intensity mapping of the light reflected from the surfaces in the scene. Therefore, existence of an external illumination and its reflection are essential for imaging in visible wavelengths. The same concept applies for infrared wavelengths up to  $\sim 3 \mu\text{m}$  except for the cases where the scene consists of very hot objects. Starting from the MWIR region, practically every object with a temperature near/above room temperature behaves as a source by itself, and an external illumination is no longer necessary. In this case, imaging becomes completely passive and is called *thermal imaging*.

Imagers, by definition, converts the electromagnetic radiation mapping of a scene into geometrically corresponding electrical representation. Basic identifiable blocks of modern imagers are illustrated in **Figure 1.3**.

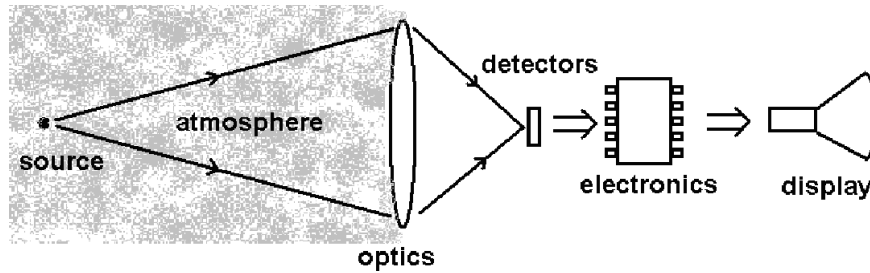


**Figure 1.3.** Basic building blocks of an imager [30]

After the incoming radiation is collected by the optics, a real image is formed on the image plane. The detector array, which is placed on the image plane, performs the electro-optic conversion, and the resulting electrical signal is read by the readout integrated circuit (ROIC). ROIC sends out the electrical signal to proximity electronics preserving the temporal and spatial correspondence of the signal. Final signal processing (pixel registration, image formation, non-uniformity and bad pixel corrections, etc.) is performed by the electronics, and the image is displayed to the user.

Infrared optics has the same fundamentals with visible optics, but materials and tolerances are different. Depending on the wavelength and application, Ge, ZnS, ZnSe, CaF<sub>2</sub>, Sapphire, Quartz and some special plastics are among the suitable materials for optics manufacturing in the infrared region. The main task for the optics is to collect the radiation through an aperture and form the image on the detector. In the first generation imagers where detectors were only single elements or were consisting of a linear array of elements, optics were also responsible for *scanning* the scene over the detector (in one or two dimension) in order to form the image. Starting from the second generation imagers, detectors consisted of 2D *staring* arrays as well, and optics were only responsible of the formation of a steady image. In some cases, the *microscanning* technique is used with 2D arrays to increase the spatial resolution of the image by shifting the image over the detector by fractions of the pixel pitch in a single frame time. The image forming techniques are illustrated in **Figure 1.4**.

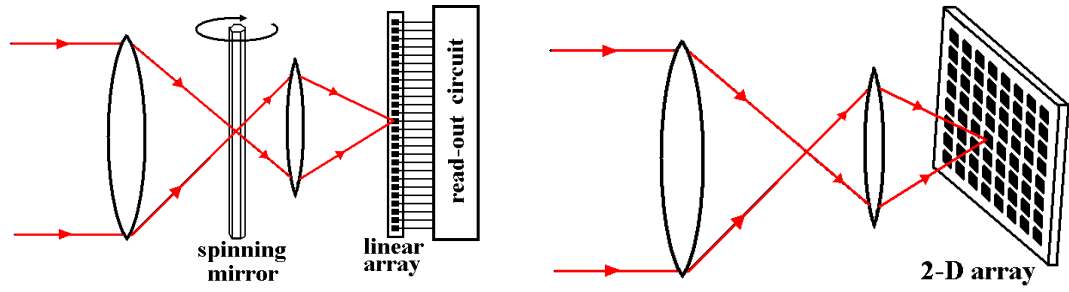


**Figure 1.4.** Scanning and staring techniques in image formation [30].

For an optic system, the f-number (denoted as  $f/\#$ ) is defined as the ratio of the lens's focal length to the diameter of the image of the physical aperture stop in the object space (entrance pupil). The f-number is the main parameter determining the amount of flux transferred to the detector. The radiant exitance  $M_e$  on the object plane is transferred to the irradiance on the image plane  $E_e$  by the ideal optics with the relation,

$$E_e = \frac{M_e}{4(f/\#)^2 + 1}. \quad (1.5)$$

The f-number also determines the minimum spot size achievable on the image plane according to the following relation,

$$R_{Airy} = 1.22 \cdot \lambda \cdot (f/\#) \quad (1.6)$$

where  $R_{Airy}$  is the radius of the Airy disk, and  $\lambda$  is the operating wavelength. *The Rayleigh criterion* suggests that two spots on the image must be separated by at least the radius of the Airy disk in order to be considered as resolved. Another approach to determine the impact of the f-number on the imaging resolution is to match the spatial cutoff frequency of the optics to the Nyquist frequency of the FPA [31]. For an ideal pixel this will occur at

$$\frac{(f/\#) \cdot \lambda}{d} = 2 \quad (1.7)$$

where  $d$  is the pixel pitch on the FPA. In any case, the diffraction sets a fundamental resolution limit, and diffraction limited performance is the ideal case. On the other hand,

another resolution limiting factor, *aberrations*, are the imperfections related to design, material and practical issues. The effects of aberrations worsen as f-number decreases, so a minimum f-number and a maximum field-of-view (FOV) is dictated by aberrations. Thus there is a fundamental trade-off between flux transfer and image quality. Optical designers play around these limitations by considering the application requirements and engineering practices in order to reach the diffraction limited performance.

Electro-optic conversion of the radiation passing through the optics is performed by the detector. The first generation of imagers were scanning systems using 1D detector arrays. In the scanning systems, signal extraction from the detector is synchronized with sliding of the scene, and only a slice of a frame is recorded at a shot (line time). The same detector elements are used to detect multiple positions in a frame, and, as a result, temporal coherency of the image is disturbed. In the second generation imagers 2D detectors arrays were employed. Thus, there is one-to-one spatial correspondence between detector elements and image elements, and the temporal coherency within the frame is preserved. Each detector element generates its own individual signal depending on the falling illumination.

The signal generated by the detector is conveyed as an electrical current, and this current is collected by the ROIC for each image element individually. ROIC may utilize different input architectures usually required by the detector configuration and application. One of the most commonly used input circuit scheme is the Direct Injection (DI). In the DI architecture, detector current is injected into an integration capacitor via the source of an input transistor. The injected detector current is integrated in the integration capacitor during the frame time. At the end of the frame time, the capacitor voltage is read and reset. This simple architecture enables the use of a large integration capacitance and the adjustment of the gain by changing the capacitance. Also the power consumption is lower compared to more complex circuits. However, under low illumination conditions performance of DI input circuit degrades due to decreased injection efficiency ( $\eta_{inj}$ ) which is approximated by [32, 33]

$$\eta_{inj} = \frac{IR_d}{IR_d + (nkT/q)}, \quad (1.1.8)$$

where  $R_d$  is the dynamic impedance of the detector,  $I$  is the total injected detector current, and  $n$  is the input transistor ideality factor (usually in the range 1-2 ).

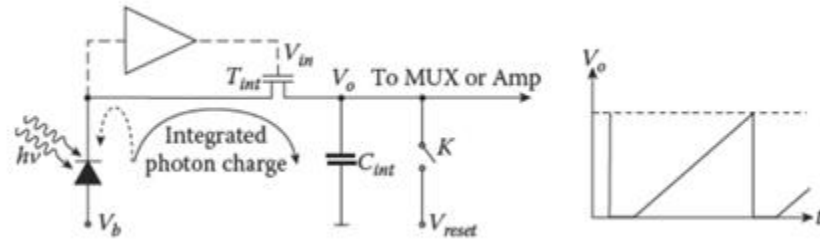


**Figure 1.5.** Direct injection readout circuit [34]

The capacitive transimpedance amplifier (CTIA) is another commonly used readout input circuit which is suitable especially for applications with low background flux or high linearity requirement. In the CTIA circuit (**Figure 1.6**), detector current is integrated onto the feedback capacitor of the inverting amplifier during the frame time. The detector current is efficiently integrated for a wide range of detector dynamic resistance or current level due to the very high input resistance of the amplifier. CTIA circuit have the disadvantage of complexity and higher power consumption when compared to other input circuits.

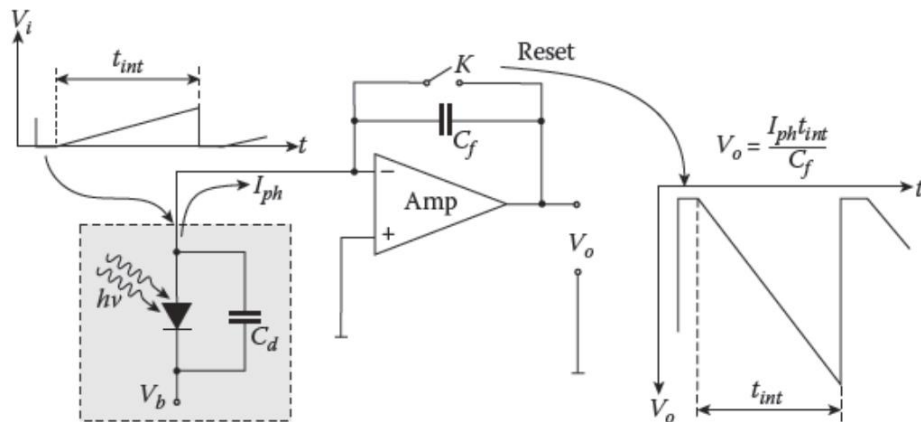


**Figure 1.6.** Capacitive transimpedance amplifier circuit [34]

The detector signal is transferred to the camera electronics after it has been captured by the ROIC. The main tasks performed by the electronics before the image is presented to the user (or transferred to the next stage of an electro-optical system) can be listed as follows,

- generation of the necessary driving signals for ROIC,
- digitization of detector output,
- formation and post processing of the image,
  - color mapping and gain control,
  - bad pixel replacements and non-uniformity correction,
- user-defined functions on the image.

The imaging is completed at this stage, and the scene information is ready to be presented to the user or to further processing by the next stages of the system. The detector, which has the very important electro-optic conversion role in this imaging chain, will be explained in detail in the next section.

## **1.2 Detector Basics**

### **1.2.1 Detector Types**

Theoretically all physical phenomena involving an energy exchange in the range of 0.1 – 1 eV can be suggested for infrared detection [35]. However the number of detector technologies that has found use is quite limited considering all possible detection mechanism. As a result of the historical trends and advances in the material technology, the infrared detection mechanisms, which are being actively pursued, can be studied under two main classes, *thermal detectors* and *photon detectors*.

#### **Thermal Detectors:**

In the thermal detectors, incoming radiation is absorbed to raise the temperature of the detector's active material. The change in the active material's highly temperature dependent property (conductivity, dimension, polarization, transmission, etc.) is used to generate the signal. The generation of the signal is an indirect effect of the incoming

radiation and is independent of the photonic nature of the light. They provide modest sensitivity and give slow response due to the nature of the heating/cooling process. Thermal detectors are usually operated at/near room temperature. The production cost for thermal detectors is relatively low primarily due to absence of the cooling equipment. Thermal detectors find widespread use in low cost and low profile applications. Common thermal detector types and their detection mechanism are given in **Table 1.1**. The advances in microbolometer technology are especially noteworthy with the demonstrated noise equivalent differences below 50mK at TV frame rates.

**Table 1.1.** Infrared Thermal Detectors [32]

<b>Detector</b>	<b>Method of Operation</b>
Bolometer	Change in the electrical conductivity
Metal	
Semiconductor	
Superconductor	
Ferroelectric	
Hot electron	
Thermocouple/thermopile	Voltage generation, caused by change in temperature of the junction of the dissimilar materials
Pyroelectric	Changes in spontaneous electrical polarization
Golay cell/gas microphone	Thermal expansion of a gas
Absorption edge	Optical transmission of a semiconductor
Pyromagnetic	Changes in magnetic properties
Liquid crystal	Changes of optical properties

**Photon Detectors:**

In this class of infrared detectors, incoming radiation is absorbed by the electrons residing in appropriate energy states of the detector’s active material. Resulting change in the electronic state distribution of the material generates the signal. Absorption of the incoming radiation has strong wavelength (photon energy) dependence, since the

excitation of the electrons occurs between certain energy states. In photon detectors, the signal is almost instantaneously generated due to the nature of the excitation mechanism. Therefore, the detector response is very fast. Photon detectors, particularly those working at low energies ( $\lambda > \sim 2 \mu\text{m}$ ), require cooling in order to suppress the thermal excitation of electrons. Photon detectors can be designed to operate under different modes which is related to the creation of the electric field and extraction of the signal. The most commonly used modes are photoconductive and photovoltaic modes. In the photoconductive mode of operation, incident radiation contributes to the conductance of the detector by creating free carriers. These photo-generated carriers are collected by an *externally applied* bias voltage and the photocurrent is created (**Figure 1.7**). The generated photocurrent ( $I_{photo}$ ) by a photoconductor of length  $l$ , width  $w$  and thickness  $t$  due to an entirely absorbed incident photon flux density  $\phi_s$  is given as

$$I_{photo} = q\eta w l \phi_s g_{photo} , \quad (1.9)$$

where  $g_{photo}$  (or  $g_p$ ) is the *photoconductive gain* which is determined by the properties of the detector.

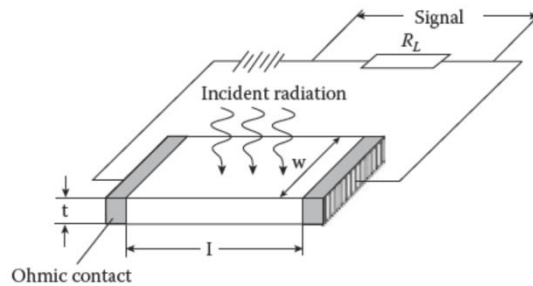


**Figure 1.7.** Illustration of photoconductor type detector operation [34].

The photoconductive gain describes the ratio of the carriers collected by external circuit to the photo-generated carriers inside the detector. If  $g_{photo}$  is larger than unity, it means that each photo-generated carrier results in the injection of more than one carrier through the contacts before this excess charge is annihilated by a recombination process. The other case where  $g_{photo}$  is smaller than unity represents the situation in which some

portion of the photo-generated carriers are recombined before they contribute to the current. If the current is mainly comprised of single type of carriers  $g_{photo}$  can be estimated as follows,

$$g_{photo} = \frac{\tau}{\tau_t} \quad (1.10)$$

where  $\tau$  is the carrier lifetime, and  $\tau_t$  is the transit time of the carriers through the device.

The other mode of the operation for a photon detector is the photovoltaic mode where the generated carriers are collected by an *internal electric field* in the device. The best example for this kind of detector is the *p-n junction*. In a standard p-n junction device, minority carriers generated in the depletion region and within the diffusion length proximity of the depletion region are swept to the other side of the junction by the built-in electric field and diffusion. The photo-generated carriers collected with this mechanism contribute to the reverse leakage current of the junction compromising the signal of the detector (**Figure 1.8**). The photocurrent of a p-n junction is given as

$$I_{photo} = q\eta A\phi_s \quad (1.11)$$

where  $\eta$  is the quantum efficiency of the device, and  $\phi_s$  is the incident photon flux. In properly designed photovoltaic devices, all the photo-generated carriers are collected by the built-in electric field and gain of the device is equal to unity.

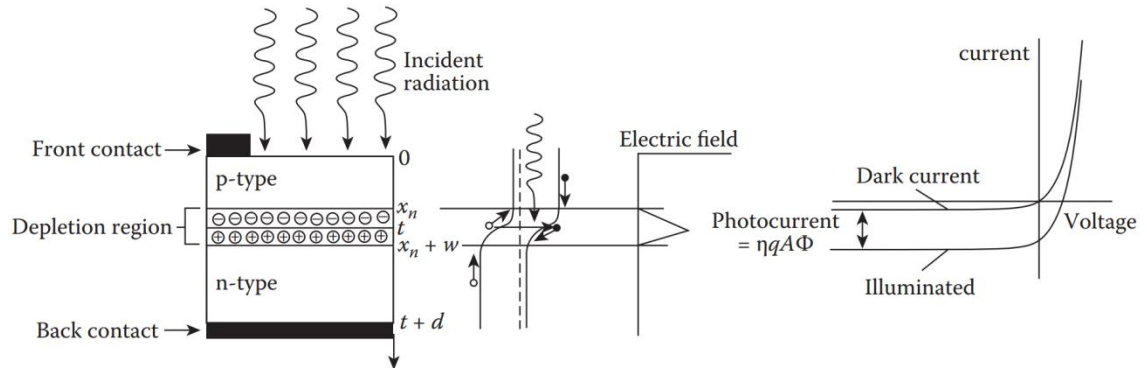


**Figure 1.8.** The operation of p-n junction as a photon detector [34].

There are also several other operating modes including photoemissive and photoelectromagnetics which will not be described in this context.

Photon detectors can be further classified under different divisions depending on the nature of the energy transitions. The most important divisions are intrinsic detectors, extrinsic detectors and bandgap engineered detectors. Intrinsic detectors are minority carrier devices which employ energy transitions across the bandgap of direct bandgap semiconductor materials as the absorption mechanism (**Figure 1.9**). Binary materials with suitable bandgap energy (InSb, InAs etc.) and ternary/quaternary materials with a bandgap adjustable in the interested energy range (HgCdTe, InGaAs etc.) are commonly used in these devices. The intrinsic detectors are characterized with high absorptions rates.

In the extrinsic detector structure, energy transitions from impurity states to conduction band are employed for the absorption of incoming photons (**Figure 1.9**). Silicon and Germanium doped with III-A and V-A materials are commonly used for the fabrication of the extrinsic detectors. They are characterized with very low operating temperature requirement and good performance under extremely low background flux conditions. Consequently, they are mostly used in astronomical applications involving very low energy radiation detection.

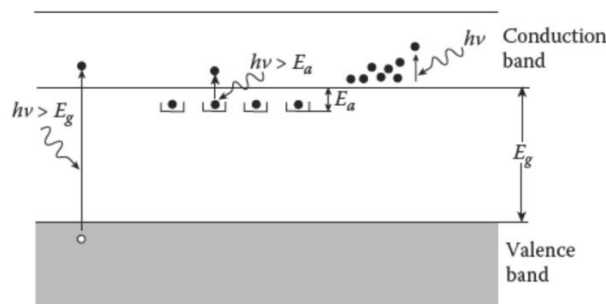


**Figure 1.9.** Illustration of optical energy transitions in intrinsic and extrinsic detector structures [26].

The bandgap engineered detectors utilize transitions through artificial energy states for photon absorption. Quantum well infrared photodetectors (QWIP) and type-II

superlattices are the most successful members of this class. In type-II superlattice structures, an artificial bandgap is formed by consecutive multilayer deposition of two materials which are chosen to have staggered bandgap alignment as shown in **Figure 1.10**. Incoming radiation is absorbed through the excitation of electrons across this artificial bandgap.

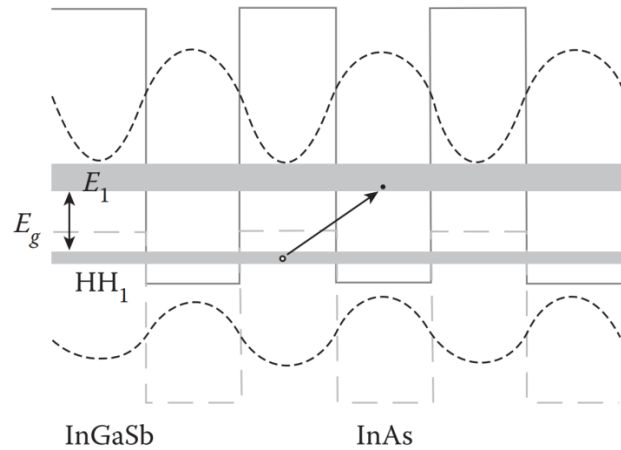


**Figure 1.10.** Staggered bandgap alignment and artificial bandgap of InGaSb/InAs material system used in the type-II superlattice detector structure [34].

In QWIP structures, confined energy states are formed in the conduction band by consecutive (multilayer) deposition of two materials which have conduction band discontinuity. Incoming radiation is absorbed by intersubband transitions of electrons trapped in these quantum wells. The operation of the QWIP structures will be explained in details in the following sections. The reported performance values for bandgap engineered detector structures improve rapidly with new design ideas and overcome of the technologic challenges. Especially QWIP is a field proven infrared detector technology with serial production level maturity.

In the next section, figures of merit of infrared detectors are explained in order to establish the necessary background for the discussion of different detector technologies throughout the thesis.

### 1.2.2 Figures of Merit

There exist several definitions in order to determine the performance characteristic of infrared detectors. Some of these definitions solely use experimental outputs, whereas some others include normalization to experimental variables in order to provide ease of comparison between different detectors.

#### **Responsivity:**

The responsivity of an infrared detector is the ratio of the output signal of the detector to the input radiation power. Symbolically, the responsivity is represented as

$$R = \frac{I_{signal}}{\Phi_{input}} \quad (1.12)$$

where  $I_{signal}$  represents the output signal of the detector. The electrical output signal can be in terms of either volts or amperes, and incident power can be specified as Watts or photons per second. The commonly used unit of responsivity for infrared photon detectors is Amperes per watt ( $A/W$ ). The response of a detector will inherently depend on the spectral content of the incoming radiation, at least at the extreme ends of the operation range. In some cases, it is convenient to specify the spectral distribution of the responsivity (*spectral responsivity*) for the detector. The spectral responsivity is characterized with a spectrum and a *peak responsivity* value. In other cases, responsivity is specified for a blackbody spectral radiant exitance under the assumption that all the incident radiation is absorbed by the detector. The resulting figure of merit is called *blackbody responsivity*. The blackbody responsivity value of a detector must be accompanied with the blackbody temperature.

#### **Noise Equivalent Power (NEP):**

The NEP is defined as the incident power required to generate unity signal-to-noise ratio at the output of the detector. Using the responsivity, NEP is given as

$$NEP = \frac{I_{noise}}{R} \quad (1.13)$$

where  $I_{noise}$  is the noise signal at the output of the detector. The unit of NEP is Watts.

**Detectivity (D) and Specific Detectivity (D\*):**

The detectivity is defined as the reciprocal of the NEP. However, the presence of the noise signal in the definition of detectivity (also NEP) makes it sensitive to other characterization parameters like detector size, measurement bandwidth and illumination level. The normalization of detectivity to detector area and measurement bandwidth is suggested by R.C. Jones [36, 37] after pointing out that noise signal increases with the square root of detector area and the measurement bandwidth under normal conditions. The normalized detectivity, specific detectivity ( $D^*$ ), is therefore defined as

$$D^* = D(A_d \Delta f)^{1/2} = (A_d \Delta f)^{1/2} \frac{R}{I_{noise}} \quad (1.14)$$

with the unit  $cm\sqrt{Hz}/W$ , which is also called (after its inventor's name) *Jones*. The usage of the specific detectivity is questionable under abnormal conditions where noise signal does not follow the square root relation with the detector area (e.g. dominant peripheral noise) or noise signal has a strongly non-uniform power spectral density (e.g. strong 1/f noise). If noise signal has external dependencies on any characterization parameter, it must be specified. The most common situation is the photon shot noise limited case of operation. In this case, noise signal, therefore the specific detectivity, will depend on the amount incident illumination during measurement. Under such a situation, the amount of incident illumination on the detector should accompany the reported specific detectivity value by some means (e.g. exitance, numerical aperture together with radiance or equivalent blackbody temperature).

**Noise Equivalent Temperature Difference (NETD):**

Although it is readily derivable from detectivity and spectral responsivity, NETD has practical importance due to its intuitive meaning and ease of practical use. NETD has the unit of temperature, and it represents the change in the temperature of the target which causes a change in the signal equal to the rms noise of the detector. The definition of the NETD applies to both discrete detectors and detector arrays, but, in most cases, NETDs used in characterizing detector arrays and population statistics of individual detectors

elements are of interest. NETD is a system scale performance parameter where contributions from all the system components must be taken into account while evaluating the results.

**Modulation Transfer Function (MTF):**

Modulation transfer function is the spatial frequency response of an imaging system as illustrated in **Figure 1.11**. If the imager can translate the contrasts at a certain spatial frequency on the scene to the image, then the imager is said to resolve that frequency. The higher the maximum resolvable spatial frequency, the sharper the image is. MTF is a system level parameter with significant contributions from many components of the imager (e.g. optics and electronics) beside the detector.

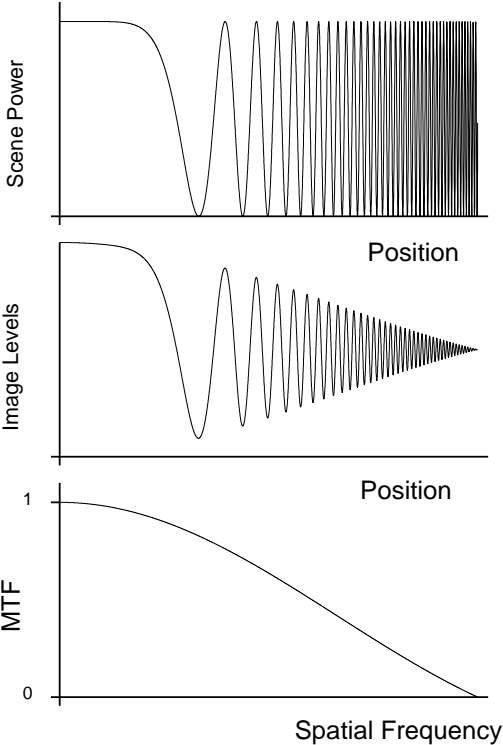


**Figure 1.11.** Illustration of MTF

### **Minimum Resolvable Temperature Difference (MRTD):**

MRTD is system level performance parameter through which both thermal and spatial resolving capabilities of an imaging system are measured. The measurement of MRTD involves visual inspection of the image of standard test patterns over a background. The observer is asked for the visibility of the test patterns while temperature difference with background is gradually changed at the lower visibility limits. Since it relies on observations of individuals, MRTD measurements for a system are subjective. Therefore averaging of the results over a group of observers is preferred.

In the next sections, several photon detector technologies are reviewed in detail in order to provide the necessary background before presenting and discussing the results of this thesis study.

### **1.3 Quantum Well Infrared Photodetectors**

As mentioned before, quantum well infrared photodetectors rely on intersubband transitions in large bandgap semiconductors. These transitions occur in the quantum wells formed by consecutive deposition of two different materials with a band discontinuity (barrier and well materials) as shown in **Figure 1.12**. Electrons residing in the ground state get excited by the photons to the second state which is located near the tip of the barrier. The excited electrons move into continuum and create the photoconduction.

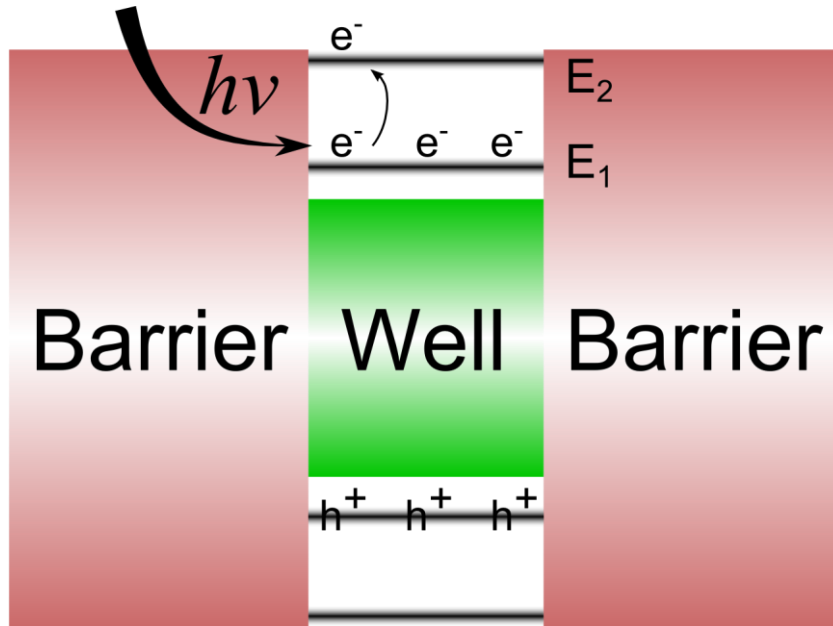


**Figure 1.12.** Intersubband transitions in quantum wells

The position of the second state relative to the tip of the barrier affects the escape of the excited electron to the continuum. If the second state is below the tip of the barrier, a strong electric field (external bias) is required to force the electron to tunnel through the tip of the barrier and move to the continuum. This configuration is called bound-to-bound operation. In this case, the second energy state is well confined and oscillator strength is high. This results in a narrow absorption spectrum with relatively high peak quantum efficiency. However, the responsivity is decreased via photoconductive gain due to lowered escape probability of the excited electrons. The reverse case is where the second state is above the tip of the barrier and electrons are directly excited to the continuum. This configuration is called bound-to-continuum operation, and, in this case, all the previously mentioned properties of bound-to-bound operation are reversed. The desired situation is the mid-point of these two extreme cases where the second energy state is leveled with the tip of the barrier (bound-to-quasibound operation).

Actual QWIP structures consist of multiple quantum wells connected in series. The well stack is finished with conductive contact layers at both sides. The conduction band diagram and the physical structure of a generic QWIP is shown in **Figure 1.13**.

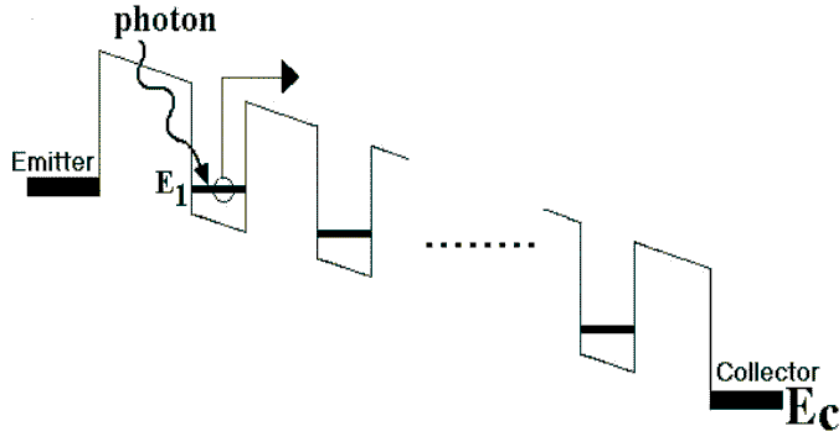


**Figure 1.13.** Conduction band diagram of a generic QWIP under bias [30].

### 1.3.1 Responsivity, Quantum Efficiency and Gain

The absorption probability of a photon in a single quantum well can be derived (under certain assumptions) using Fermi's Golden Rule as [38]

$$\eta_a = \frac{q^2 h}{4\epsilon_0 n_r m^* c} \frac{\sin^2 \theta}{\cos \theta} n_{2D} f \delta(E_2 - E_1 - h\nu) \quad (1.15)$$

where

- $f$  : oscillator strength,
- $m^*$  : effective mass of electrons in the quantum well,
- $\theta$  : incidence angle w.r.t. growth axis,
- $n_{2D}$  : 2D quantum well carrier density,
- $n_r$  : refractive index of the quantum well material,
- $h$  : Planck's constant,
- $\nu$  : photon frequency.

This equation provides the most basic insight about the absorption behavior of the QWIP. It can easily be seen that the absorption probability for the normally incident radiation ( $\theta = 0$ ) is theoretically zero due to the  $\sin^2 \theta$  term arising from the polarization selection rule. Calculations on a standard QWIP structure for oblique incidence ( $\theta = 45^\circ$ ) will

lead to absorption coefficients ( $\sim 1500 \text{ cm}^{-1}$  [38]) lower but comparable to that of intrinsic detectors ( $\sim 3000\text{-}6000 \text{ cm}^{-1}$  for HgCdTe). However, oblique incidence is not a practically realizable condition for focal plane arrays. This struggle necessitates the addition of a new engineering parameter in the design, *optical coupling*, which will be discussed later. The horizontal incidence condition ( $\theta = 90^\circ$ ) gives an infinite absorption probability, since it corresponds to infinitely long absorption path. In this case absorption coefficient can be extracted by normalizing the absorption probability with the absorption path as  $L_w/\cos\theta$ .

The event of collection of an electron in response to an incoming photon in the QWIP structure comprises the following steps:

- transition of an electron to the excited state with a probability of  $\eta_a$ ,
- escape of the excited electron to continuum with a probability of  $p_e$ ,
- collection of the generated electron by the contacts depending on  $g_{photo}$ .

Putting all these steps together, the collected charge per incoming photon energy or the responsivity of the QWIP can be given as [39]

$$R = q \frac{\lambda}{hc} \eta_a p_e g_{photo} = q \frac{\lambda}{hc} \eta g_{photo} . \quad (1.16)$$

In this relation,  $\eta_a$  is called absorption quantum efficiency, and  $p_e$  is called escape probability. The product of these two parameters is the incoming photon's probability of creating a free electron, which is defined as the internal quantum efficiency. Similarly the product  $\eta g_{photo}$  is called conversion efficiency (or external quantum efficiency). The gain,  $g_{photo}$ , has the same meaning in QWIP as in other photoconductive detectors. However, free electrons travelling through a QWIP structure are subject to additional capture and scattering mechanisms which are not present in other photoconductive detectors. In idealized calculations of SNR based performance parameters ( $D^*$  and NETD), gain does not seem to have any influence. The important role of the gain is understood when conditions due to practical limitations (e.g. limited integration time and low background) are imposed. The effects of gain are discussed extensively in another chapter.

### 1.3.2 Dark Current

Even in the absence of illumination, the dark current flows through the structures under applied bias due to generation of free carriers by other means. Three main mechanisms generating the dark current in QWIPs are illustrated in **Figure 1.14**.

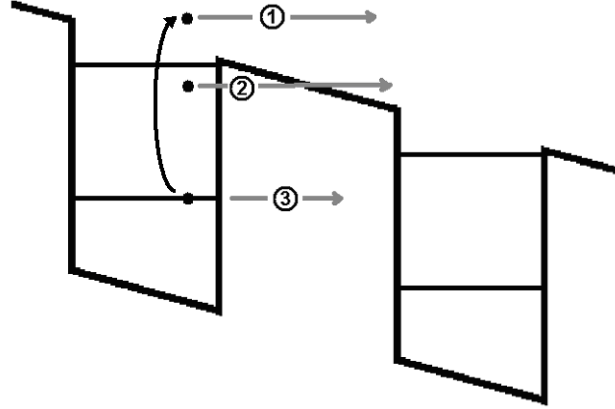


**Figure 1.14.** Illustration of dark current components in QWIP: thermionic emission (1), thermally assisted tunneling (2) and ground state tunneling (3) [30]

Sequential ground state tunneling (3) is usually important only at very low temperatures and can be decreased to negligible levels at operating temperature by adjusting the barrier thickness. Thermionic emission (1) and thermally assisted tunneling (2) normally govern the dark current around the operating temperature. Thermal excitation of electrons in the quantum well is unavoidable and can only be suppressed by cooling. The operating temperature of the QWIP is set by this cooling requirement to cryogenic temperatures where the dark current does not limit the performance. The thermally generated carrier density can be approximated under abrupt tunneling probability and low bias assumptions as [39]

$$n_{thermal} = \left( \frac{m^* kT}{\pi \hbar^2 L_p} \right) e^{-(E_b - E_1 - E_f)/kT} . \quad (1.17)$$

where  $L_p$  is the quantum well period, and  $E_b$  is the energy barrier height. If we define the dark current activation energy as  $E_a = E_b - E_1 - E_f$  and recall the dependency of dark current density to thermally generated carrier density as

$$J_{dark} = q \times n_{thermal} \times v_{drift} , \quad (1.18)$$

the temperature and energy dependence of dark current density can be formulated as

$$\frac{J_{dark}}{T} \propto e^{-(E_a)/kT} . \quad (1.19)$$

Several precautions must be taken during the design in order to obtain a reasonable operating temperature. If the position of the second energy state is set further above the tip of the barrier (bound-to-continuum operation), this will promote the thermal generation of the carriers by decreasing the activation energy. However, no corresponding improvement will occur in optical excitation and responsivity. In addition to the exponential temperature dependence of the thermally generated dark current, doping density of the well ( $N_D$ ) affects the dark current through  $E_f$  as they are related with [38]

$$n_{3D} = N_D = \frac{m^*kT}{\pi\hbar^2L_w} \ln(1 + e^{E_f/kT}) . \quad (1.20)$$

The doping density must be chosen properly to keep the dark current and operating temperature at reasonable levels while preserving adequate quantum efficiency.

### 1.3.3 Noise

The dominant noise mechanism under normal operating condition in QWIPs is the Generation-Recombination (G-R) noise. The G-R noise originates from small fluctuations in the number of occurrences of carrier generation and recombination events in a given time interval. These two events have a known average rate and occur independent of the time since last event such that they follow a Poisson distribution. The total device current is linked to the fluctuations in the generation and recombination with the factor called noise gain ( $g_{noise}$  or  $g_n$ ). After summing the contributions of both

events and linking to the device current, the G-R noise expression in dark current dominated regime is given by Poisson statistics as [38]

$$i_{n,dark} = \sqrt{4qg_{noise}I_{dark}\Delta f}. \quad (1.21)$$

Under illumination, the generation of the photocurrent is directly coupled to the arrival of the photons which also follows a Poisson distribution. The photo-generated carriers are subject to same recombination mechanisms. Therefore, the photocurrent appears in the noise expression in the same way as the dark current. The ultimate (desirable) noise floor in QWIPs is reached when the condition  $I_{photo} \gg I_{dark}$  is established by sufficient cooling. In this case, the noise expression reads,

$$i_n \approx \sqrt{4qg_{noise}I_{photo}\Delta f}. \quad (1.22)$$

Under this condition, G-R noise is called *Photon noise* and it is unavoidable. The operating temperature of the QWIP structure is set by the cooling requirement to meet  $I_{photo} \gg I_{dark}$  condition (Background Limited Performance, BLIP). The noise gain ( $g_{noise} = 1/(Np_c)$ ,  $p_c$ : *capture probability*) is very closely related to the photoconductive gain ( $g_{photo} = p_e/Np_c$ ) in QWIPs, and they are observed to be practically equal in situations where escape probability approaches to unity [38].

The Johnson (Thermal) noise which is inherent to all resistive devices, is not a significant noise contributor in QWIPs under usual operating conditions [40]. Similarly, another common detector noise mechanism,  $1/f$  noise, is not observed in QWIPs [41], and this is attributed to the large band gap of the involved materials and maturity of the production processes.

### 1.3.4 Light Coupling

The light coupling in (n-type) QWIPs is a complex research and engineering topic due to insensitivity of intersubband transitions to normal incident radiation. Although there is considerable detector response to normal incidence as partly explained by some secondary effects (near-field coupling [42], doping effects [43], spatial variation of

effective mass and coupling to valence band [44]), many attempts and designs have been demonstrated to improve the QWIPs responsivity significantly. The main aim, common to all designs, is to create an electric field component normal to the quantum well plane by either reflecting, refracting, diffracting or resonating the incident radiation. Apart from scientific concerns, practically designed light coupling schemes are desired to be compatible with 2D FPA processing while keeping the detector uniformity, process complexity, yield and crosstalk at reasonable levels. The most basic light coupling approach is the illumination through a 45° facet. This method is preferred in testing of discrete detectors. However, it cannot be adapted to 2D array technology where the most commonly used method is the diffraction grating coupling. In this method, incident radiation is diffracted by the elements fabricated on top of the detector (**Figure 1.15**). The diffractive elements are in the form of etched pits or trenches leaving unetched bumps, all coated with gold for near lossless reflection. The diffractive elements are in the form of etched pits or trenches leaving unetched bumps, all coated with gold for near lossless reflection.

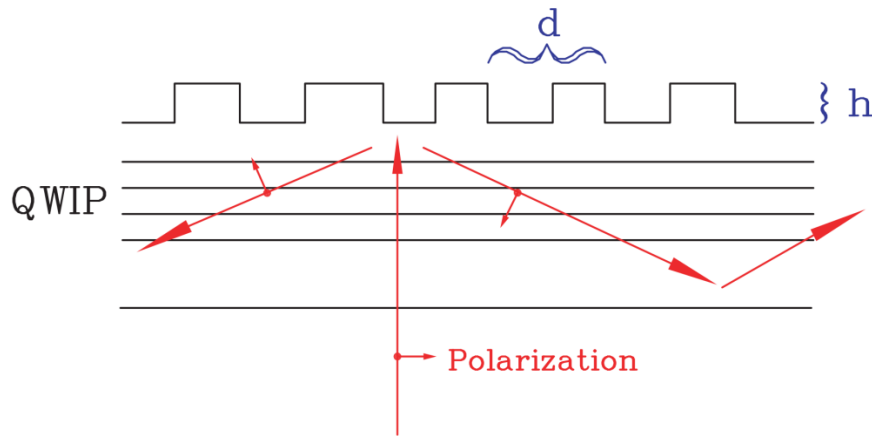


**Figure 1.15.** Schematic of a diffraction grating fabricated on top of a detector [38].

The grating may consist of linear (lamellar), two dimensional, biperiodic or random shaped/sized diffractive elements designed according to the application’s spectral requirements. In the basic two dimensional etched cross grating design (**Figure 1.15**), the grating period,  $d$ , should be approximately equal to  $\lambda_c/n_r$ , where  $n_r$  is the refractive index of the material ( $\sim 3.3$  for InGaAs and GaAs), and  $\lambda_c$  is the absorption cutoff wavelength in the material. The etch depth,  $h$ , should be equal to  $\lambda_c/4n_r$ , and the ratio

of etched to unetched areas should be unity in order to eliminate direct reflection (0<sup>th</sup> order diffraction). The design of the gratings can be customized for wider or dual band responses [45]. There are also special applications like polarization sensitive imaging which is enabled with customized use of diffraction gratings [46]. The accurate grating design is a complex optics problem involving contributions from many effects such as free carrier absorption, realistic modeling of actual geometries, finite mesa sizes, imperfect reflections from metals and so on. The efficiency of diffraction gratings is shown to be decreasing as the mesa size is reduced [47, 48]. However, with the currently used pixel pitches, the diffraction grating is still a preferred light coupling choice of QWIP manufacturers.

Corrugations are other light coupling structures that have been extensively studied. In this method, detector mesas are in the form of trapezoids, and light coupling is achieved by reflections at the corrugated sidewalls [49]. Typical pixel structure is illustrated in **Figure 1.16**. The required sidewall inclination can be achieved by selective chemical etching of crystallographic planes or special dry etching methods.

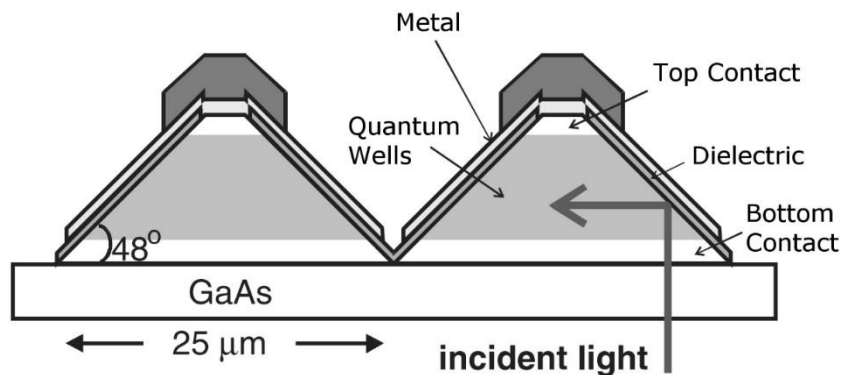


**Figure 1.16.** Corrugation coupled QWIP pixel structure [50].

The fabrication process for corrugated QWIPs (c-QWIPs) is compatible with large array production, and good performance values on megapixel size arrays have already been demonstrated [51]. Light coupling with corrugation is also demonstrated on dual-color and broad band QWIPs [50]. The coupling efficiency for c-QWIPs does not suffer from

reduced pixel size as diffraction grating do, but, a relatively larger bias is required to extract a reasonable conversion efficiency out of a thick quantum well stack needed for pixel geometry. In cases where such large bias is not applicable, achievable conversion efficiency will be limited compared to the standard designs [52].

There exist demonstrations of several other coupling schemes in the literature including microstrip antenna coupling [53], surface plasmon resonances [54, 55], photonic crystals [56] and microlenses. More recently, the resonator-QWIP (r-QWIPs) concept, in which the whole pixel volume is optimized to resonate with the help of diffractive elements, has been introduced [51]. The first experimental results of r-QWIPs were demonstrated to exhibit quantum efficiencies up to 70% in 40x40 groups of 25  $\mu\text{m}$  pitch,  $\sim 20$  well AlGaAs/GaAs QWIP pixels [57, 58].

### 1.3.5 Material Systems

The quantum well in which the electrons are confined can be realized using the band discontinuities of different barrier/well material couples. The energy band alignment parameters relevant for quantum well formation are illustrated in **Figure 1.17**. In theory, every material combination with a suitable conduction band discontinuity is usable for QWIP fabrication, and there are numerous experimental results with almost all possible combinations. Most remarkable and promising material systems are shortly reviewed below.

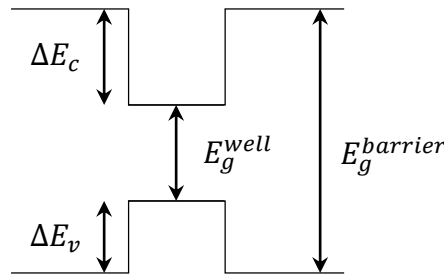


**Figure 1.17.** Description of energy band alignment parameters

### **AlGaAs/GaAs**

AlGaAs/GaAs is the most commonly used material system, since it is widely studied for many other purposes. This material system has the flexibility of bandgap adjustment without disturbing the lattice matching by changing the aluminum concentration ( $\Delta E_c/\Delta E_g = \%65$ ). This possibility enables the continuous adjustment of spectral response of the QWIPs from LWIR to lower energies (6-20  $\mu\text{m}$  [39]). For larger band discontinuities (larger aluminum concentrations  $x > \sim 0.3$ ), bandgap of AlGaAs changes to indirect, and transport properties deteriorate resulting in decreased responsivity. AlGaAs/GaAs QWIPs and related heterojunction properties are extensively studied in the literature.

### **InGaAs/InP**

The InGaAs/InP material system is used extensively in optical communication devices and has well-developed growth and processing technology. First investigation of this material system for QWIP fabrication is by Gunapala et al. [59].  $\text{In}_{0.53}\text{Ga}_{0.47}\text{As}$  ( $E_g^{well} = 0.75 \text{ eV}$ ) is lattice matched to InP ( $E_g^{barrier} = 1.35 \text{ eV}$ ) with a conduction band discontinuity of  $\Delta E_c = 0.25 \text{ eV}$  which permits LWIR operation around 8.0-8.5  $\mu\text{m}$  wavelengths. However it is shown that with slight introduction of strain to the InGaAs, more desirable spectral properties are achievable [60]. Properties and advantages of this material system are extensively discussed in the following chapters of the thesis.

### **InGaAs/InAlAs/InP**

With the use of  $\text{In}_{0.48}\text{Al}_{0.52}\text{As}$  as barrier material ( $E_g^{barrier} = 1.45 \text{ eV}$ ), the  $\text{In}_{0.48}\text{Al}_{0.52}\text{As}/\text{In}_{0.53}\text{Ga}_{0.47}\text{As}$  lattice-matched heterostructure reaches a conduction band discontinuity of  $\Delta E_c = 0.5 \text{ eV}$  which is suitable for MWIR QWIP operation with direct bandgap. First investigation of this material system for this purpose is done by Levine et al. [61] in 1988 where they reported a peak responsivity at 4.4  $\mu\text{m}$ . The demonstration of large format FPAs with this material system is also available in the literature [62].

## **InGaAsP/InP**

In order to extend the responsivity of the InGaAs/InP material to longer wavelengths, the band gap of the well can be increased by switching to the quaternary InGaAsP material without sacrificing the lattice matching. This capability of the lattice matched InGaAsP/InP system is first demonstrated by Gunapala et al. [63], [64]. They reported cutoff wavelengths reaching up to 13.2  $\mu\text{m}$  in InGaAsP(1.3  $\mu\text{m}$ )/InP structures. The FPA level performance assessment of this material system is done by Ozer et al. [65].

## **(Al<sub>x</sub>Ga<sub>1-x</sub>)<sub>0.5</sub>In<sub>0.5</sub>P /GaAs**

At  $x = 0$ , The Ga<sub>0.5</sub>In<sub>0.5</sub>P/GaAs heterostructure has a conduction band discontinuity of  $\Delta E_C = 0.22 \text{ eV}$  [39] which permits LWIR QWIP operation. The detector performances ranging from  $\sim 8 \mu\text{m}$  to  $\sim 13 \mu\text{m}$  are available in the literature [66], [67]. This material system is reported to exhibit lower dark currents than equivalent AlGaAs/GaAs counterparts [66]. (Al<sub>x</sub>Ga<sub>1-x</sub>)<sub>0.5</sub>In<sub>0.5</sub>P system has an indirect  $X$  – valley bandgap in the range  $0.7 < x < 1$ . At the  $x = 1$  limit, the  $\Gamma$  – valley conduction band discontinuity is around  $\Delta E_C \sim 0.5 \text{ eV}$  which is useful for down to  $\sim 3 \mu\text{m}$  operation on GaAs substrate [39].

## **InGaAs/GaAs**

In order to take the advantage of the desirable transport properties of binary GaAs, the strained In<sub>x</sub>Ga<sub>1-x</sub>As/GaAs system, in which GaAs constitutes the barriers, is investigated. This system has 55% conduction band offset ( $\Delta E_C / \Delta E_g$ ) and, for compositions with  $x < 0.2$ , material quality is conserved despite the strain introduced. VLWIR responses  $> \sim 12 \mu\text{m}$  are achievable with high photoconductive gain and low capture probability [68].

## **AlGaAs/InGaAs/GaAs**

The replacement of GaAs with InGaAs in the standard AlGaAs/GaAs system enables MWIR operation due to increased bandgap discontinuity. Performance remains unaltered despite the introduced strain and large format dual-color FPA demonstrations are already available [69].

### **1.3.6 Special QWIP Configurations**

Apart from standard QWIP structure in which electrons are confined in symmetrical conduction band wells, there are many variations to this configuration. Even though most of them remained as experimental research work, most significant designs are briefly explained below.

#### **p-type QWIPs**

In the p-type QWIPs, valence band quantum wells are employed for confining the hole type carriers. The main advantage of the p-type QWIPs is that they are sensitive to s-polarized (normally incident) light even more than p-polarized light, which is forbidden in n-type QWIPs [70]. Various p-type QWIPs have been demonstrated with AlGaAs/GaAs and InGaAs/InP material systems by Gunapala et al. and Levine et al. [70], [71]. Even though reported quantum efficiencies are significant ( $\eta = 28\%$ ), achieved responsivities (30-50 mA/W) are quite limited due to poor transport properties of the holes (mean free paths  $\sim 30$ -50 nm).

#### **Photovoltaic QWIPs**

Most of QWIP designs are built around a photoconductive detection mechanism where photo-generated carriers are collected by an externally applied electric field. There are also studies on a different class of QWIP structures where built-in inversion asymmetry acts as an internal electric field and collects photo-generated carriers. The designs offer usually similar detectivities at reduced or zero biases at the expense of reduction in device gain [38].

#### **Dual band QWIPs**

Detection in multiple spectral regions for a detector is a highly desirable property especially with the requirements targeted by the third generation thermal imagers. The QWIPs provide important advantages for multi-band detector designs including highly adjustable narrow band spectral response and unmatched uniformity. The spatially separated, multi-contact per pixel or bias selected multi-band operation are possible via

various QWIP structures. Many QWIP FPAs operating as MWIR/LWIR ( [72], [73], [74] ), MWIR/MWIR ( [69] ) and in other spectral regions are reported in the literature.

## **1.4 HgCdTe Photodiodes**

More than 50 years old HgCdTe is the major IR detector technology addressing the high performance requirements of modern cutting edge systems. It is a very well known material system (with all advantages and disadvantages) after more than half century of heavy research and development. HgCdTe has very favorable intrinsic properties enabling the development of IR detectors for a wide range of applications.

Bulk growth methods (Gradient Freeze, Solid State Recrystallization and Zone Melting) are used in the synthesis of HgCdTe during initial stages of the technology. Later on liquid phase (LPE) and vapor phase epitaxy (MOCVD and MBE) technologies took over as the preferred crystal growth methods. The MBE growth of HgCdTe offering greater flexibilities than all other options is the most promising method with increasing interest.

In the early stages of development, HgCdTe detectors were photoconductive devices since the technology was not mature yet to implement photovoltaic structures. Many photoconductive devices were fabricated, and they found use in the field. As the technology improved, HgCdTe photodiodes appeared with junctions formed first with ion implantation. Junctions with in situ doping (both  $n^+$ -p and  $p^+$ -n ), heterojunctions, multiple junctions (back-to-back diodes) and avalanche diodes are the key developments in the evolution of HgCdTe IR detector until present.

In the next section, fundamental material properties, which make the HgCdTe a favorable IR detector material, are presented.

### **1.4.1 Material System Properties**

$Hg_{1-x}Cd_xTe$  is a ternary compound which is a proportional mix of metallic HgTe and a large bandgap semiconductor CdTe. As expected, HgCdTe has a variable and direct

bandgap starting from -0.261 eV (semimetal) to 1.609 eV (at 77 K). The bandgap increases with increasing Cd mole fraction  $x$ , and it shows strong temperature dependence. Although there are several expressions to describe the bandgap versus  $x$  relation, the following expression by Hansen et al. [75] is commonly referenced,

$$E_g = -0.302 + 1.93x - 0.81x^2 + 0.832x^3 + (5.35(1 - 2x)10^{-4} T). \quad (1.23)$$

The cut-off wavelength,  $\lambda_c$ , associated with an energy bandgap  $E_g$  can be estimated using the relation,

$$\lambda_c = \frac{hc}{E_g} = \frac{1.24 \mu m.eV}{E_g}. \quad (1.24)$$

The corresponding cut-off wavelength versus  $x$  relation is visualized in **Figure 1.18**. The immediate observation is that the entire infrared band can be covered using the same material system by varying the alloy composition. This unique property is one of the major advantages of the HgCdTe.

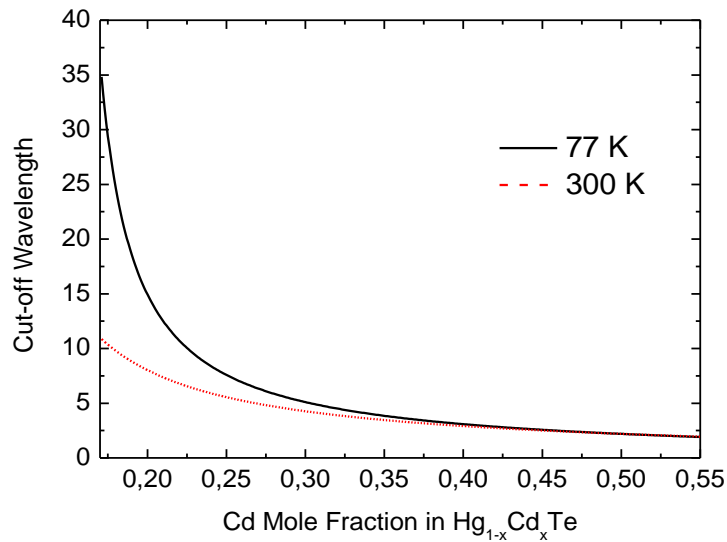


**Figure 1.18.** Cut-off versus Cd mole fraction in  $Hg_{1-x}Cd_xTe$

HgCdTe has zinc blend crystal structure like its constituents CdTe and HgTe, and retains this structure over the entire composition range. The lattice constant of the ternary crystal

changes very little with the alloy composition, and its dependency can be expressed using the relation given by Higgins et al. [76] as,

$$a = 6.4614 + 0.0084x + 0.01168x^2 - 0.0057x^3. \quad 1.25$$

The lattice constant changes only 0.22% over the entire range. This property of the HgCdTe permits all the compositions to be grown on the same substrate without significant degradation due to lattice mismatch. This freedom facilitates the implementation of structures like double/triple layer heterojunctions and HgTe/CdTe superlattices.

HgCdTe has strong and sharp optical absorption as shown in **Figure 1.19**. High absorption coefficient provides high quantum efficiency with thinner absorption layer thickness (~10 μm in the LWIR band). Additionally rapid increase of absorption coefficient with energy decreases spectral crosstalk in multi-spectral detector structures.

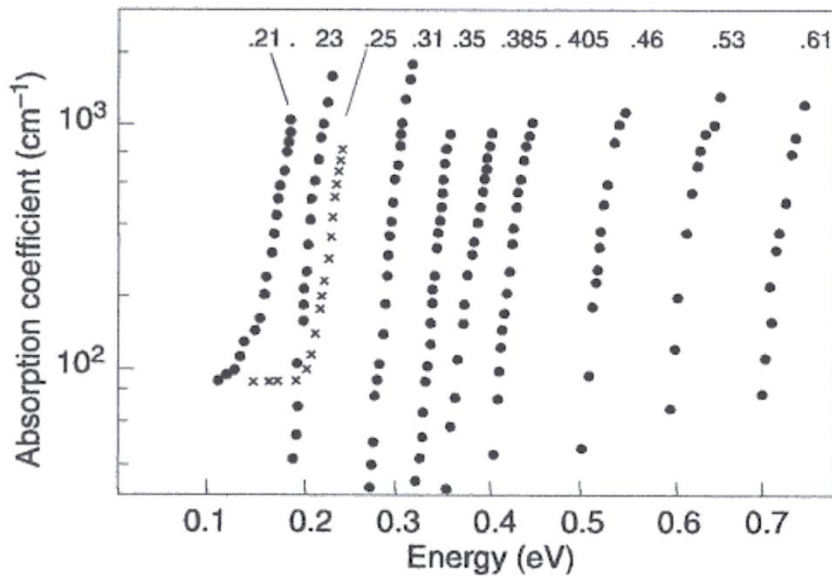


**Figure 1.19.** Intrinsic absorption spectrum of Hg<sub>1-x</sub>Cd<sub>x</sub>Te [77]

HgCdTe has favorably long minority carrier life which is required for low dark current photodiodes. Minority carrier lifetime under low carrier density (< ~10<sup>15</sup> cm<sup>-3</sup>) is limited

by the Shockley-Read-Hall (SRH) type generation- recombination processes. Since the SRH processes occur via levels in the forbidden gap, impurities and defects causing states in the bandgap are more effective in the device performance at low carrier concentrations. At higher carrier concentrations ( $> \sim 10^{15} \text{ cm}^{-3}$ ), Auger 1 process is the limiting factor of minority carrier lifetime in high quality materials (n-type), except under highly non-equilibrium circumstances [78].

Due to small effective mass ( $\sim 0.01m_0$ ), electron mobility is very high ( $10^4$ - $10^5 \text{ cm}^2\text{V}^{-1}\text{s}^{-1}$ ), and it is determined by several mechanisms including mostly optical phonon scattering and alloy scattering. The hole transport is governed by the hole effective mass ( $\sim 0.55m_0$ ), and the hole mobility is approximately two orders smaller than electron mobility. It should be noted that all the transport properties of the material have very strong dependence on alloy composition.

The weak Hg-Te bonds in the crystal is the leading reason for the instability of the material. The addition of Cd atoms to the lattice structure further destabilizes bond strengths. This instability emerges as structural inhomogeneity and defect formation tendency during material growth. The high partial pressure of the Hg in the substance significantly reduces the temperature tolerance of the material. Above temperatures  $\sim 80$  °C, Hg desorption from the lattice causes material degradation, and device processing temperature is therefore limited to unusually low temperatures.

1/f noise is a known contributor in HgCdTe based devices. Although it is not well understood, there are several models trying to explain the nature of the underlying mechanism. It is believed that 1/f noise in HgCdTe is surface originated, since thermal transition rates are too fast to support the spectral distribution of time constants required to explain spectral noise densities observed [78]. 1/f noise can therefore be associated with the surface stability issues of the material.

### 1.4.2 Device Architectures and Recent Advancements

The IR detectors -specifically FPAs- fabricated with HgCdTe material systems employ many different processing schemes, and most of the time the production details are proprietary information of manufacturers. In an FPA fabrication, basically a 2-D array of isolated p-n junctions is formed. Keeping one nodes common, the other nodes of the junctions are connected to the silicon multiplexer (readout circuit) using metallic interconnections. The indium bump and loophole interconnect methods are illustrated in **Figure 1.20**.

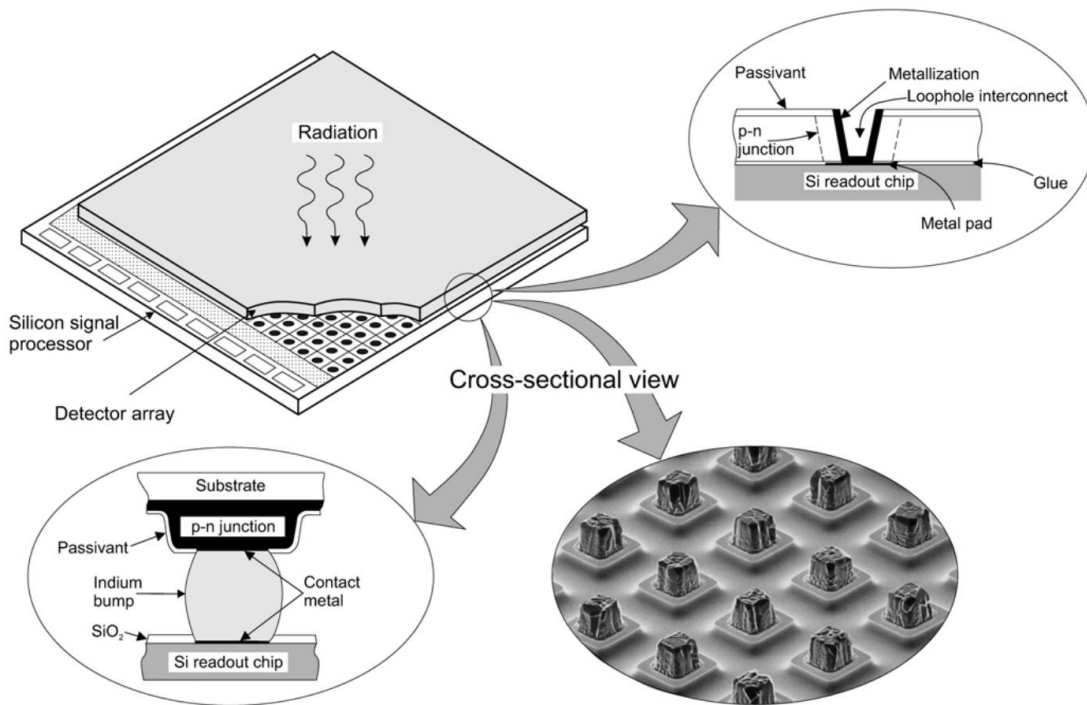


**Figure 1.20.** Indium bump and loophole interconnects [79]

The junction formation and delineation are performed with in-situ/ex-situ doping and etching steps. The exposed surfaces with electrical activity are coated with passivation materials. The current motivation of the manufacturers is toward smaller pixel pitch,

higher operation temperature and lower cost. The detector architectures used by several manufactures will be reviewed below together with their latest achievements.

High-density vertically integrated photodiode (HDVIP<sup>®</sup>) architecture is a proprietary of DRS Technology. The layout of this structure is shown in **Figure 1.21**.

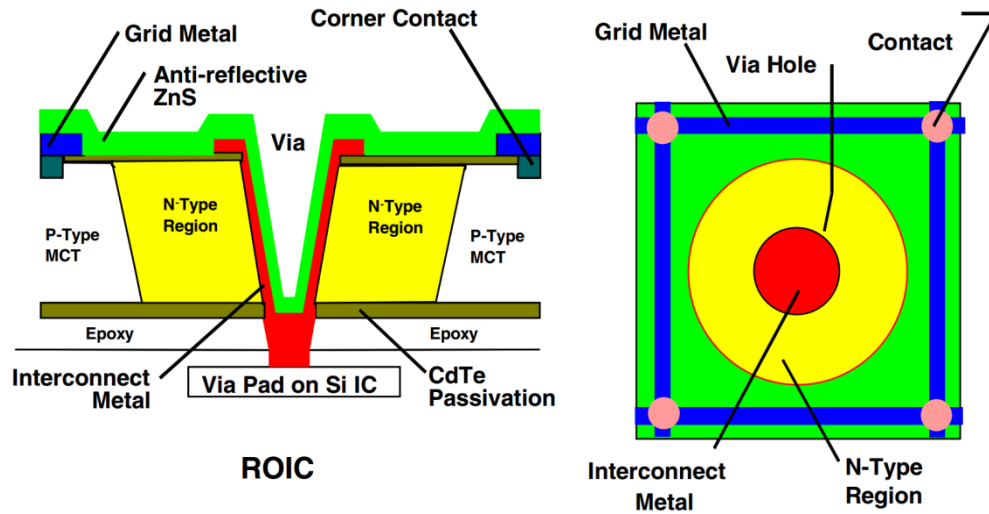


**Figure 1.21.** HDVIP architecture of DRS Technology [80].

In this architecture, a single p-type layer of HgCdTe is grown by LPE or MBE on a CdZnTe substrate. Both surfaces of the HgCdTe layer are passivated with thermal CdTe depositon after substrate transfers and removals, and then it is glued to silicon a ROIC. The n-type region and the junction are formed during via etching and ion implantation. This architecture is also applicable to two-color detector structure as illustrated in **Figure 1.22**.

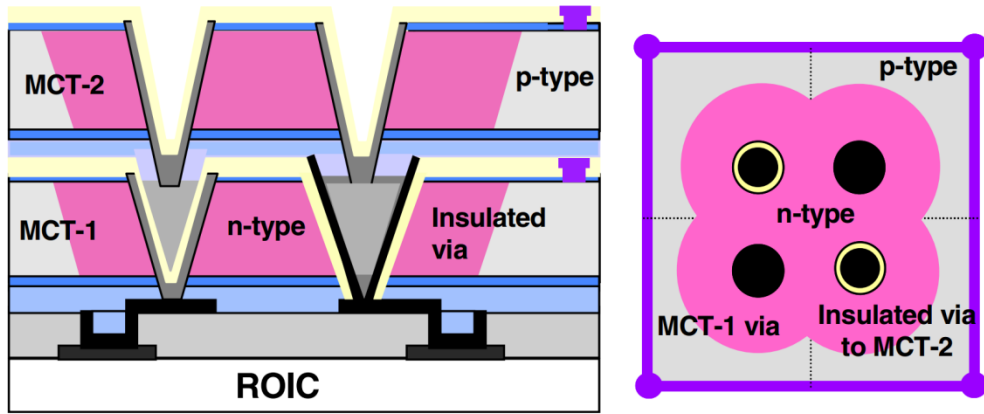


**Figure 1.22.** Two-color HDVIP architecture [80].

The first ever  $5\mu\text{m}$  pitch  $1280 \times 720$  format FPAs were reported by DRS with HDVIP architecture. The reported FPAs have operabilities  $>99.6\%$  and  $>99.95\%$ , and collection efficiencies of 45-55% and 80% in the LWIR and MWIR bands, respectively [81].



**Figure 1.23.** Outdoor scene taken with  $1280 \times 720$ ,  $5\mu\text{m}$  pitch HgCdTe FPA [81].

Raytheon Vision Systems uses the mesa architecture shown in **Figure 1.24** in the fabrication of single and two color HgCdTe FPAs. In this architecture, p-n junction is formed during the growth by incorporating indium (n-type) or arsenic (p-type) dopant

atoms to the lattice. The junctions are delineated by etching, and isolated individual detectors are formed. The mesa sidewalls are passivated with CdTe, and indium bumps are deposited on top of the pixels for ROIC hybridizations.

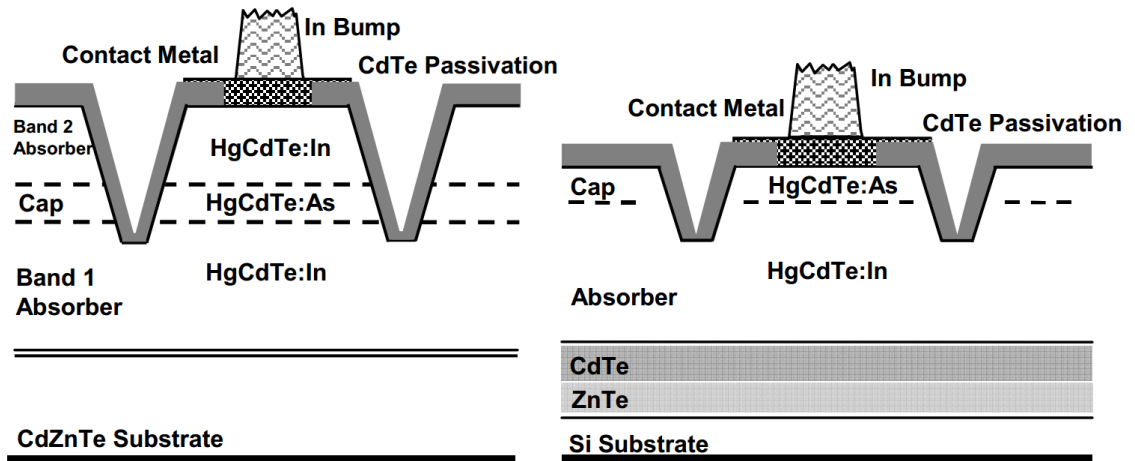


**Figure 1.24.** Mesa architecture used by RVS [82].

This architecture is also suitable for the realization of two color detection using back-to-back connected diodes. In the two color operation, detector bias polarity is sequentially switched to reverse bias only one diode at a time. The two color megapixel (1280x720) arrays with 20  $\mu\text{m}$  pitch have been demonstrated with operabilities greater than 99% in both LWIR and MWIR bands [82]. The outdoor scenes taken with RVS' two color 1280x720 FPA in LWIR and MWIR bands are shown in **Figure 1.25**.



**Figure 1.25.** Outdoor scenes taken in LWIR (upper) and MWIR(lower) with RVS' 1280x720 20  $\mu\text{m}$  pitch two color FPA [82].

Using the mesa architecture, RVS also demonstrated two color HgCdTe FPAs grown on silicon substrates. Currently, demonstrated FPAs exhibit pixel operabilities up to 99.98% in MWIR and 98.8% in the LWIR band at 81 K and  $f/3$  background [83]. As they already note in their reports, the HgCdTe on silicon substrates are not ready for strategic applications in the LWIR band due to low operability.

The planar architecture consists of an epitaxially grown (LPE, MOCVD or MBE) single absorber layer, and junctions are locally implemented by ion implantation in this

absorber layer. The planar detector structure is completed after passivation coating, contact deposition and indium bump formation. This architecture can also be manipulated to accommodate two color detection scheme as shown in **Figure 1.26**, and it is preferred by French manufactures/developers CEA-LETI and Sofradir.

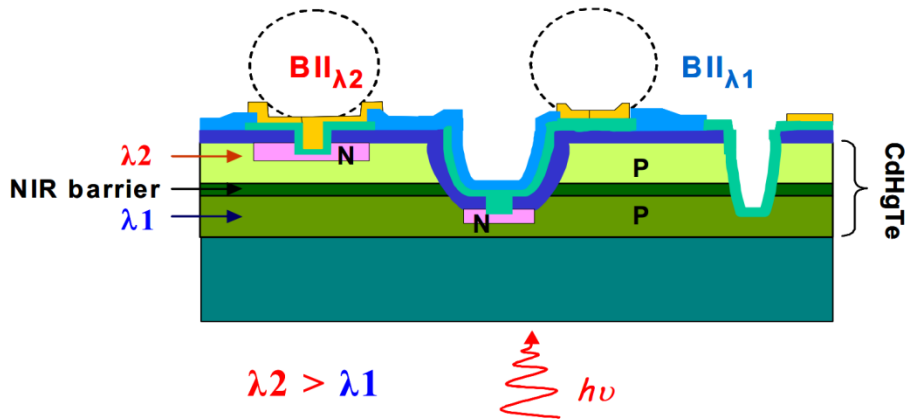


**Figure 1.26.** Pseudoplanar structure by DEFIR (CEA-LETI & Sofradir) [84].

Using planar technology and indium bump bonding, Sofradir demonstrated megapixel MWIR focal plane arrays with 10  $\mu\text{m}$  pitch maintaining an operability value above 99.5% up to 130 K [85]. An indoor screenshot taken with such FPA is shown in **Figure 1.27**



**Figure 1.27.** Laboratory image taken with 10  $\mu\text{m}$  pitch MWIR FPA at 120 K [85].

AIM Infrarot-Module reported their results on megapixel (1280x1024, 15  $\mu\text{m}$  pitch) LWIR and MWIR FPAs fabricated with HgCdTe on GaAs substrate with MBE grown planar technology. In the MWIR band, the FPA operabilities are reported to be above 99.5% for the operation temperature of 100K where as in the LWIR band, operability achieved is 99.25% at 76 K operation temperature [86].

## CHAPTER 2

### InGaAs/InP QWIPS

The standard QWIP cannot compete with the low bandgap semiconductor (inter-band transition) photodetectors at discrete sensor (single pixel) level due to considerably lower quantum efficiency and sensitivity. QWIP, in spite of this deficiency, has been able to compete with the other technologies at the FPA level by providing a lower but sufficiently high detectivity such that the FPA sensitivity is mostly governed by the uniformity. Even at the FPA level, the low quantum and conversion efficiencies of the QWIP remain as a problem since low quantum efficiency decreases the FPA operation temperature to achieve the background limited performance (BLIP) condition, and low conversion efficiency inhibits the operation with short integration times/high frame rates and/or low background radiation levels. Larger conversion efficiency (quantum efficiency-gain product) can be achieved by increasing the photoconductive gain of the device.

This chapter is dedicated to the presentation of this thesis work on the development of the InP/InGaAs QWIP FPA technology as an alternative to the standard AlGaAs/GaAs QWIPs which suffer from low quantum and conversion efficiencies being the main barrier against wider adoption of this FPA technology offering excellent uniformity, high yield and low production cost at the same time. We have achieved nearly an order of magnitude higher quantum and conversion efficiencies by utilizing the InP/InGaAs

material system to construct a properly designed multi quantum well structure providing both larger quantum efficiency and photoconductive gain. The experimental procedures conducted throughout this development work include the establishment of the entire production cycle involving the molecular beam epitaxy growth of the detector epilayer structures, FPA microfabrication/hybridization and detailed characterization. We present below the obtained results in comparison with the standard AlGaAs/GaAs QWIP performance.

This chapter starts with a discussion on the impact of the detector parameters on the FPA performance and related material system characteristics. This discussion will provide the basis for the interpretation of the results including the comparison of two different material systems for QWIPs. The chapter continues with the description of experimental procedures and the presentation of the results and discussion.

## 2.1 Impact of Device Gain on FPA Performance

The photoconductive gain of a QWIP is defined as the ratio of the drift distance to the device length where the drift distance is the average distance travelled by a photoexcited electron before it is captured by a quantum well. It is a well-known fact that the gain of the device does not have any effect on the sensitivity of a discrete sensor since both the signal and the noise of a BLIP sensor increases linearly with the device gain as reflected by the following expression [38, 39] for the detectivity of a BLIP sensor which does not include the detector gain,

$$D_{BLIP}^* = \frac{\lambda_p}{2hc} \sqrt{\frac{\eta_p}{\phi_b}} \quad (2.1)$$

In the above expression,  $\phi_b$  is the photon flux density, and  $\eta_p$  and  $\lambda_p$  are the peak quantum efficiency and responsivity wavelength, respectively.

The following expression [87] defines the temporal NETD of a detector which is not coupled to an ROIC. Since the detectivity ( $D^*$ ) of the BLIP sensor is independent of the gain, a relation between NETD and gain is not established. In the expression,  $f/\#$  is the f-

number of the optics,  $A_D$  is the detector area,  $T(\lambda)$  is the transmission of the atmosphere,  $M_{\lambda_{Target}}$  is the spectral exitance of the target, and  $\Delta f$  is the measurement bandwidth which is related to the integration time ( $\tau$ ) as  $\Delta f^{1/2} = (1/2\tau)^{1/2}$ .

$$NETD = \frac{4f/\#^2 \sqrt{\Delta f}}{\sqrt{A_D} \int_0^\infty T(\lambda) D^*(\lambda) \frac{dM_{\lambda_{Target}}(\lambda)}{dT} d\lambda} \quad (2.2)$$

As seen from expressions (2.1) and (2.2), the NETD of the discrete sensor can be decreased (the performance is improved) only by increasing the quantum efficiency resulting in higher detectivity.

The above discussion is valid for a discrete sensor. On the other hand, when the detector is coupled to the read out integrated circuit (ROIC), extrinsic noise sources in addition to the detector noise influence the SNR of the FPA/ROIC hybrid. Additionally, a relation between the gain and NETD is established through the  $\Delta f = 1/(2\tau)$  term since  $\tau$  is limited by the integration capacitors of the ROIC [88]. Higher gain (while not offering better SNR) results in more rapid filling of the ROIC integration capacitors limiting  $\tau$  and increasing NETD. Therefore, it may be advantageous to operate the sensor with a low device gain in order to allow a larger integration time if the photon flux is sufficiently large and the integration time is not limited by high frame rate requirement. On the other hand, if the device is used with low gain under low photon flux (large  $f/\#$ , low background radiation etc) and/or high frame rate (short integration time), the SNR of the FPA/ROIC hybrid may be limited by the read out noise instead of the detector noise. Small device gain under these conditions results in both the detector signal and noise being small leading to read noise limited SNR in the FPA/ROIC hybrid. The NETD of the FPA under such conditions can be expressed as [38]

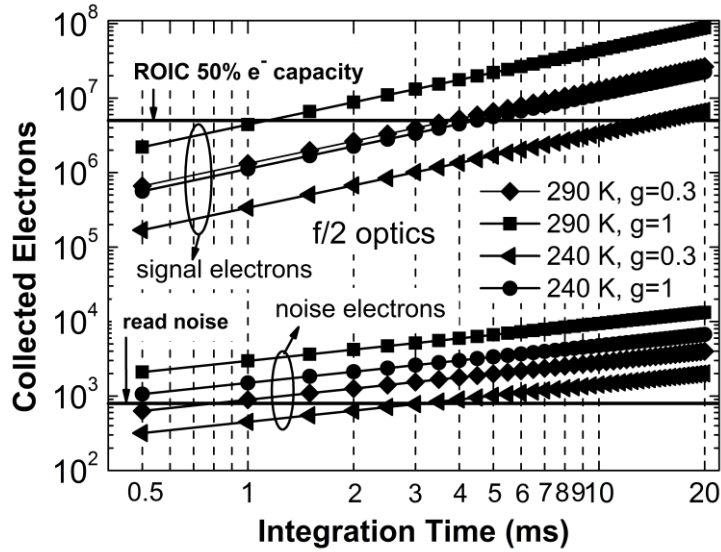
$$NETD = \frac{kT^2 Q_{ROIC}}{\phi_b q\eta g\tau}. \quad (2.3)$$

In the above expression,  $Q_{ROIC}$  is the ROIC noise charge. If the integration time is limited by the requirements of high speed imaging (high frame rate) application or the background photon flux is too low to saturate the ROIC capacitors, the relation between  $\tau$  and  $g$  disappears making the NETD of the FPA inversely proportional to the device gain

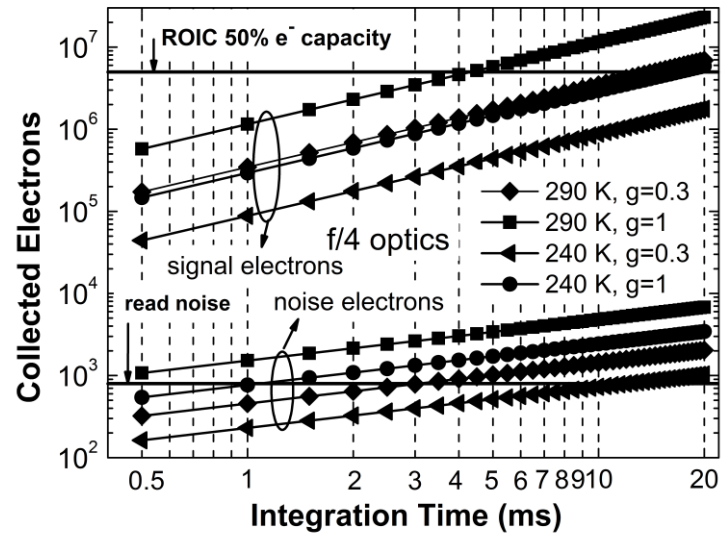
[89]. Under this condition, it is advantageous to have both large quantum efficiency and high gain in order to preserve the SNR of the hybrid at a value comparable to that of the discrete sensor [89].

**Figure 2.1** shows the noise- and photo-electrons generated by a fully BLIP QWIP FPA pixel ( $20 \times 20 \mu\text{m}^2$ ) with a peak quantum efficiency of 10% at  $8.5 \mu\text{m}$  and a cut-off wavelength of  $9 \mu\text{m}$  while the detector is looking at blackbody targets at 240 and 290 K with  $f/2$  and  $f/4$  apertures, different integration times and two different gains of 0.3 and 1 [89]. The noise ( $800 e^-$ ) and 50% electron capacity ( $5 \times 10^6 e^-$ ) levels of a typical read-out circuit are also shown in the figure for comparison. It should be noted that the collected photo-electrons will fill only 13% of the capacitors of a typical ROIC when operated with  $g = 0.3$ ,  $f/2$  and 1 ms integration time even when looking at room temperature scene [89]. In case the integration time is limited by the application at 4 ms, a gain level of 1 is needed in order to fill half of the integration capacitors of a typical ROIC while looking at 290 K target with  $f/4$  aperture. In addition to many other applications, tracking of rapidly moving targets or utilization of micro-scanning for resolution enhancement call for short integration times requiring high gain and responsivity. Only sensors with a sufficiently large conversion efficiency and sensitivity may fully comply with the requirements of these systems operating under strict conditions.

The maximum gain achievable with an AlGaAs/GaAs QWIP having a typical number of periods is around 0.3 [39]. When the noise level (in the range of  $500\text{-}1000 e^-$ ) and 50% electron capacity ( $5 \times 10^6 e^-$ ) levels of a typical read-out circuit are considered, it is obvious that the performance of the FPA/ROIC hybrid will be better in the case of larger gain especially when it is looking at a cold target. It is worth mentioning that the adaptation of a low gain sensor to different conditions may not be possible by changing the ROIC gain. The ROIC noise does not decrease linearly with increasing ROIC gain, and the read noise exceeds the detector noise under short integration time and/or low background conditions resulting in a low SNR due to the low detector signal [89].



(a)



(b)

**Figure 2.1.** Noise and photo-electrons generated by a  $20 \times 20 \mu\text{m}^2$  FPA pixel with different gains and background temperatures (a)  $f/2$  aperture, (b)  $f/4$  aperture [89]

A desirable QWIP with flexible behavior adaptable to different conditions should display characteristics similar to those presented in **Figure 2.2** [89]. The variable gain should be adjusted to low values under sufficiently high photon flux and integration time, while it should be set at a large value under low photon flux and/or low  $\tau$ . Constant detectivity

with varying device gain allows gain switching without degradation in the sensitivity of the FPA pixels.

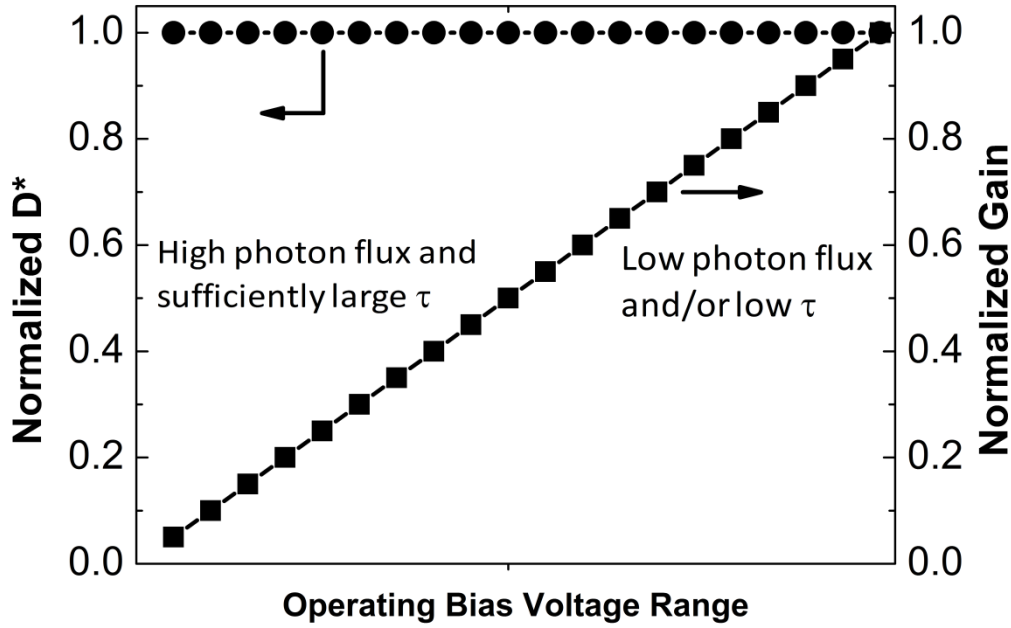


**Figure 2.2.** Gain and sensitivity of a desirable QWIP with flexible characteristics adaptable to different conditions [89].

## 2.2 Feasible LWIR QWIP Material Systems

Based on the above discussion, it should be clear that the limitations of the standard QWIP can mostly be overcome if sufficiently large quantum efficiency and bias adjustable gain (in a wide enough range) are provided by the sensor. While high enough  $\eta$  increases the operation temperature of the detector, adjustable gain offers flexibility to adapt the sensor to different operating conditions.

Based on the experimental results from literature on the QWIP drift distance (which is proportional to gain) offered by various material systems, the drift distance (and gain) seems to be related mostly with the properties of the barrier material [59,90-93]. The relative magnitude of the gain exhibits different characteristic under low and high E-

fields. Materials with larger energy separation between the central ( $\Gamma$ ) and satellite conduction band valleys (e.g.  $L$ ) tend to provide higher gain under moderate and large E-fields while the low bias gain seems to be somehow related with low field mobility. Among the feasible material systems, InP/InGaAs system seems to offer the maximum gain under large bias while providing flexibility to adjust this parameter in a wide range.

The limited gain range offered by the  $\text{Al}_x\text{Ga}_{1-x}\text{As}/\text{GaAs}$  material system (with  $x \sim 0.3$ ) results in relatively low conversion efficiency which may be a problem in a certain group of applications as described in the gain discussion. While the GaAs/InGaAs system seems to be better in this sense, the large lattice mismatch in this material system is not desirable.

The most important advantages of the QWIP technology that should not be sacrificed while selecting a material system are uniformity, reproducibility and stability. InP/InGaAs material system has successfully been utilized for the production of various semiconductor devices in large volume which is an indication of the high level maturity of this material system. When the low electron effective mass in InGaAs (as a quantum well material) is combined with the large  $\Gamma - L$  energy spacing in InP (as a barrier material), the resultant combination displays potential for QWIP applications promising relatively large quantum efficiency together with larger photoconductive gain (under moderate and large bias). It should also be noted that the InP/InGaAs material system when combined with the AlInAs/InGaAs system provides completely lattice matched epitaxial structure for the implementation of dual band QWIP FPAs [72, 94]. The GaAs based alternative to lattice matched AlInAs/InGaAs system for mid-wavelength infrared sensors is the lattice mismatched AlGaAs/InGaAs material system.

There are reports suggesting that the QWIPs based on the lattice matched InP/In<sub>0.53</sub>Ga<sub>0.47</sub>As material system provide cut-off wavelengths around 8.5  $\mu\text{m}$  which is rather short for thermal imaging in the LWIR band [59]. The solutions to extend the peak and cut-off wavelengths to desirable values (such as 8.5 and 9  $\mu\text{m}$ ) are the replacement of the quantum-well (QW) material In<sub>0.53</sub>Ga<sub>0.47</sub>As with InGaAsP (1.55  $\mu\text{m}$  bandgap) [63, 65], or utilization of strain as an additional bandgap engineering parameter [60] by

lowering the In mole fraction in InGaAs below 0.53. Another lattice matched solution as demonstrated by Jelen and Razeghi [94] is the utilization of the InP/Al<sub>x</sub>Ga<sub>y</sub>In<sub>1-x-y</sub>As material system at the lattice matched composition. This material system allows the fabrication of very long wavelength infrared (VLWIR) QWIPs while maintaining lattice match and the desirable properties of InP as the barrier material. Furthermore, the growth of AlGaInAs is relatively easy when compared with the quaternary InGaAsP which includes two group V elements [94]. While this material system seems to be the only feasible solution (avoiding large lattice mismatch) for VLWIR sensing on InP substrate, the replacement of quantum well material with a smaller electron effective mass material, In<sub>x</sub>Ga<sub>1-x</sub>As ( $x \sim 0.5$ ), is expected to provide improvement for LWIR sensing.

It has experimentally been demonstrated at the FPA level [89, 95], that InP/In<sub>x</sub>Ga<sub>1-x</sub>As QWIPs with  $x \sim 0.5$  provide desirable spectral characteristics as needed by LWIR thermal imagers. Based on the above discussion and the results presented in the following sections, it can be concluded that strained InP/In<sub>x</sub>Ga<sub>1-x</sub>As material system has high potential for building a LWIR QWIP that can compete with the other technologies in a wider group of applications while maintaining its low cost nature.

### **2.3 InP Based QWIPs: The Origin of Superiority**

Larger gain achievable in InP/InGaAs QWIPs is generally attributed to the electron transport properties of the binary material InP. However, the dependence of the gain on the material properties is not straightforward. The drift distance depends both on the velocity of the excited electrons and the carrier lifetime. The characteristics of the electron velocity in a QWIP is significantly different than steady-state velocity-field relation in bulk material due to the velocity overshoot of the electrons excited from the preceding wells and the reflections of the electrons at the interfaces between the barriers and wells. Indeed, it has been shown through ensemble Monte Carlo (EMC) simulations that the low field electron mobility in a QWIP is significantly lower than that in bulk material [96].

It may also be possible to relate the significantly higher responsivity in InP/InGaAs QWIPs partially to avalanche multiplication [97] which is not commonly observed in AlGaAs/GaAs QWIPs. The absence of this effect in AlGaAs/GaAs QWIPs was attributed to alloy scattering in the ternary barrier. However, it is also possible to relate this observation to smaller  $\Gamma - L$  energy spacing in AlGaAs preventing the electrons from gaining large energies from the E-field before being captured. At first look, InP/InGaAs QWIPs should be more prone to impact ionization due to significantly larger  $\Gamma - L$  energy spacing. A more detailed discussion on this issue will be provided during the presentation of the results.

In order to explain the dependence of the moderate and large bias gain on the  $\Gamma - L$  energy separation in the barrier material, the calculated (through ensemble Monte Carlo simulations) drift distance versus average E-field in the device for a 16-period LWIR  $\text{Al}_{0.3}\text{Ga}_{0.7}\text{As}/\text{GaAs}$  QWIP with 500 Å thick barriers and 44 Å thick QWs is shown in **Figure 2.3** [90, 96]. The drift distance obtained when (only) the  $\Gamma - L$  energy separation is artificially increased in the barrier material (AlGaAs) to be equivalent to that in InP is also shown in **Figure 2.3** displaying nearly an order of larger gain under large bias. Noting that the  $\Gamma$ -valley electron effective mass in InP is close to that in  $\text{Al}_{0.3}\text{Ga}_{0.7}\text{As}$ , the results presented in **Figure 2.3** for larger  $\Gamma - L$  energy spacing are expected to be close to those in InP/InGaAs QWIPs under low fields.

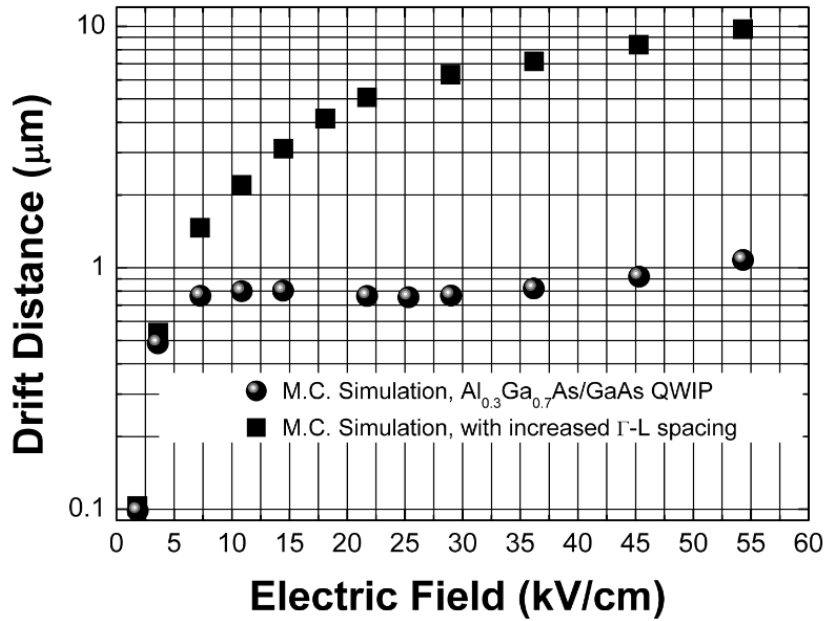


**Figure 2.3.** Simulated drift distance vs. the average electric field for  $\text{Al}_{0.3}\text{Ga}_{0.7}\text{As}/\text{GaAs}$  QWIP (circles). Upper data points (squares) show the results obtained after artificially increasing the  $\Gamma - L$  energy separation equivalent to that in InP [90].

The predictions of the ensemble Monte Carlo simulations are in good agreement with the experimental results on  $\text{Al}_x\text{Ga}_{1-x}\text{As}/\text{GaAs}$  QWIPs with  $x \sim 0.3$ . The results showed that larger gain in InP/InGaAs QWIPs under moderate and large bias can be explained solely by the larger  $\Gamma - L$  energy separation in the barrier material. In other words, referring to the contribution of avalanche multiplication (which was not included in the simulations) in order to explain the experimentally observed high responsivity in InP/InGaAs QWIPs is not necessary. Larger  $\Gamma - L$  energy separation in the barrier material of the InP/InGaAs QWIP leads to heating of electrons to larger kinetic energies without  $\Gamma - L$  intervalley scattering which creates an efficient capture path through the L valley quantum well decreasing the drift distance due mainly to the reduced lifetime [96]. Therefore, larger photoexcited electron lifetime (not larger electron velocity) seems to be the main reason for larger moderate and large bias gain in InP/InGaAs QWIPs [90]. The drift distance-E-field characteristics should not be expected to follow the bulk material drift velocity-field characteristics due to the different velocity-field characteristics of the multi

quantum well structure and the dependence of the photoexcited carrier lifetime as well on the E-field.

InP/InGaAs QWIPs also offer advantage on the quantum efficiency side. The electron effective mass ratio in  $\text{In}_x\text{Ga}_{1-x}\text{As}$  with  $x \sim 0.5$  is  $\sim 0.04$  which is smaller than that in GaAs by a factor of  $\sim 1.7$ . The dependence of the absorption efficiency on the effective mass (expected to be inversely proportional to  $m^*$ ) results in considerably higher  $\eta$  in InP/InGaAs QWIPs under the same quantum well two dimensional electron density ( $n_{2D}$ ). However, after interpreting the following relation of the  $n_{2D}$  with  $E_F$  and  $m^*$ , which can be derived from Equation 1.19, it should be noted that the Fermi level ( $E_F$ ) in InP/InGaAs QWIPs should be located at a higher level due to the lower density of states,

$$n_{2D} = \frac{m^*kT}{\pi\hbar^2} \ln(1 + e^{E_f/kT}). \quad (3.1)$$

Noting that  $\eta$  linearly depends on  $n_{2D}$  (Equation 1.15), and the dark current increases exponentially with  $E_F$  (Equation 1.17), the optimum doping densities (maximizing detectivity or BLIP T) for InP/InGaAs QWIPs should be different than those in AlGaAs/GaAs QWIPs. Higher quantum efficiency in InP/InGaAs QWIPs enable the use of a smaller doping density for a targeted responsivity. This results in a larger photocurrent to dark current ratio and larger BLIP temperature with a properly selected quantum well electron density. Under the background limited operating conditions, the InP/InGaAs QWIP is expected to be always superior to AlGaAs/GaAs QWIP with the same quantum well electron density due to larger quantum efficiency and larger BLIP detectivity ( $D_{BLIP}^* \propto \sqrt{\eta}$ ).

As an experimental demonstration of the above discussions, the thermal images taken with  $640 \times 512$  AlGaAs/GaAs and InP/InGaAs QWIP FPAs are presented in **Figure 2.4**. Both FPAs were fabricated in our laboratory including the MBE growth of the epilayers [89]. While the image quality of the AlGaAs/GaAs FPA is degraded under sub-millisecond integration times, the thermal image provided by the InP/InGaAs QWIP FPA still reflects high sensitivity operation.

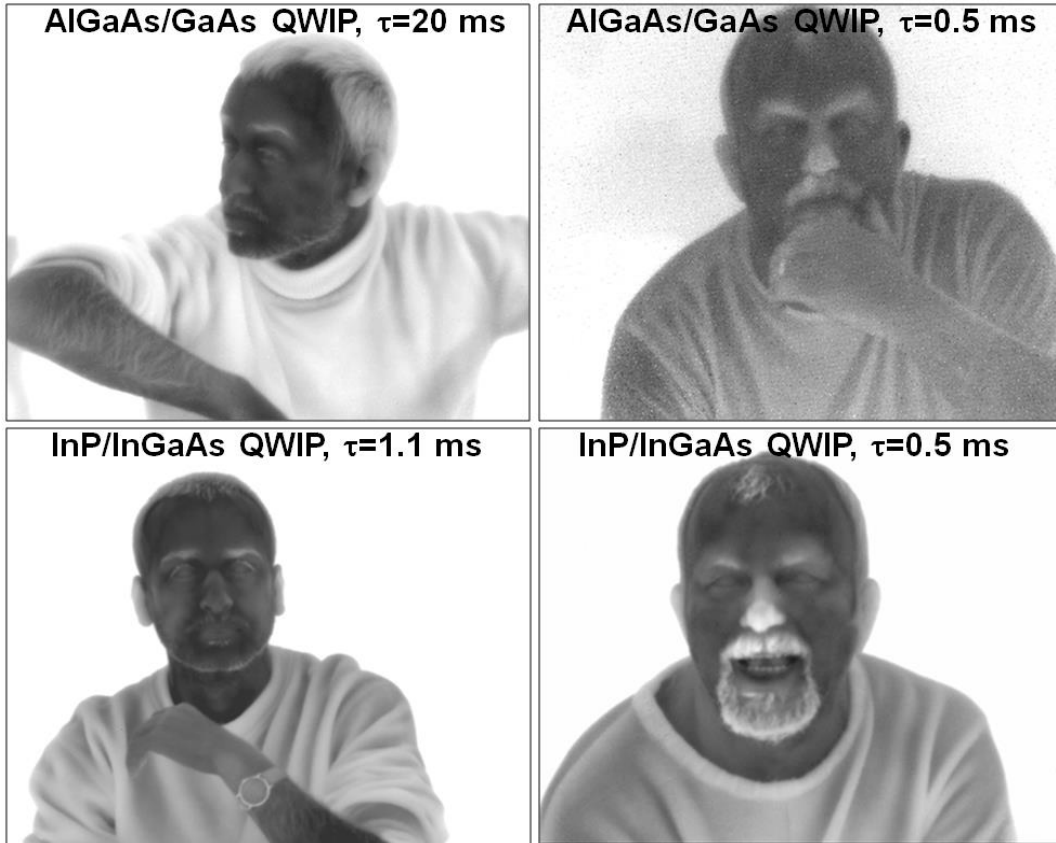


**Figure 2.4.** Thermal images taken with the two FPAs under different conditions. In the case of the InP/InGaAs QWIP FPA, the detector bias is adjusted to have nearly half filled ROIC capacitors while looking at 300 K background. AlGaAs/GaAs QWIP FPA in the short (0.5 ms) integration mode is operating at a bias voltage providing the optimum detectivity [89].

In spite of the high potential they display, there has been limited work on the use of the material systems on InP substrates for QWIPs, especially at the FPA level [62,65,89,95,98-101]. In this work, considerable enhancement in the InP/InGaAs QWIP performance has been achieved through improving both device epilayer structure and processing techniques.

## 2.4 InP/InGaAs Multi Quantum Well Epilayer Design

In this study, all of the relevant design parameters are investigated in the same course, unlike the similar efforts which focus on a single parameter at a time. It is aimed to provide a basis for converging into an optimum QWIP design under different operational requirements.

A typical QWIP epilayer structure with related fundamental parameters are shown in **Figure 2.5** and shortly explained below. All the investigated structures use the same design outline with variations on the parameters.

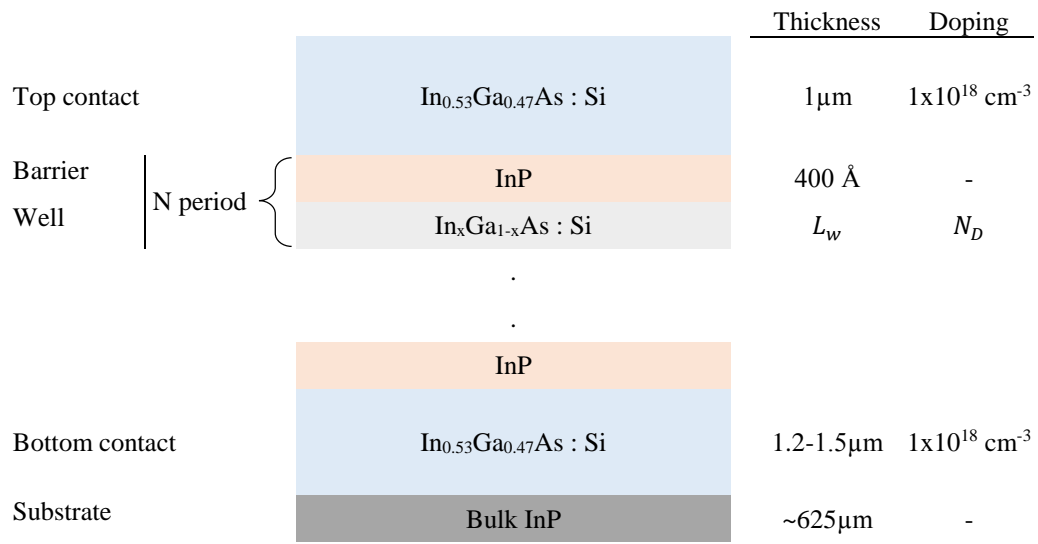


**Figure 2.5.** QWIP epilayer structure and design parameters

In this structure, the quantum well stack is terminated with lattice matched  $\text{In}_{0.53}\text{Ga}_{0.47}\text{As}$  contact layers from top and bottom. Both contact layers are heavily n-type doped with silicon ( $\sim 1 \times 10^{18}\ \text{cm}^{-3}$ ) in order to provide good electrical contact to the quantum well stack. The thickness of the top contact layer is set to  $1\ \mu\text{m}$  to facilitate the fabrication of the diffraction gratings optimized for LWIR window. The bottom contact thickness is set to  $1.2$  or  $1.5\ \mu\text{m}$  considering quantum well stack thickness and the etching process tolerances.

The quantum well stack is composed of InP barriers and  $\text{In}_x\text{Ga}_{1-x}\text{As}$  wells. In all of the investigated structures, InP barriers are undoped and have 400 Å thickness. The thickness of the barriers are selected large enough to prevent ground state tunneling [102] and small enough to keep a reasonable total well stack thickness. As the transport through the well stack is mostly determined by the barriers, keeping the same barrier length also ensures a fair comparison of different designs.

The quantum well parameters determine the most of the detector's characteristics. The conduction band discontinuity, which can be adjusted with InGaAs composition ( $x$ ), and the well width ( $L_W$ ) determines the energy states in the well and therefore the spectral properties of the detector. The usability of strained InGaAs/InP system in the 8-11 μm spectral range has already been shown in literature [60]. The well width and well composition are among the investigated parameters in this work. The doping level ( $N_D$ ) of the well is an important parameter which directly affects the responsivity, detectivity and the operating temperature as discussed in the introductory chapter. There have been some efforts dedicated to the optimization of the doping level for this material system [103] which yielded results similar to this work. The number of the periods in the multi quantum well structure is selected to provide high absorption while keeping a large enough device gain.

A total of seven different epilayer structures have been investigated in this study. First two of them were grown by commercial supplier while the rest were home-grown by solid source molecular beam epitaxy. The design parameters of the investigated epilayer structures (enumerated as S1... S7) are shown in **Table 2.1**.

**Table 2.1.** Design parameters of the investigated epilayer structures

	<i>S1</i>	<i>S2</i>	<i>S3</i>	<i>S4</i>	<i>S5</i>	<i>S6</i>	<i>S7</i>
$x$	0.45	0.48	0.48	0.48	0.51	0.48	0.48
$L_W$ (Å)	60	60	57	50	50	57	57
$N_D$ (cm <sup>-3</sup> )	4x10 <sup>17</sup>	4x10 <sup>17</sup>	5x10 <sup>17</sup>	5x10 <sup>17</sup>	4x10 <sup>17</sup>	8x10 <sup>17</sup>	2.7x10 <sup>17</sup>
$N$	40	40	60	40	36	40	40

The study starts with the growth of the epilayer structures. The growth procedure is described in the next section including some background information on molecular beam epitaxy and the growth of InGaAs/InP structures.

## 2.5 MBE Growth of InGaAs/InP QWIPs

The term *molecular beam epitaxy* introduced in 1970 by A. Cho [104] describes a process in which the crystal growth on a heated crystalline surface takes place by the adsorption of atomic/molecular beams in an ultra-high vacuum environment. This method is suitable for the preparation of many classes of materials including semiconductors (such as III-V, IV-IV, II-VI, and IV-VI compounds), oxides, magnetic materials and metals. In the archetypal case of III-V compound semiconductors, MBE is an essential way of material synthesis.

The core configuration of a MBE system includes an introduction chamber, a buffer chamber and a growth chamber. The vacuum level and the cleanliness standard improves progressively toward the growth chamber. This compartmentalisation of the vacuum volume allows the transfer of a sample between atmosphere and growth chamber in minutes while keeping the growth chamber under ultra-high vacuum for extended periods of time (e.g. several years). The introduction (or loading) chamber is the chamber which is opened to atmosphere in each sample loading cycle. The sample is transferred to the buffer chamber after a certain vacuum level (e.g.  $10^{-6} - 10^{-7}$  torr) is reached in the

introduction chamber. The buffer chamber includes an outgassing oven to drive-off atmospheric residues (mostly water) on the sample. The outgassing of the InP and GaAs substrates is typically done for 1 hour at 300 °C and 400 °C, respectively. Following the outgassing, the sample is transferred to the growth chamber. The schematic of the growth chamber of the Riber Epineat which is typical to all vertical MBE systems, is shown in **Figure 2.6**. The growth chamber is a stainless steel vessel containing a heatable substrate holder, sources, shutters, liquid nitrogen panels, measurement instruments (ion gauges, quadrupoles, pyrometers, etc.) and in-situ characterization instruments (reflective high energy electron diffraction, spectral ellipsometry, absorption band-edge spectrometry, etc.). The substrate holder heats and rotates the loaded wafers, and the temperature is set by the closed loop controllers uniformly throughout the wafer. The surface temperature of the substrate is also measured with an optical pyrometer.

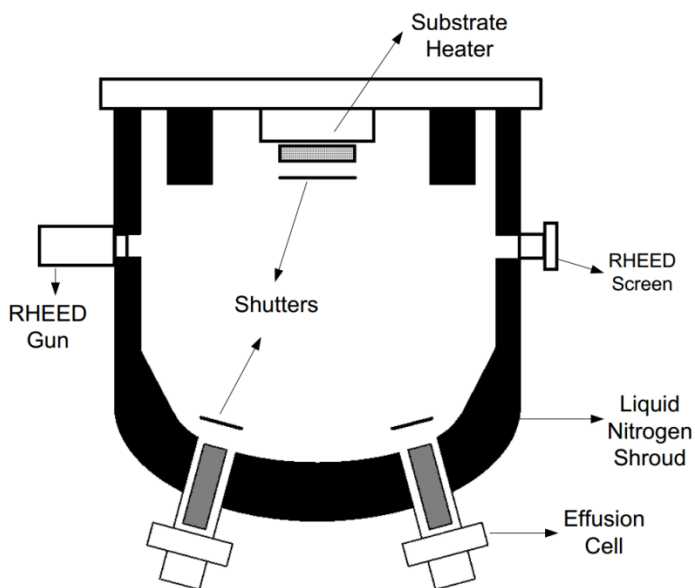


**Figure 2.6.** Typical growth chamber cross section for a vertical MBE system [105].

The sources generate beams by thermal evaporation or sublimation of the materials which are in atomic (In, Ga, Al, Si, Be) or molecular ( $As_2/As_4$ ,  $P_2/P_4$ ) forms. The

materials are contained in crucibles which are made of pyrolytic boron nitride or similar low vapor pressure refractory materials. The axes of the sources, therefore the beams, converge on the surface of the substrate. Group IIIA and IVA materials are directly evaporated from the heated crucibles whereas As and P require additional stages for reduction of tetramers to dimers (cracking). Furthermore, solid source P cells requires proper handling of allotropic forms (red, white and black phosphorus) which needs one more stage. *The valved cracker cell* concepts for As and P are illustrated in **Figure 2.7**. The beams emerging from the sources are interrupted by the shutters located above the sources and below the substrate holder. The growth chamber vacuum level is continuously preserved by cryopumps, ion pumps and titanium sublimation pumps. During crystal growths, base pressure of the growth chamber is further decreased (e.g.  $\sim 10^{-11}$  torr) by introducing liquid nitrogen to the cryo-panels. The pressures of all chambers and beam equivalent pressures of the materials are measured with Bayard-Alpert gauges located at different points of the system. The composition of the residual gases in the growth chamber is measured with a quadrupole mass spectrometer.

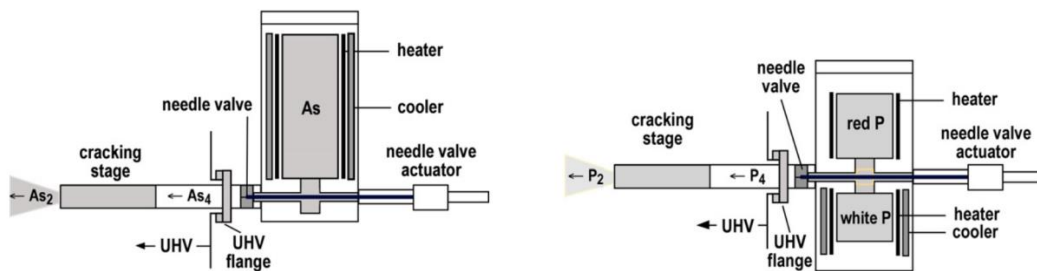


**Figure 2.7.** Schematic cross-sectional view of As and P valved cracker cells [106].

The RHEED is an essential in-situ tool for MBE systems which provides real time surface inspection during growth. The RHEED system consists of an electron gun (12 kV in this case) and a fluorescent screen installed on the growth chamber facing each other. The collimated beam of electrons generated by the gun hits the substrate surface at grazing angle ( $0.5^\circ - 2.0^\circ$ ) and form a diffraction pattern on the screen. This diffraction

pattern unveils the evolving conditions on the surface including surface reconstruction, roughness, oxide desorption and growth rate.

In a typical growth event, the substrate is first loaded and outgassed in the buffer chamber. In the meantime, the sources are heated to growth temperatures from their stand-by temperatures, and their fluxes are adjusted to the desired values. Once the outgassing is completed and the fluxes are set, the wafer is transferred to growth chamber and heated for *oxide desorption*. During the thermal desorption of the thin surface oxide, group V elements in the substrate lattice are evaporated as well due to excess temperature, therefore this procedure is performed under a suitable group V flux (typically P for InP and As for GaAs) in order to compensate the evaporation loss. After oxide desorption and surface reconstruction, the substrate is cooled down to growth temperature. The growth is initiated by the opening of the source shutters. The shutters are computer controlled and the shutter sequences are programmed in a recipe. After the completion of the epilayer structures, substrate is cooled down and removed from the system.

In the growths of InGaAs/InP QWIP structures, arsenic is used as tetramers ( $As_4$ ) whereas phosphorus is cracked with a cracker temperature as low as possible to minimize background doping in the barriers [107]. The substrate deoxidization is done under  $P_2$  flux until an indium stabilized surface is reached as inspected from RHEED. The growth rates used the investigated epilayer structures, were  $0.62 \mu\text{m/h}$  and  $1.2 \mu\text{m/h}$  for InP and InGaAs, respectively. The growth temperature during InGaAs layers were manipulated manually due the self-heating by infrared absorption of the low bandgap InGaAs. The temperature versus doping concentration relation for the silicon cell was previously constructed with calibration growths.

The crystal quality and the epilayer structures of the grown wafers were verified with x-ray diffraction measurements. An example rocking curve (S4) is shown in **Figure 2.8**.

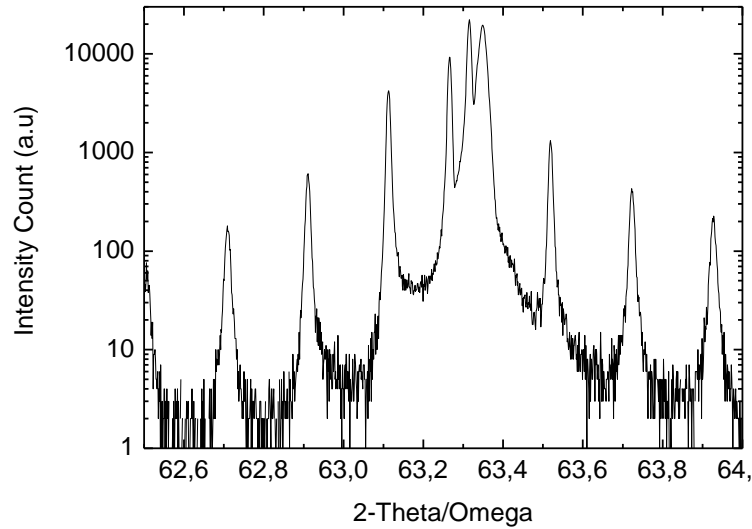


**Figure 2.8.** The rocking curve of S4 epilayer structure

Both large area test detectors and focal plane arrays are fabricated using the grown epilayer structures. The fabrication processes are summarized in the next section.

## 2.6 InP/InGaAs QWIP Fabrication

After x-ray diffraction measurements, large area test detectors are fabricated in a quick manner for a preliminary inspection of the detector performance. The large area test detector fabrication includes only mesa etching and ohmic contact deposition steps. The mesa etching is done in a single step with HBr:Br (typically 200:1) and standard AuGe/Ni/Au ohmic contact is used. The electrical contact to the 200x200  $\mu\text{m}^2$  or 300x300 detectors is established via direct wirebonding on top of the mesas as shown in **Figure 2.9**.

The preliminary measurements are performed on the large area detectors in order to verify the detector behavior. If the first observations comply with the expectations, the wafer is set for FPA fabrication.

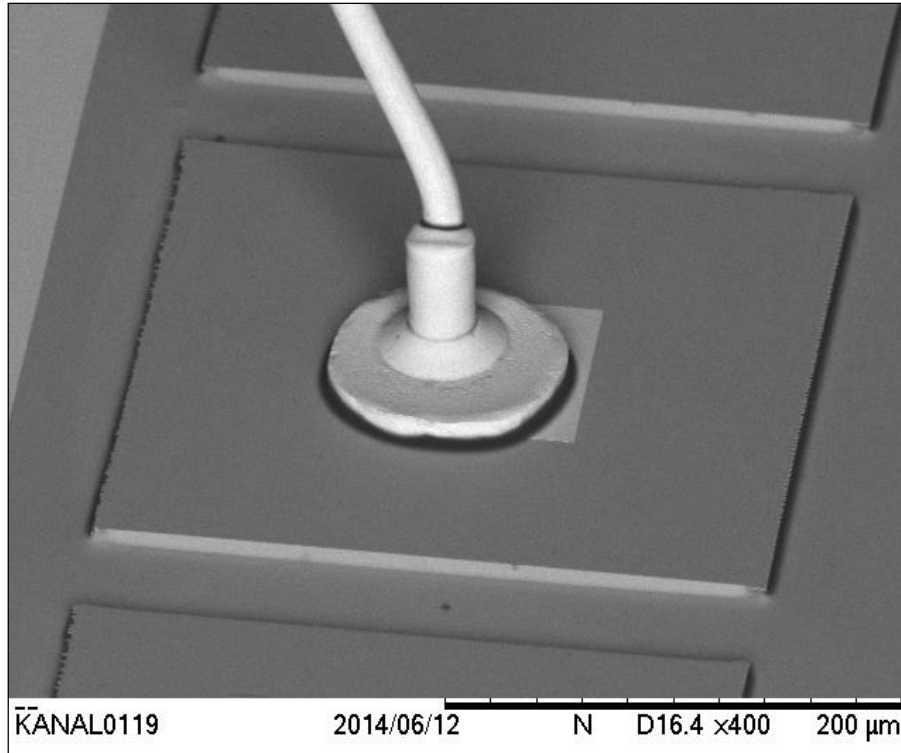


**Figure 2.9.** SEM image of large area test detectors

The FPA fabrication processes in this work were done at die scale, one by one for each sample. These fabrication steps are illustrated in **Figure 2.10**. All the required lithography steps are performed with a Suss MicroTec MJB4 mask aligner in the contact mode.

The fabrications start with the formation of the metal alignment marks with lift-off method. The quality of the alignment marks significantly affects the alignment accuracy of the following process steps. The second step is the formation of the diffraction gratings by inductively coupled plasma reactive ion etching (ICP-RIE). The lithography tolerance for this step is low and the wet etching method is not applicable due to anisotropy requirement.  $\text{BCl}_3$  or  $\text{SiCl}_4$  based gas combinations are used for etching of the top InGaAs layer. The third step is the definition of the pixels by mesa etching. The  $\text{HBr}:\text{Br}$  solution (or equivalent bromine based solutions) can be used to delineate pixels in a single step. If the mesa edges are aligned along  $\langle 1,1,0 \rangle$  and  $\langle 1,-1,0 \rangle$  directions (major and minor

flats) there will be a difference in the sidewall slopes due to directional selectivity of the etchant. This can be prevented by rotating the sample  $45^\circ$ . The mesa profile etched in this fashion is shown in **Figure 2.11**. In this picture quantum well stack is also visible. It must be kept in mind that bromine and related solutions are not compatible with most of the metals including gold and titanium. Any exposed metals (e.g. alignment marks) will cause surface damage on the surrounding structures which will progressively worsen and spread as the etching continues.

In addition to wet etching, anisotropic dry etching with ICP-RIE is also used in order to increase the fill factor. Dry etching is always followed by a short wet etching step (several hundreds of nanometers) in order to recover the surface condition of the mesa sidewalls. In the fourth and fifth steps, ohmic contact (AuGe/Ni/Au) and reflector metals (Ti/Au) are deposited and patterned using lift-off method. Small ohmic contact area and large reflector area is preferred in order to obtain good second pass reflection with low absorption. In the next step, mesa sidewalls are spin coated with a suitable passivation material and the contact regions are uncovered. Following the passivation step, under bump metallization and indium bump deposition via e-beam evaporation is done. This process is applied to readout chips as well. Approximately 5-6  $\mu\text{m}$  tall indium bumps are formed on both side before hybridization.

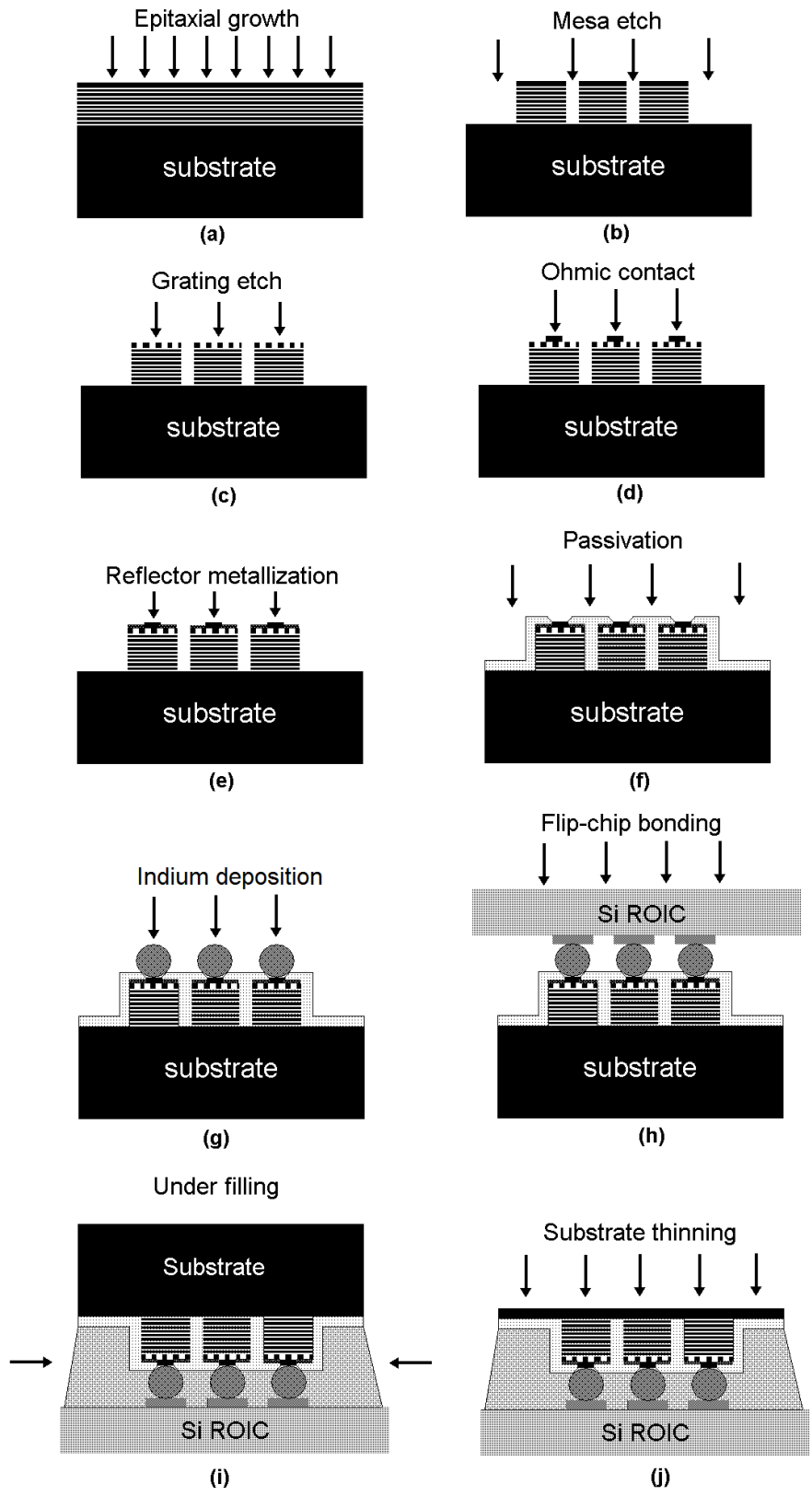


**Figure 2.10.** FPA fabrication steps [30]

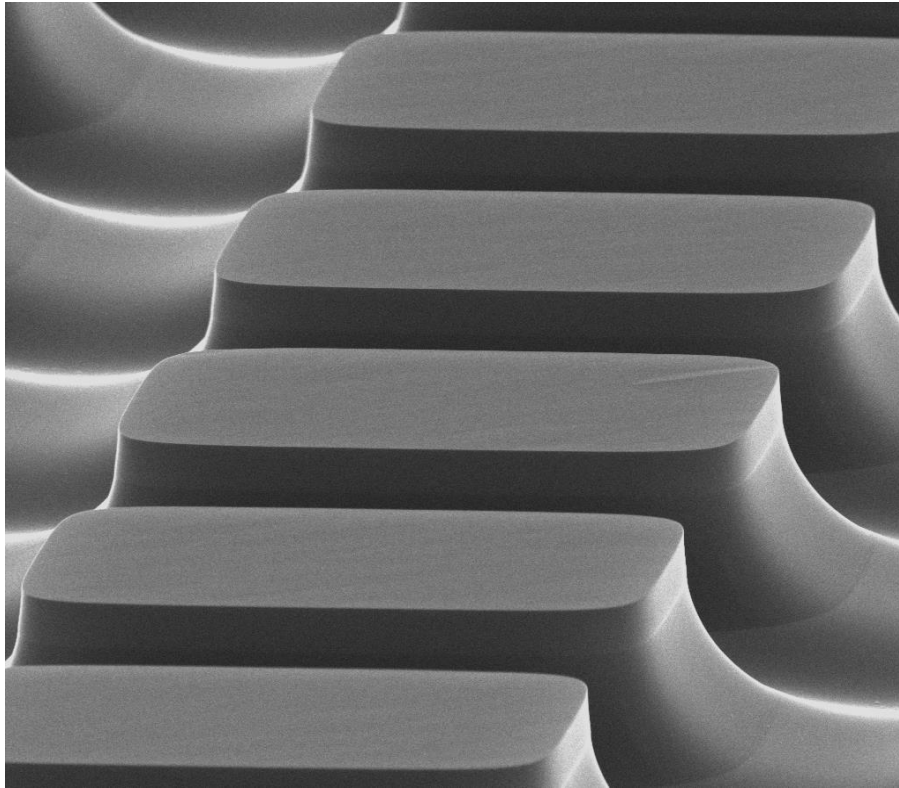


**Figure 2.11.** 25  $\mu\text{m}$  pitch mesa profile obtained with HBr:Br solution

After indium bump implementation, the wafer piece is diced and the FPA is extracted from the surrounding support pixels. The support pixels which are identical to FPA pixels, are saved for fanout coupling and testing. The FPA is flip-chip bonded to commercially available FLIR Systems' ISC9803 ROIC. The cold compression method is used during the flip-chip bonding which is done using a SET FC150 flip-chip bonder. A suitable low viscosity underfill epoxy is injected into the ROIC-FPA interface in order to improve the mechanical strength of the bonding. Finally, the substrate is thinned down to several micrometers thickness.

The FPA hybrid is placed on an 84 pin leadless chip carrier (LCC) and installed on a dewar for testing. Similarly, the support pixels, which are flip-chip bonded to fanout substrates, are placed on a LCC and installed on a dewar for pixel level characterization.

## **2.7 Characterization Setups**

The fanout substrates which host the support pixels, provide direct electrical access to the parallel connected pixel groups of 25. Consequently, electrical and optical characterization is performed on these pixels reflecting the performance of FPA pixels. Throughout the measurements, the temperature of the detector was monitored with a forward biased 2N2222 temperature diode placed on the fanout substrate.

### **2.7.1 I-V Measurements**

The current-voltage measurements are performed using a remotely controlled Keithley 238 source-measure unit. For the dark current measurements, the detector is completely blinded with a cold shield. The photo-current is obtained by subtracting the dark current at that detector temperature, from the total current generated while the detector is looking at 300 K background.

### **2.7.2 Responsivity Spectrum Measurements**

The responsivity spectra of the detectors are measured with a MIR-8000 Fourier transform infrared spectrometer. The connection diagram of the measurement setup is shown in **Figure 2.12**. In order to measure the responsivity spectrum of a detector, first, the spectral shape of the system's radiation source is normalized using the system's own DTGS detector. Then, the detector to be measured is replaced with the DTGS detector. The detector, which is installed in the dewar and cooled, is connected to the spectrometer over a current preamplifier. The computer controlled spectrometer runs in the transmission mode and measures the intrinsic response spectrum of the detector. This spectrum is used to calculate the peak factor for each detector.

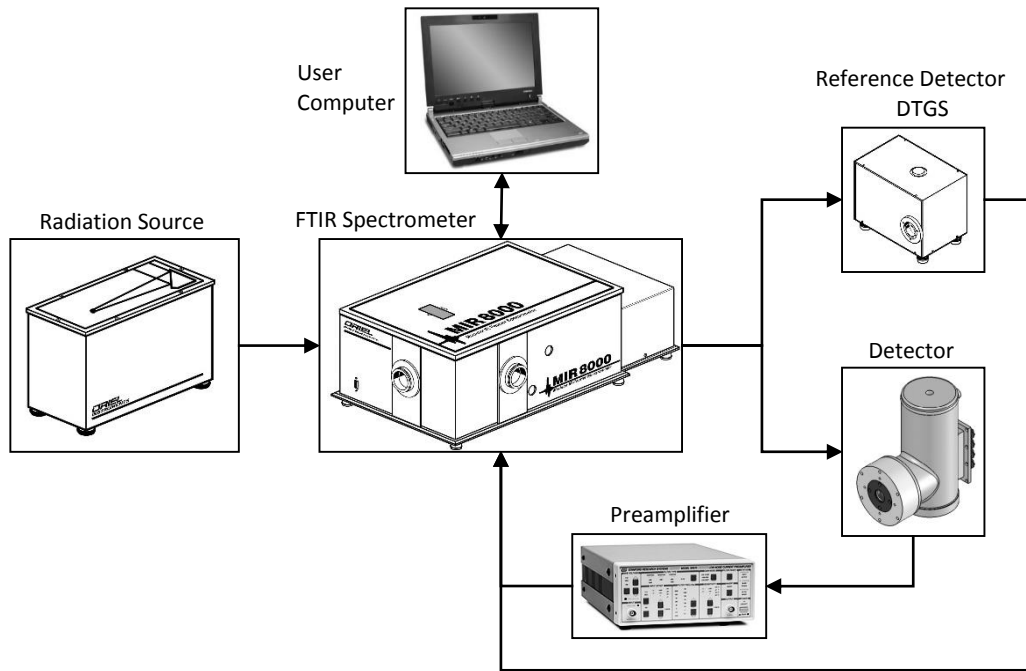


**Figure 2.12.** Responsivity spectrum measurement setup

### 2.7.3 Responsivity and Detectivity Measurements

The responsivity and detectivity measurement setup is shown in **Figure 2.13**. The blackbody with an integrated chopper provides a known amount of modulated radiation which falls on the detector installed in the dewar. The dewar outputs are connected to the current preamplifier which supplies the detector bias and collects the detector current. The amplified detector signal in response to modulated radiation is fed to lock-in amplifier which extracts the signal component at the modulation frequency. The output of the lock-in amplifier is handled by the software installed on the user computer. The software calculates the blackbody responsivity of the detector by dividing the generated detector signal to the amount of the radiation falling on the detector. The detector noise at the modulation frequency is measured with the detector looking to a steady room temperature scene in order to extract the noise of the detector. The detectivity of the detector is calculated using the measured responsivity and the noise by the software. The

peak responsivity and detectivity values are found by multiplying the obtained blackbody responsivity and detectivity with the peak factor.

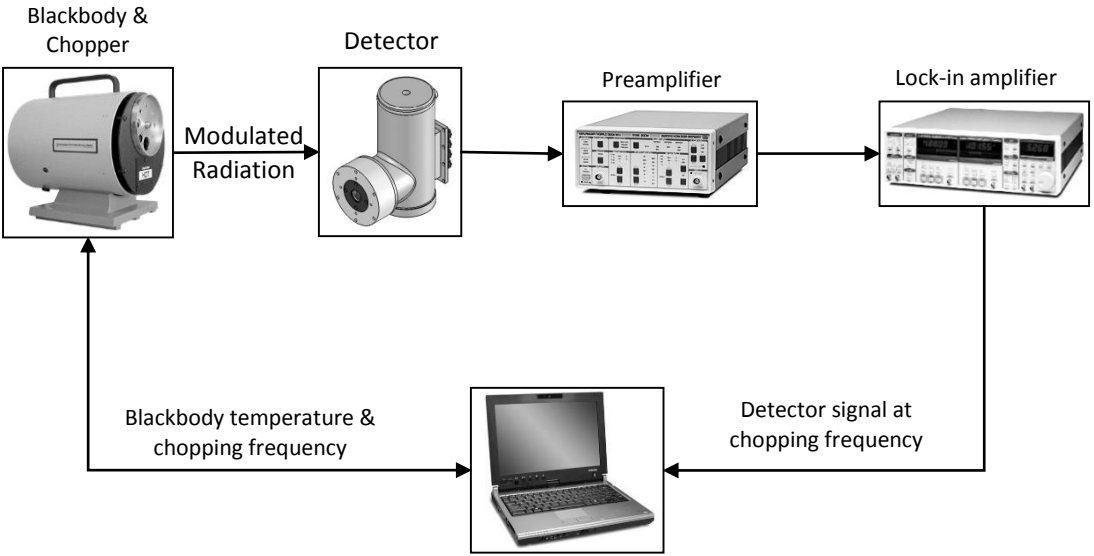


**Figure 2.13.** Responsivity and detectivity measurement setup

**2.7.4 NETD Measurement**

Unlike the above measurements, NETD measurement is performed on the hybridized FPA using 14 bit camera electronics and a large area differential blackbody source. The differential blackbody has two plates, one is left floating at room temperature (cold) and the other one (hot) is heated to have a certain temperature difference ( $\Delta T \sim 12^{\circ}C$ ) with the first one. Two sets of frames are captured with the camera while its field of view is entirely covered with the cold and hot plates in turn. The captured videos are averaged over frames to obtain the average signal level of each pixel while looking at cold and hot scenes. The difference of these two frames gives the response of the pixels to the  $\Delta T$  temperature difference in ADC counts. The standard deviation of each pixel over the frames of cold frame set is used to determine the noise of that pixel. Finally, the NETD value for each pixel is found by dividing its noise to its response and multiplying with

$\Delta T$ . If the pixel value located in the  $i^{th}$  row and  $j^{th}$  column of  $k^{th}$  frame is denoted by  $\rho_{i,j,k}$ , the NETD calculation for that pixel is given by equation

$$NETD_{i,j} = \frac{\sqrt{\frac{1}{N} \sum_{k=1}^N \left( \rho_{i,j,k} - \frac{1}{N} \sum_{k=1}^N \rho_{i,j,k} \right)^2}}{\frac{1}{\Delta T} \left[ \left( \frac{1}{N} \sum_{k=1}^N \rho_{i,j,k} \right) |_{T=RT+\Delta T} - \left( \frac{1}{N} \sum_{k=1}^N \rho_{i,j,k} \right) |_{T=RT} \right]} \quad (2.4)$$

where N denotes the number of frames collected, and  $\Delta T$  denotes the temperature difference between hot and cold plates.

The operability of the FPA is determined by discarding the pixels giving negative response or NETD value above three times the average. All the calculations are implemented on a MATLAB script and performed automatically once the frame sets are given.

## 2.8 Preliminary Characterization of Epilayer Structures

Using the fabrication procedures given in the previous section many test detectors were fabricated with the 7 epilayer structures described in **Table 2.1**. The design parameter variations among the samples were accordingly made to allow the extraction of the effects of changing the well width and indium content. The designed structures displayed bound-to-continuum or bound-to-quasibound type of transitions with peak absorption wavelength ranging between 8.4 and 9.1  $\mu\text{m}$ , except S3 which showed bound-to-bound transition type as verified by narrower spectral response and highly bias dependent responsivity. The peak responsivity / cut-off wavelengths and  $\Delta\lambda/\lambda_p$  of the detectors are 9.12 / 9.48 $\mu\text{m}$  and 9.6% for S3, and 9.04 / 9.60  $\mu\text{m}$  and 13.8% for S4. At the same well indium content ( $x = 0.48$ ), decreasing the well width below 57  $\text{\AA}$  (S4) to 50  $\text{\AA}$  (S3) results in a wider spectral response with similar peak absorption wavelength. This complies with the expectation that the transition type is pushed towards bound-to-continuum as the excited state is further elevated. When S4 and S5 which have the same

well width (50Å) are compared, increasing indium mole fraction in the well from 0.48 to 0.51 results in shift in the peak responsivity / cut-off wavelengths from 9.04/9.60 μm to 8.80/9.25 μm as well as decreasing of the  $\Delta\lambda/\lambda_p$  from 13.8% to 10.8%.

In the next section, the characteristics of the large format (640x512) sensor fabricated with sample S2 (**Table 2.1**) will be presented at both pixel and FPA levels in comparison with an AlGaAs/GaAs QWIP sensor with similar spectral responsivity.

## 2.9 Detailed Characterization at Pixel and FPA Level

The pixel level characterization results presented in this section were measured on the support pixels of the FPA fabricated with S2 (**Table 2.1**) in comparison with those of an AlGaAs/GaAs QWIP FPA with the same pitch. InP/InGaAs epilayer structure, S2, consists of forty 60 Å thick In<sub>0.48</sub>Ga<sub>0.52</sub>As QWs ( $n_s=2.4 \times 10^{11} \text{ cm}^{-2}$ ) between 400 Å thick InP barriers. The AlGaAs/GaAs FPA pixels used in the comparison were fabricated with 36 GaAs (45 Å) quantum wells ( $n_s=1.8 \times 10^{11} \text{ cm}^{-2}$ ) between 500 Å thick Al<sub>0.27</sub>Ga<sub>0.73</sub>As barriers. Both detectors were fabricated using cross type optical grating structure and 25 μm pitch. While attention has been paid to have the two QWIPs displaying similar spectral characteristics (with the same diffraction grating structure) for a fair comparison, no definite quantitative conclusion is propounded on the ultimate relative performances of AlGaAs/GaAs and InP/InGaAs QWIP FPAs due to different processing techniques leading to non-identical mesa profiles. These unavoidable differences may lead to different light coupling efficiencies in QWIPs based on different material systems. The employed light coupling scheme and epilayer structures are not perfectly optimized for a specific target application. Further work may be conducted toward the optimization of the BLIP detectivity or BLIP temperature depending on the requirements of the specific applications. However, the general conclusions of this work should be still valid and guiding for application specific design work.

After defining the detector mesas and optical grating by reactive ion etching using an inductively coupled plasma system and the formation of ohmic contacts, reflectors, passivation, under-bump metallization and In bumps, the InP/In<sub>0.48</sub>Ga<sub>0.52</sub>As QWIP FPA

was hybridized to FLIR Systems ISC9803 ROIC using Suss MicroTec FC150 flip-chip aligner/bonder. After the hybridization and underfilling, the InP substrate was thinned to  $\sim 10 \mu\text{m}$ .

Pixel level electrical and optical characterization was conducted on parallel connected test detectors (identical to FPA pixels with dimensions of  $\sim 21 \times 21 \mu\text{m}^2$ ) flip chip bonded to a fan out substrate for characterization under backside illumination. The test pixels/fanout-substrate hybrid was not filled with underfill epoxy to eliminate any secondary effects resulting from the absorption of the radiation by the epoxy. Test detectors were characterized using a blackbody source, a chopper, a low noise transimpedance preamplifier, a lock-in amplifier, an FTIR system and a dynamic signal analyzer.

As depicted in **Figure 2.14**, the normalized spectral responsivity of the InP/InGaAs and AlGaAs/GaAs QWIP test pixels exhibit similar characteristics.

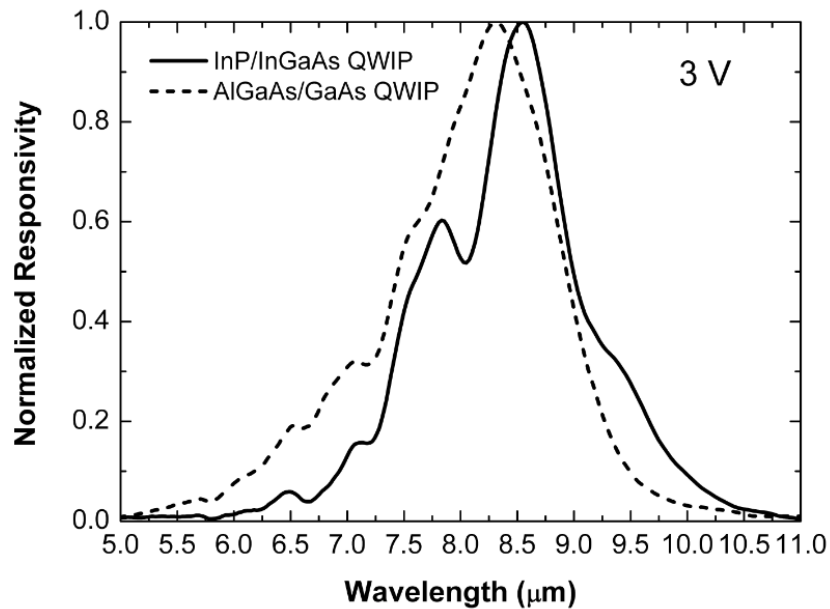


**Figure 2.14.** Normalized spectral responsivity of the InP/InGaAs and AlGaAs/GaAs QWIP test pixels [108].

**Figure 2.15** displays the I-V characteristics of the InP/InGaAs QWIP FPA pixels showing background limited performance with  $f/2$  optics for temperatures below 72 K up to a reverse bias voltage of  $\sim 2$  V. Dark current under positive bias (mesa top positive) is smaller than that under negative bias in agreement with the result reported by Gunapala et. al. [59] on MOMBE grown QWIPs. Positive bias response spectrum for this QWIP is narrower than that under negative bias again in agreement with Ref. [59]. These observations can be explained by the lower barrier formation during the MBE growth of InGaAs on InP when compared with that for InP on InGaAs in contrast to that reported by Andersson et. al. on MOVPE grown QWIPs with arsenic incorporation into the InP layer grown on InGaAs [109]. It should be noted that the asymmetry in the I-V characteristics is not likely to originate from the diffusion of the dopants into the barrier during growth, if the dopant diffusion is faster in the growth direction [110]. In this case, the barrier lowering and E-field enhancement is expected to occur at the InP on InGaAs interface leading to larger current under positive bias. Furthermore, due to the lower growth temperature of InP/InGaAs materials compared to AlGaAs/GaAs couple, dopant diffusion is expected to be less significant. Positive bias dark and photocurrents of the AlGaAs/GaAs QWIP FPA pixels were found to be larger than those under reverse bias.

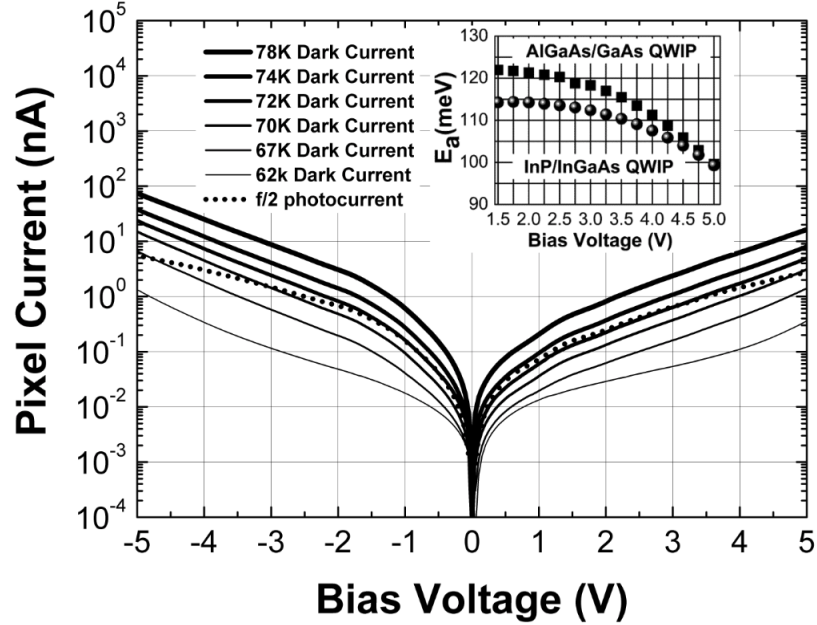


**Figure 2.15.** I-V characteristics of fabricated InP/InGaAs QWIP test pixels and bias dependency of activation energy (inset) [108].

The dark current activation energies ( $E_a = E_b - E_1 - E_f$ ) for the InP/InGaAs and AlGaAs/GaAs QWIPs are shown in the inset of **Figure 2.15**.

Under the conditions where the tunneling currents can be ignored, the dark current of QWIP depends on temperature as follows [108]

$$\frac{I_D}{T} \propto e^{-\frac{(E_b - E_1 - E_f)}{kT}} = e^{-\frac{E_a}{kT}} \quad (2.5)$$

where  $E_b$  is the barrier height,  $E_1$  is the bound ground state energy, and  $E_F$  is the Fermi level measured with respect to  $E_1$ .

The Fermi energies measured with respect to ground state ( $E_1$ ) are estimated using Equation 2.5 to be  $\sim 14$  and  $\sim 3$  meV for the InP/InGaAs and AlGaAs/GaAs QWIPs, respectively. The optical activation energies are nearly equal for the two QWIPs as indicated by **Figure 2.14**. Under this condition, the difference between the dark current activation energies should be nearly equal to the difference between the Fermi energies which is the case under low bias voltages as reflected by the activation energies of 122

and 114 meV for AlGaAs/GaAs and InP/InGaAs QWIPs, respectively. At the same time, the optical cut off energy ( $E_b - E_1 \cong 138$  meV) is in reasonable agreement with  $E_a + E_f$ . The activation energies under large bias voltages shown in the inset of **Figure 2.15** are for illustrative purposes since the temperature dependence of dark current can no longer be described by Equation 2.5 when considerable tunneling is present. The activation energy is expected to decrease with increasing bias due to barrier lowering effects [111]. Nearly bias independent activation energy up to  $\sim 2.5$  V in both QWIPs suggest that the tunneling currents are insignificant in this range. This has been verified by the perfectly straight lines obtained when  $I_{dark}/T$  was plotted in log scale versus  $1000/T$ . This observation serves as an indication of high quality (low impurity/defect density) barriers in both devices. Indeed, the detectors provide desirable characteristics in the bias voltage range applicable by a typical ROIC.

**Figure 2.16** compares the I-V characteristics of InP/InGaAs and AlGaAs/GaAs QWIPs. Photo- to dark current ratios of the devices at 72 K are shown in the inset of **Figure 2.16**. Both dark and photocurrents of InP/InGaAs QWIP FPA pixels are larger than those of AlGaAs/GaAs QWIPs under moderate and large bias voltages. The InP/InGaAs QWIP is superior to the AlGaAs/GaAs QWIP at the operation temperatures typically used for QWIPs and provides up to a factor of 2 higher photocurrent to dark current ratio at 72 K.

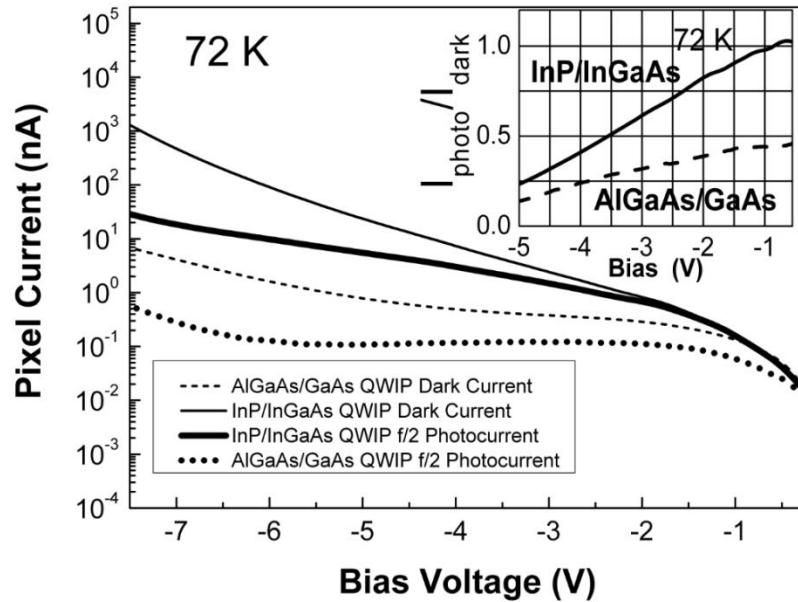


**Figure 2.16.** Dark and photocurrents of AlGaAs/GaAs and InP/InGaAs QWIP FPA pixels at 72 K [108].

The peak responsivity of the InP/InGaAs QWIP test pixels versus reverse bias voltage (mesa top negative) is shown in **Figure 2.17**. The pixels exhibit very high conversion efficiency and peak responsivity of 22 % and  $\sim 1.5$  A/W under 3.5 V bias which is applicable by commercial ROICs. Considering the fact that the AlGaAs/GaAs QWIP FPA pixels generally yield conversion efficiencies around 5% or lower, this result shows a tremendous improvement introduced by the intrinsic properties of the InP/InGaAs material system.

The peak detectivity of the InP/InGaAs QWIP test pixels measured with  $f/2$  aperture is presented in **Figure 2.18**. The pixels display excellent performance with a moderate bias detectivity of  $\sim 5 \times 10^{10}$   $\text{cmHz}^{1/2}/\text{W}$  at a temperature as high as 78 K. It should be noted that the conversion efficiency of the device can be varied with bias in a wide range while keeping the detectivity at reasonably large values in the bias region applicable by standard ROICs. This property of InP/InGaAs QWIPs offers flexibility to adapt the sensor to different operation conditions as discussed in Section 2.1.

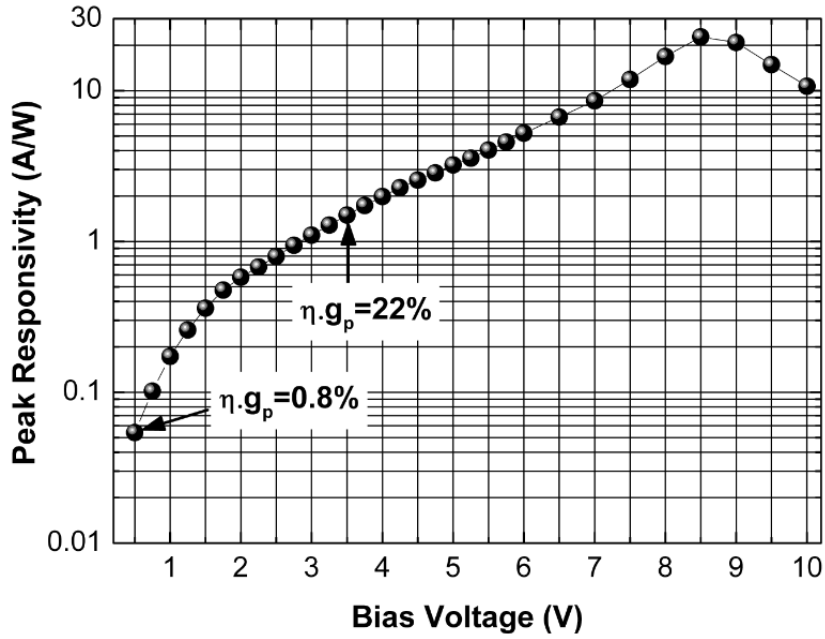


**Figure 2.17.** Peak responsivity of the InP/InGaAs QWIP FPA pixels versus reverse bias voltage (mesa top negative) [108].

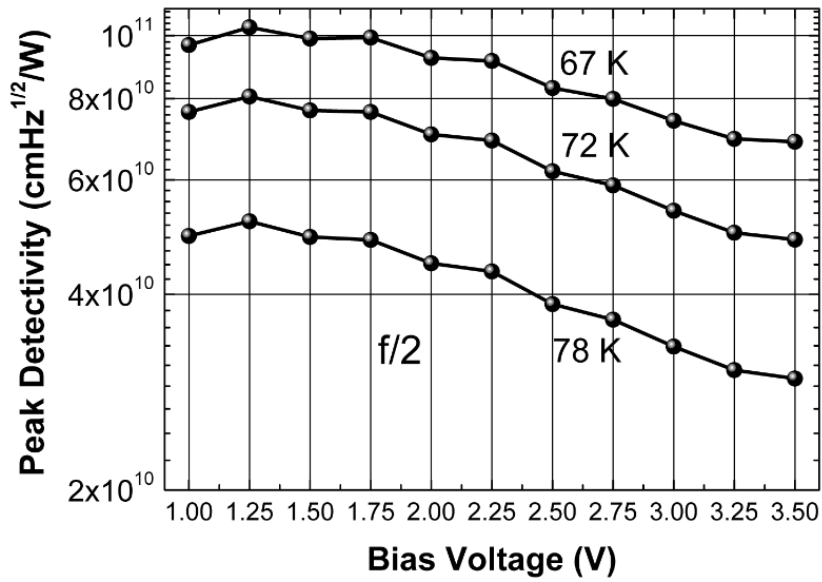


**Figure 2.18.** The peak detectivity of InP/InGaAs QWIP FPA pixels with  $f/2$  aperture [108].

The noise and photoconductive gains of the InP/InGaAs QWIP test pixels are presented in **Figure 2.19**. The noise gain was extracted from noise measurements at 78 K using the standard G-R noise current expression (Equation 1.21). Noise measurements were performed at 333 Hz with a low noise preamplifier and a lock in amplifier and were verified with Agilent 35670A dynamic signal analyzer.

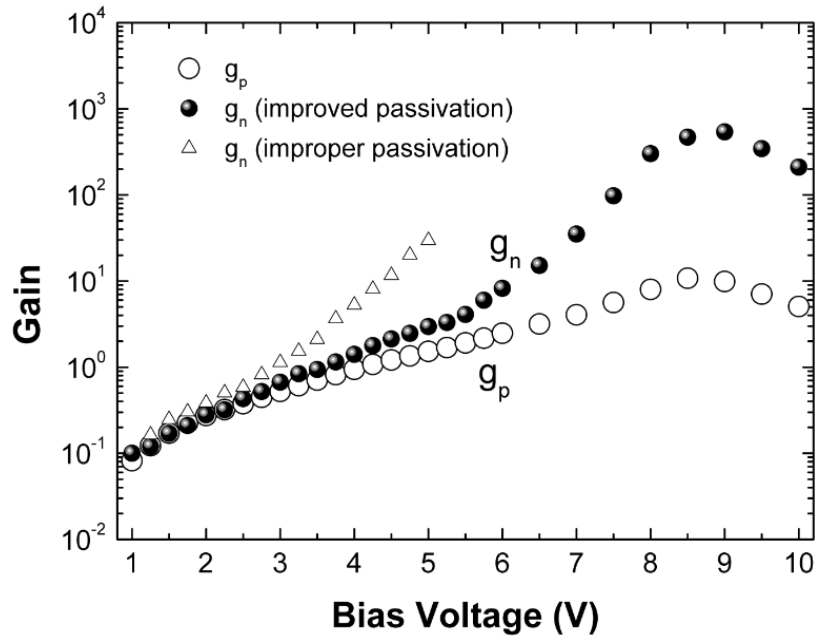


**Figure 2.19.** Noise and photoconductive gains of InP/InGaAs QWIP pixels [108].

Under moderately large bias (where escape probability is close to unity), the noise gain is expected to be equal to the photoconductive gain. Therefore, the quantum efficiency can be extracted by setting  $g_p = g_n$  and using the measured conversion efficiency ( $\eta \cdot g_p$ ) through the responsivity measurement. The quantum efficiency determined with this method is 31% which is extraordinarily high for a grating coupled QWIP FPA pixel. The photoconductive gain is nearly equal to the noise gain up to a bias voltage of  $\sim 3V$  if the quantum efficiency is held constant at 31%. This observation shows that  $\eta$  does not considerably change with bias in this range. The peak quantum efficiency of the AlGaAs/GaAs QWIP FPA pixels was measured to be around 4%. While this value can

be considered as typical for AlGaAs/GaAs QWIPs, it is significantly lower than that of InP/InGaAs QWIP FPA pixels. If the quantum efficiency is assumed to be inversely proportional to the electron effective mass in the quantum well, the effective mass and well doping density differences predict only ~2 times larger  $\eta$  in the InP/InGaAs QWIP. This larger than predicted difference in quantum efficiencies cannot entirely be attributed to the different light coupling efficiencies of non-identical pixel geometry which is an unavoidable result of different fabrication processes. A clearer quantitative explanation for this difference calls for detailed and complicated theoretical analysis.

**Figure 2.19** shows the noise gain characteristics of InP/InGaAs QWIP FPA pixels fabricated with two different passivation techniques in order to demonstrate the degrading effects of improper passivation process. Improper passivation refers to passivation with  $\text{Si}_3\text{N}_4$  which is a commonly used material for AlGaAs/GaAs QWIPs. As seen in **Figure 2.19**, noise gain deviates from the photoconductive gain at considerably low bias voltages with this type of passivation. The results presented in **Figure 2.19** are interesting in the sense that excess noise introduced by improper passivation displays a characteristic similar to that of avalanche multiplication through impact ionization which is not expected to be suppressed by surface passivation. Improper passivation leading to larger detector noise even under low bias voltages also results in underestimation of the quantum efficiency by overestimating the device gain. The results strongly suggest that the passivation of the InP/InGaAs QWIPs must be carefully optimized in order to obtain the true performance out of them.

**Figure 2.20** shows the drift distances for InP/InGaAs and AlGaAs/GaAs QWIP test pixels extracted from the measurements. In case avalanche multiplication occurs in the device, the extracted drift distance for the InP/InGaAs QWIP will be meaningful up to an E-field of ~30 kV/cm ( $V_{\text{bias}} \sim 6$  V) below which, impact ionization does not set in. The experimental results are in reasonable agreement with the predictions of the EMC simulations which expect nearly an order of magnitude larger photoconductive gain in InP/InGaAs QWIPs under large bias. At the bias voltage (~ 2V) where the gains of the two devices are equal, the dark current of the InP/InGaAs QWIP is larger than that of the AlGaAs/GaAs QWIP by a factor of ~3 at 72 K as reflected by the characteristics in

**Figure 2.16** which is in agreement with the Fermi energy and effective mass differences. The well doping of InP/InGaAs QWIP should be decreased roughly by a factor of 2 to have the same dark current with the AlGaAs/GaAs QWIP. In this case, since the quantum efficiency is proportional to the well doping density, InP/InGaAs QWIP will still provide higher photocurrent to dark current ratio due to the large difference between the measured quantum efficiencies under the present condition.

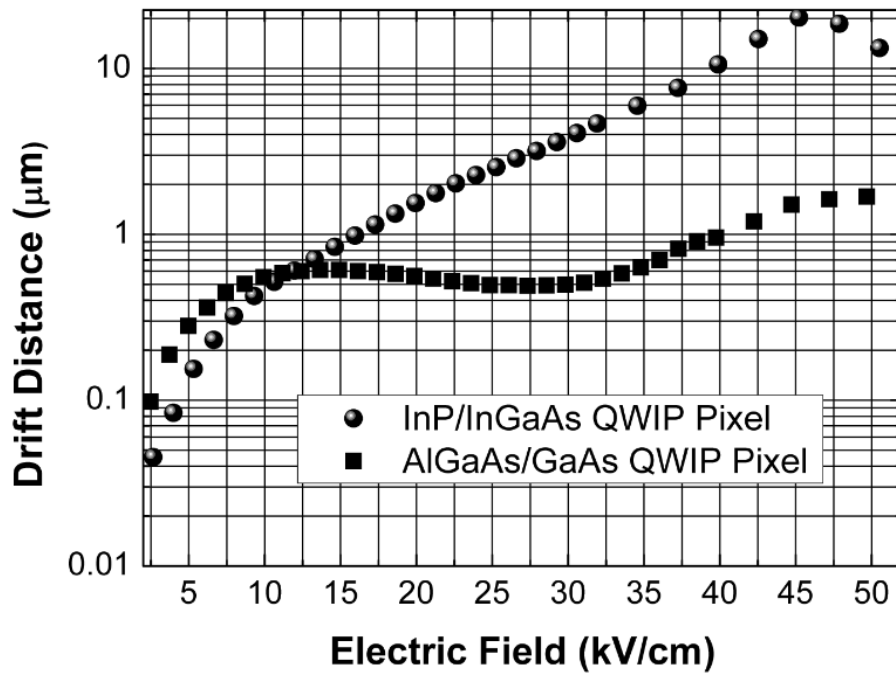


**Figure 2.20.** Drift distances of InP/InGaAs and AlGaAs/GaAs QWIPs extracted from measurements [108].

The existence of the case where the detector noise is suppressed with proper surface passivation invalidates the possibility of avalanche multiplication under moderate to large (3-5 V) bias voltages. Therefore the excess noise in the detector with improper passivation is likely to originate from surface nonidealities indicating that InP/InGaAs QWIPs may be prone to surface conditions. However, it is already demonstrated that excess noise can successfully be suppressed in the bias range of interest by alternative

passivation techniques, which can further be improved by optimizations. Therefore, we do not consider this property of the InP/InGAs material system as a disadvantage leading to degraded performance when compared with AlGaAs/GaAs QWIPs. The dark current-voltage characteristics of the pixels fabricated with improper and improved passivation techniques are shown in **Figure 2.21**. In both cases, the pixels exhibit almost identical dark current characteristics showing that the excess noise generating mechanism(s) does not create excess current (DC) in the device. Normalized noise spectral density of the devices with improper passivation is shown in the inset of **Figure 2.21** displaying 1/f like noise under large bias voltages at which the noise gain deviates from the photoconductive gain. This observation is similar to the trap assisted tunneling component of a low bandgap semiconductor (e.g. HgCdTe) photodiode dark current, which, being invisible through the dark current analysis, may introduce considerable 1/f noise to the device [112]. Therefore, the efficiency assessment of a passivation process in these devices should include the noise characterization as well as dark current measurements.

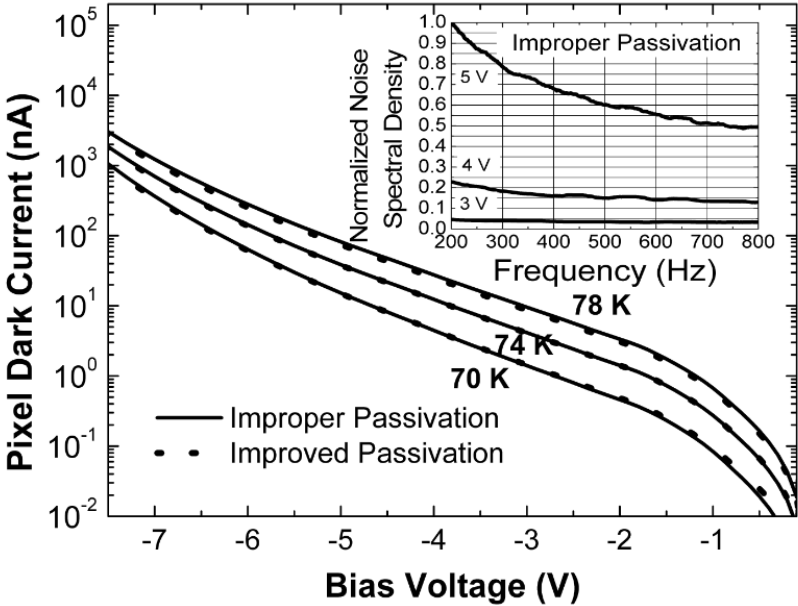


**Figure 2.21.** I-V characteristics of the pixels fabricated with improper and improved passivation techniques [108].

Referring back to **Figure 2.19**, while it is suspected that the excess noise causing the deviation of noise gain from photoconductive gain in the 3.5 – 6 V bias range is related to imperfections of the “proper” passivation, there is an apparent increase in the slope of the noise gain above 6 V bias. This observation suggest the initiation of an extra noise mechanism beyond this point. The nature of this process needs further investigation for clarification.

Gendron et al. [113] concluded that impact ionization process in QWIPs occurs only in the first two periods of the structure under typical operating conditions, and avalanche multiplication does not exist in the device.

Schneider et al. [97] presented a theoretical treatment of excess noise in QWIPs originating from avalanche multiplication. In case of small capture probability, the photoconductive gain and the noise gain extracted from the standard G-R noise expression are expressed as  $g_p = g_{net}M$  and  $g_n = g_{net}M^2$  in terms of the gain of the device in the absence of multiplication ( $g_{net}$ ).

Rehm et al. [114] investigated the characteristics of a 20-period GaAs/In<sub>0.3</sub>Ga<sub>0.7</sub>As QWIP. They attributed the difference between the photoconductive and noise gains under large E-field to avalanche multiplication resulting from impact ionization. Following the predictions of the theory [97], they reported an M value of 3.6 at an E-field as high as ~37 kV/cm.

Aslan et al. [115] obtained results showing that M saturates in the range 1.5-2 at a bias voltage of ~3 V in a 20-well InP/InGaAs QWIP. The authors attributed the excess noise to avalanche multiplication while it was not clear why M saturated rather than increasing with bias. In the light of the results obtained in this work, the excess noise (at least in the bias region investigated by the authors) may not originate from impact ionization which explains why M saturates at a rather small value.

The InP/InGaAs QWIP in this work yields a maximum M of ~55 at an E-field of ~48 kV/cm assuming that avalanche multiplication by impact ionization occurs under large bias. Beyond this biasing point M decreases with increasing E-field which is accompanied with a decrease in the responsivity (**Figure 2.17**). The saturation of

responsivity under large bias may occur due to the decrease in the ionization coefficient at high electron energies with the decrease in the wave function overlap between the free and bound electrons as explained by Levine [39]. However, avalanche multiplication may not absolutely be necessary to reach the experimentally observed large responsivity levels based on the predictions of EMC simulations. In the absence of avalanche multiplication, the responsivity characteristic under large bias can be explained by intervalley scattering of electrons which decreases the drift distance. While it is worth investigating the large bias characteristics through further study, impact ionization in InP/InGaAs QWIPs does not seem to have considerable effect on the FPA performance since the maximum bias voltage applicable by a typical ROIC ( $< 5$  V) is not large enough to create the required E-field strength for avalanche multiplication in a typical QWIP.

The operability of the FPA was larger than 99.5% with responsivity and NETD nonuniformities (without calibration and  $\cos^4$  correction) of  $\sim 6\%$  and  $\sim 15\%$  which are comparable to those of the best AlGaAs/GaAs QWIPs. **Figure 2.22** shows the normalized NETD histogram of the FPA at 68 K confirming the good uniformity throughout the FPA in terms of both responsivity and noise characteristics. **Figure 2.23** shows the NETD of the InP/InGaAs QWIP FPA/ROIC hybrid determined using the results of the measurements on the test detectors and ROIC noise ( $550e^-$ ). Since the test detectors are identical to the FPA pixels in all aspects, this technique allows determination of the FPA sensitivity without being affected by the additional noise occurring during the measurement of the NETD with a camera. The integration times shown at each bias voltage correspond to half-filled ROIC capacitors ( $1.1 \times 10^7 e^-$  capacity). The NETD is below 50 mK with  $f/2$  optics at a temperature as high as 78 K, and the performance of the FPA with sub-millisecond integration times is exceptional for QWIPs. These results achieved with this FPA, which is open to optimization in many aspects, are among the best results reported for LWIR QWIP FPAs.

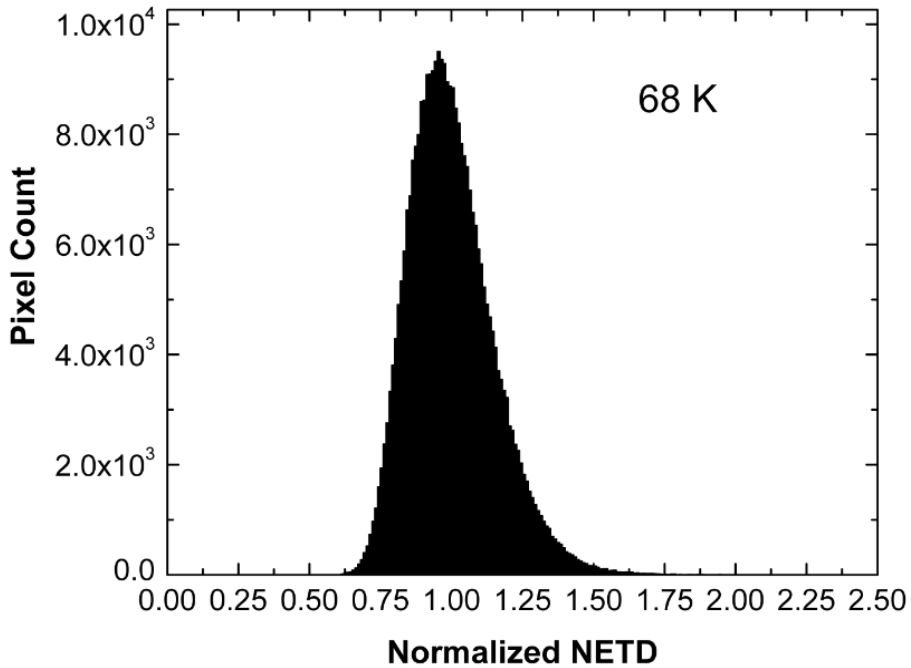


**Figure 2.22.** Normalized NETD histogram of the InP/InGaAs QWIP FPA at 68 K and  $V_{\text{bias}} = \sim 2.6$  V [108].

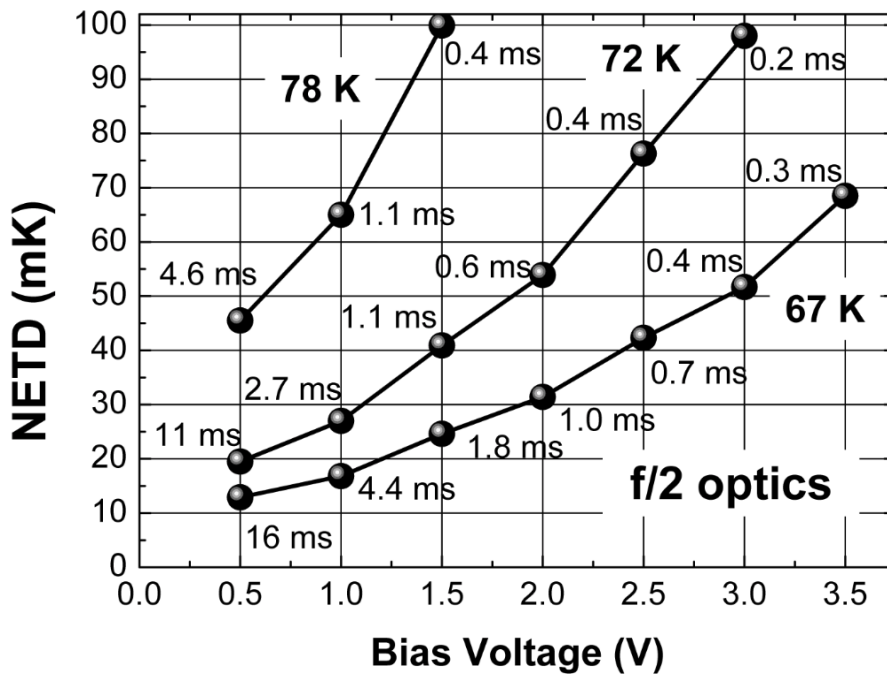


**Figure 2.23.** NETD of the InP/InGaAs QWIP FPA with half-filled ROIC capacitors and 300 K background at different operation temperatures [108].

**Figure 2.24** presents the NETD of the FPA/ROIC hybrid versus integration time with large f-number optics ( $f/2.7$ ) and short integration times under full BLIP condition. The NETD is shown with two different pixel bias voltages: 1.25 V for operating the sensor with optimum pixel detectivity and 3.5 V for high conversion gain required by short integration times. The NETD of the pixels with 1.25 V bias and 5 ms integration time is impressively low (15 mK) even with a small aperture ( $f/2.7$ ). It should be noted that the NETD increases to 81 mK when the integration time is decreased to 500  $\mu\text{s}$  if the FPA is kept under the same bias voltage. However, the FPA provides considerably better NETD (57 mK) with the same integration time (500  $\mu\text{s}$ ) if the bias is switched to 3.5 V. This observation demonstrates the importance of a large conversion gain under strict operation conditions.

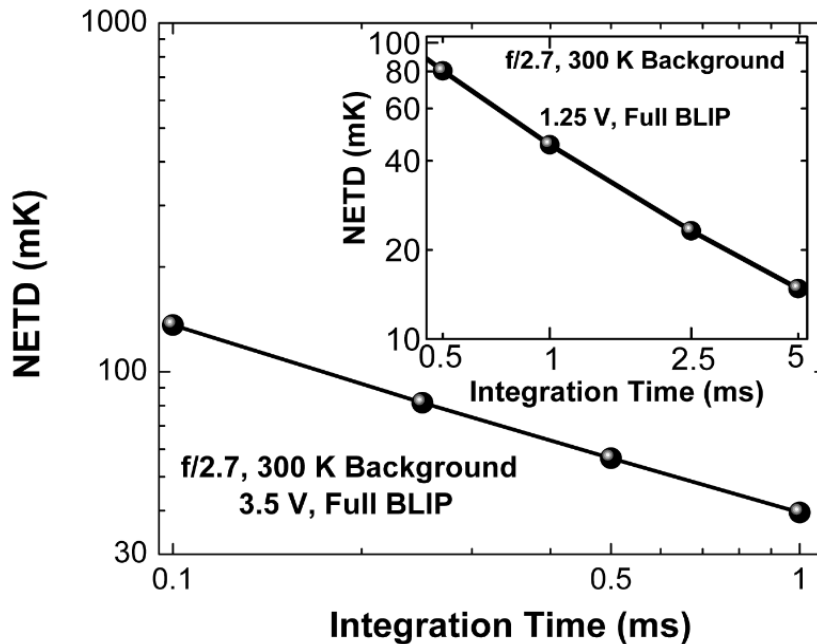


**Figure 2.24.** Background limited NETD performance of the InP/InGaAs QWIP at low integration times

Snapshot thermal images recorded with the FPA using  $f/2$  lens (100 mm) are shown in **Figure 2.25** under unusual conditions for LWIR QWIPs. The first image is recorded with

the FPA at  $\sim 80$  K under low bias, while the second image is recorded with a very short integration time of  $300 \mu\text{s}$  when the FPA is at  $\sim 65$  K.



**Figure 2.25.** Thermal images recorded with the InP/InGaAs QWIP FPA (a) at  $\sim 80$  K, (b) at  $\sim 65$  K. The second thermal image is recorded with  $300 \mu\text{s}$  integration time [108].

InP/InGaAs QWIPs are promising as sensors compatible with the requirements of new generation thermal imagers and high speed imaging. The exceptional results reported in this thesis demonstrate the potential of this technology as well as serving as a guide for the optimization of the epilayer/device structure of these sensors. While the quantum efficiency achieved in this work is suitable for a wide range of thermal imaging

applications, further work is necessary to increase the QWIP absorption efficiency to higher levels and make this sensor a lower cost alternative to HgCdTe detectors for high end applications. The results of this work suggest that there is room for this advancement.

## CHAPTER 3

### PERFORMANCE ENHANCEMENTS IN InGaAs/InP QWIPS

Recalling that a photon detector converts electromagnetic signal into an electrical signal, it is fair to say that any photon detector is an electromagnetic device as much as it is a semiconductor device. In this chapter, InP/InGaAs QWIPs are investigated from electromagnetics perspective with an emphasis on performance enhancing methods and explanation of observed electromagnetic effects.

This chapter starts with the presentation of an experimental study on diffraction gratings. Discussions on the effects of substrate thickness, underfilling process and anti-reflection coating are given in the next sections, followed by electromagnetic simulations.

#### 3.1 Diffraction Grating

Diffraction grating is the common method to create the perpendicular electric field component required for high absorption in QWIPs. Theoretically, cross grating with grating period,  $d$ , equal to absorption wavelength ( $\lambda_c$ ) in the material (i.e.  $d = \lambda_c/n_r$ ), and the etch depth,  $h$ , equal to the quarter of the wavelength inside the material (i.e.  $h = \lambda_c/4n_r$ ) should give the maximum perpendicular field intensity. However this purely theoretical prediction does not take into account,

- finite volume and boundaries of the pixel,
- position of the QW stack and the presence of inactive contact layers,

- oblique incidence.

Experimental investigation of the grating performance is required due to the above effects rendering the theoretical predictions unreliable.

A short set of experiments is designed to investigate the spectral behavior and performance enhancement level of the cross grating. FPA pixel size test detectors employing cross grating periods changing from 2.5  $\mu\text{m}$  to 3.1  $\mu\text{m}$ , were fabricated using epilayer structure S4. The test detectors were flip-chip bonded to fanout substrate and characterized with backside illumination. The responsivity versus bias curves for different grating periods are shown in **Figure 3.1**. The parallel lines in the responsivity curves suggest that the enhancement in the responsivity is independent of applied bias. Such behavior in the responsivity is indicative for an enhancement mechanism which does not have an electronic nature.

The dependence of the responsivity on the grating period is given in **Figure 3.2**. There is roughly 3 times improvement for most of the grating periods compared to reference detectors with no grating. The enhancement is still -but weakly- increasing beyond the theoretically expected period (2.8-2.9  $\mu\text{m}$ ). This observation suggests that diffraction effect is not narrow band and there may be additional resonances which may be comparably dominant in the electric field distribution inside the pixel volume.

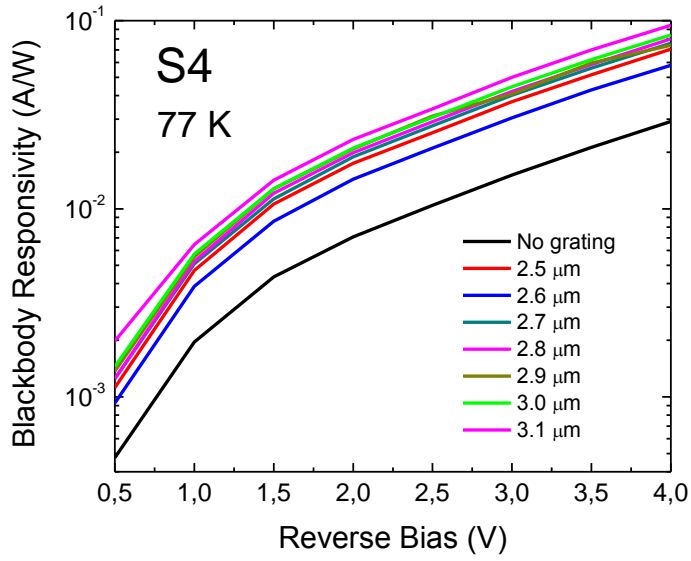


**Figure 3.1.** Responsivity of test detectors with different grating periods

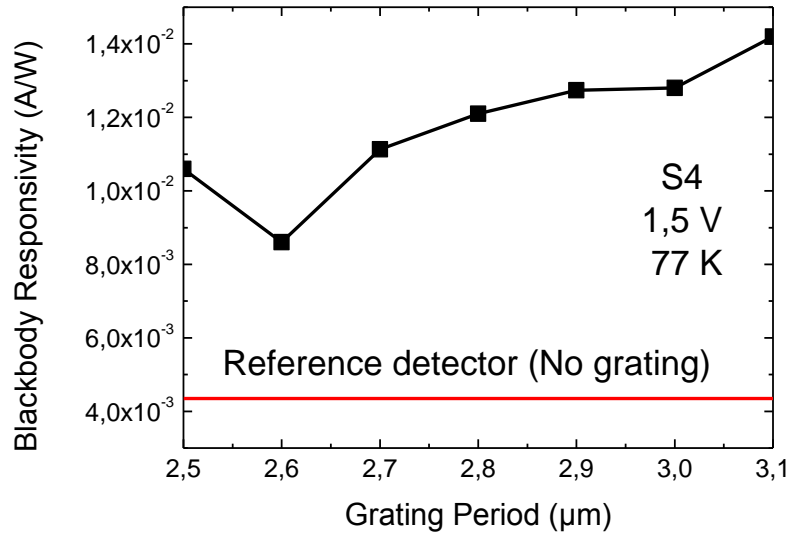


**Figure 3.2.** Dependence of responsivity enhancement on grating period

The responsivity spectra of the test detectors with different grating periods are shown in **Figure 3.3**. As it is suggested by the weak dependence of enhancement on the grating period, it is clearly visualized in **Figure 3.3** that the diffraction grating (utilized in this work) has wideband effect on the responsivity causing no change in the spectrum. Even the spectrum of the gratingless reference pixels follow the same spectrum which is a strong evidence that the diffraction grating has a relatively wide band response.

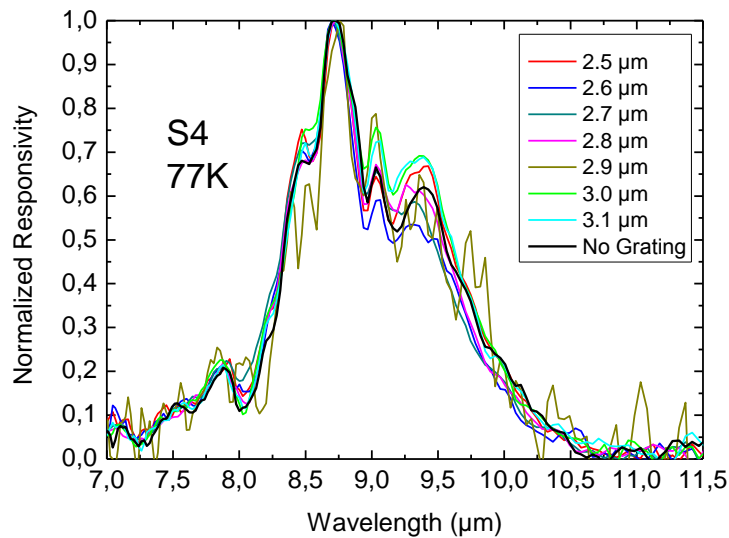


**Figure 3.3.** Responsivity spectra of test detectors with different grating periods

The amount of grating enhancement observed in this experiment is consistent with a similar work by A. DeRossi [48]. However in their report, there is no comment about tuning the grating to the intrinsic absorption spectrum of the quantum well.

### 3.2 Substrate Removal and Underfill

In the epitaxial film technologies, grown film is usually few microns thick (~5-10 $\mu\text{m}$ ) and constitutes only a small fraction of the material stock when the carrier substrate is taken into account (600-800 $\mu\text{m}$ ). The substrate material enables handling of the thin

epilayer structure and provides the mechanical support during processing. Almost all the macro-mechanical properties of the structure are therefore determined by the substrate material. In the hybrid device technology where chips of different materials are bonded together, mechanical incompatibilities causes several complications. In the case of infrared detector arrays where cryogenic operation is needed, the most important problem is the coefficient of thermal expansion (CTE) mismatch of the substrate material (InP, GaAs, CdZnTe) with silicon readout chip. When free silicon is cooled down to 77 K, it contracts about 450 ppm from its original dimensions ( $\Delta L/L = -450 \times 10^{-6}$ ), whereas common substrate materials contracts about 900-1000 ppm. If there is no other enforcing carrier substrate, the resulting difference in strain is shared between silicon and substrate material being inversely proportional to their young modulus and thickness. The most common solution is the partial or complete removal of the detector substrate material after hybridization and underfilling. The stress at the bonding interface is reduced after making the detector substrate thinner and easier to stretch. If the hybrid is cooled without substrate thinning, the substrate may crack in a couple of thermal cycles.

The partial removal of the substrate down to several  $\mu\text{m}$  thickness is routinely performed on underfill injected FPA hybrids. The FPA support pixels coupled to fanout substrates are usually characterized without substrate thinning due to their small size ( $\sim 2 \times 2 \text{ mm}^2$ ). In order to investigate the effect of substrate thickness on the detector performance, measurements were performed on support pixels with and without substrate removed. The complete substrate removal process mainly consists of a mechanical and a chemical step. At the end of these process steps, the detectors remain as a thin membrane suspended on the indium bumps. In **Figure 3.4**, support pixels coupled to fanout substrate are shown before and after substrate removal.

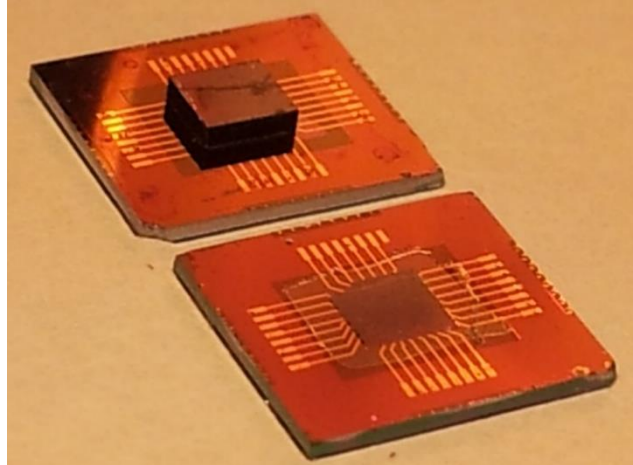


**Figure 3.4.** The FPA support pixels coupled to fanout substrate before and after substrate removal.

After the substrate removal, the responsivity spectrum of the InP/InGaAs QWIPs is strongly altered due to resonating modes in the pixel. These modes are created after the onset of internal reflections from epilayer-air interface. They can be regarded as interaction of epilayer-air interface with pixel boundaries. The responsivity spectrum measured on the support pixels with and without substrate, is shown in **Figure 3.5**. Both measurements are made on the FPA support pixels fabricated with the same epilayer structure (S5).

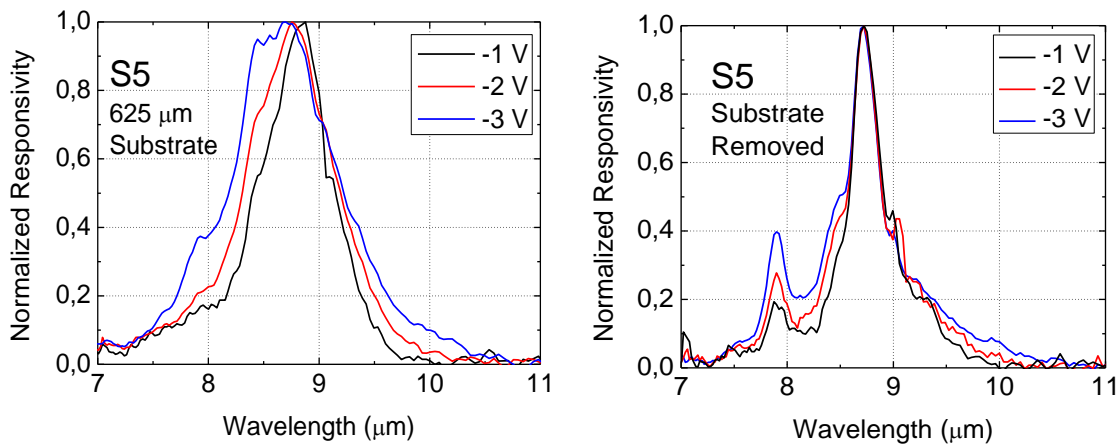


**Figure 3.5.** The responsivity spectrum of S5 with and without InP substrate

The observed resonances are very sharp when compared to the absorption spectrum by the electronic states. The evolution of the spectrum tails with increasing bias is the same in both cases. In this case, two major resonance lines (at 7.9  $\mu\text{m}$  and 8.7 $\mu\text{m}$ ) dominate the normalized absorption spectrum. The positions and widths of the resonance lines are functions of the pixel geometry and epilayer thickness being independent of electronic states. The effect of the substrate removal in the responsivity spectrum is different for different epilayer structures, and the case for S2 is shown in **Figure 3.6**. In this sample, no strong resonance line dominates the spectrum but several relatively smaller resonances can be seen.

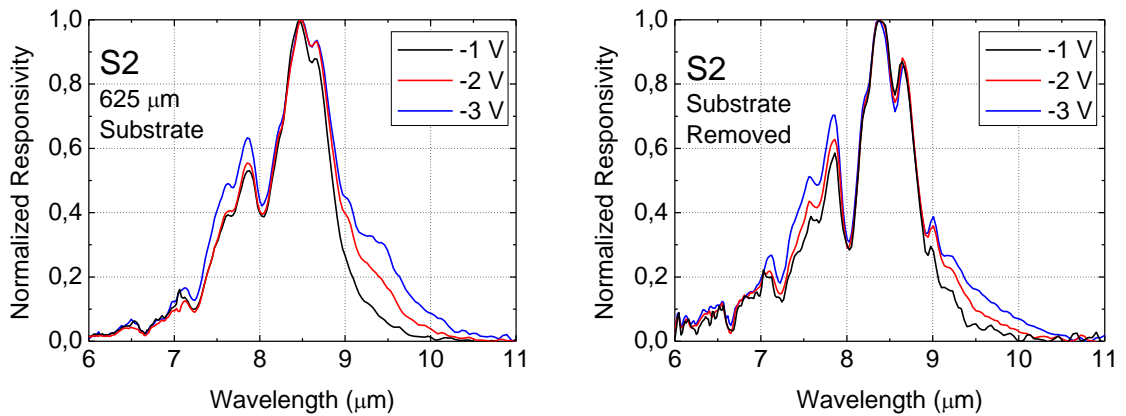


**Figure 3.6.** The responsivity spectrum of S2 with and without InP substrate

The effect of substrate removal in the blackbody responsivity is observed to be positive and around 10-20% in all cases. However, it was not possible to establish a trend using the results of experiments performed on various epilayer structures.

Underfill epoxy is another factor having an indirect effect on detector performance. When injected, epoxy fills the volume around the indium bumps and mesa sidewalls. Having a refractive index greater than air, the presence of underfill facilitates the escape of the radiation from the mesa sidewalls by increasing the critical angle for total internal

reflection [57]. It is observed that the absence of epoxy material may increase the responsivity up to 50% depending on sidewall profile and insulation material coated on sidewalls. The responsivity spectrum is mildly affected from the presence of underfill epoxy as shown in **Figure 3.7**. As the underfill alleviates reflections from the mesa sidewalls, sharp internal resonances fade and spectrum flattens out.

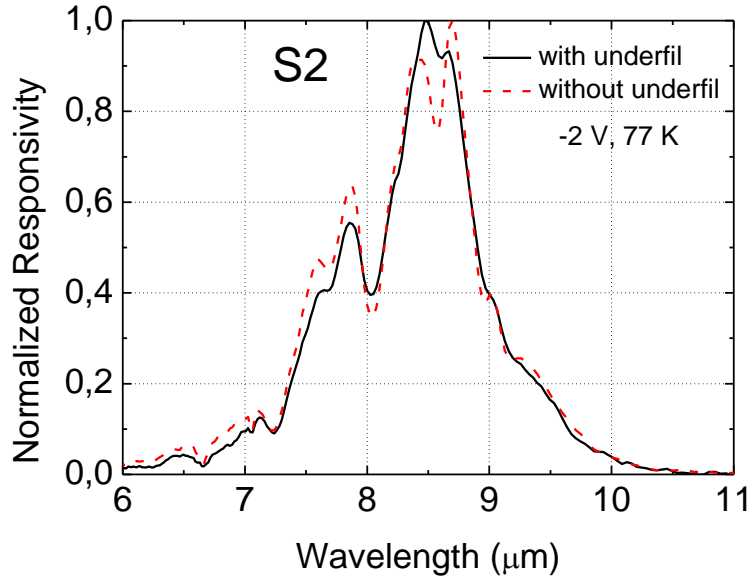


**Figure 3.7.** The responsivity spectrum of S2 with and without underfill.

### 3.3 Anti-Reflection Coatings

The substrate material InP has a refractive index around 3.1 at the infrared region. When the internal reflections are ignored, approximately 30 % of the normally incident radiation is directly reflected back from the substrate without reaching the quantum wells due to the high refractive index, This loss can be prevented by implementing an anti-reflection (AR) coating on the back side of the substrate. It is observed that the effect of the anti-reflection coating is a straight-forward increase in the responsivity of the detector if the substrate is thick enough to prevent secondary reflection to reach the air interface. However, when the substrate is thin or completely removed, the effect of an AR coating

is of interest in order to observe the electromagnetic resonances in the pixel structure. For this purpose, an AR coating is designed and implemented on QWIP structures.

AR coatings basically match impedances of the propagation media, preventing the reflection. The most basic AR coating is quarter wave transformer which consists of a  $\lambda/4$  thick layer with an refractive index of  $\sqrt{n_1 n_2}$ , where  $n_1$  and  $n_2$  are the refractive indices of the first and destination media. The material of the antireflective coating must be chemically stable and transparent at the operation wavelengths and must have a refractive index as close as possible to  $\sqrt{n_1 n_2}$ .

A simple AR coating employing a 950 nm ZnS film is designed using TFCalc software and verified on bare InP substrates. The ZnS deposition is performed at ASELSAN using RF sputtering. The FTIR transmission measurement of a single side coated InP substrate is shown in **Figure 3.8**.

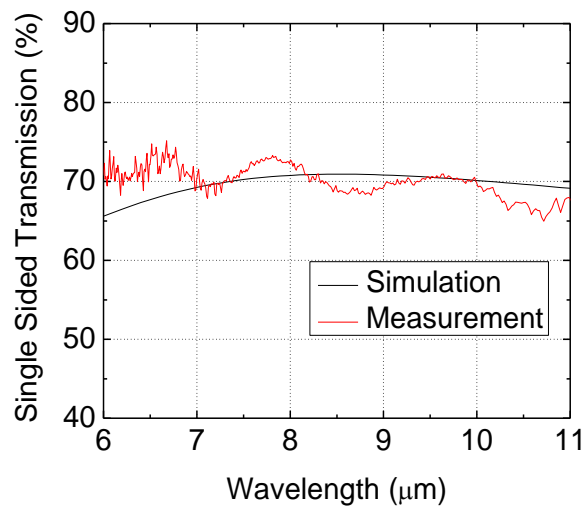


**Figure 3.8.** Transmission of InP substrate with single side AR coating

After one side of the InP substrate is AR coated, due to reflection from the other surface, ideally 70% transmission should be expected. As the measurement meets expectations,

and the AR coating is verified, the same coating is applied on the backside of FPA support pixels. In **Figure 3.9** the spectral responsivity of S5 FPA support pixels is compared before and after AR coating.

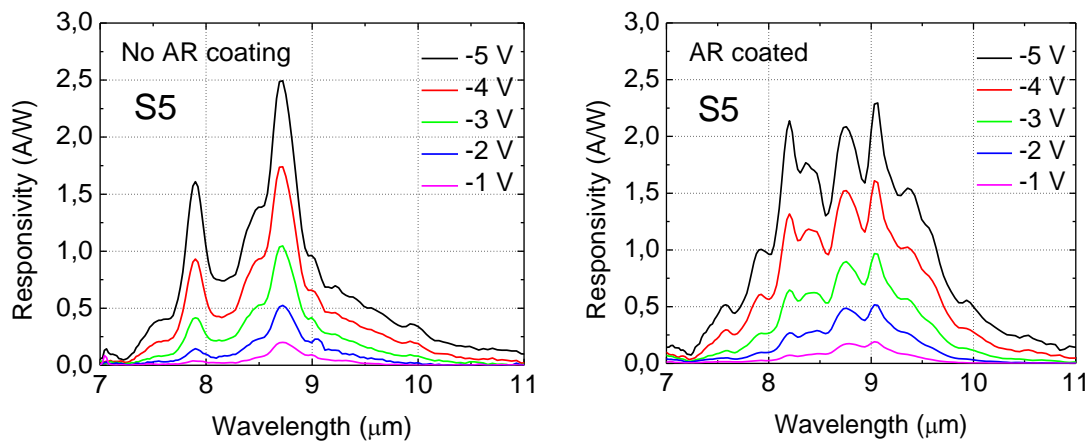


**Figure 3.9.** Spectral responsivity of S5 FPA support pixels before (left) and after (right) AR coating.

The spectral shape is significantly changed after AR coating which suggests a different electromagnetic field distribution inside the pixel volume. Instead of the two major resonance lines which appeared after substrate removal, many small resonances are visible and upper cut-off wavelengths is significantly extended. This observation suggests that more resonant modes have been excited after AR coating. Such a drastic change in the absorption spectrum signifies the importance of electromagnetic design of the pixel as much as the electronic design of the detector structure.

The 500°C blackbody responsivity of the AR coated detector is increased by  $\sim 20\%$  as shown in **Figure 3.10**. This increase is independent of the applied bias confirming that it is not related to any electronic process.

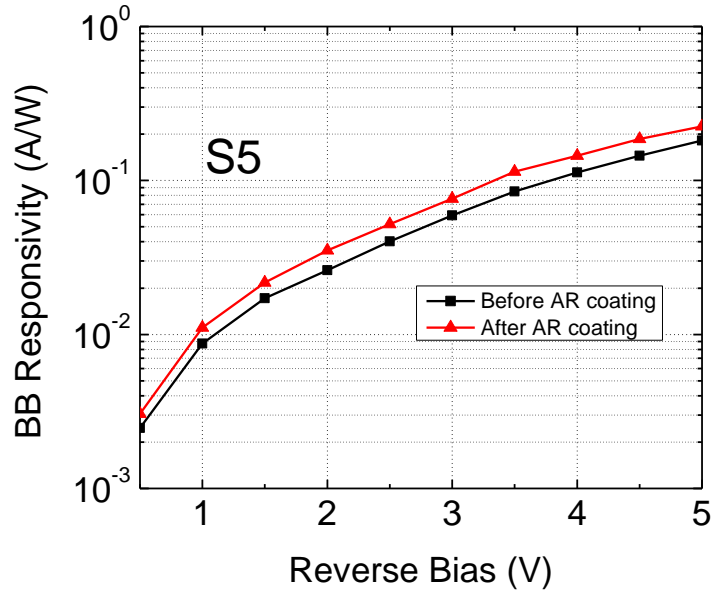


**Figure 3.10.** Black body responsivity of S5 FPA support pixel after AR coating

### 3.4 Electromagnetic Simulations

The relation of the QWIP's quantum efficiency to the electromagnetic field distribution in the detector volume is suggested by K.K. Choi [51] as

$$\eta = \frac{n\alpha}{AE_0^2} \int_V |E_z(\vec{r})|^2 d^3r \quad (3.1)$$

where  $A$  is the detector area,  $E_0$  is the incident field strength,  $\alpha$  is the absorption coefficient,  $n$  is the refractive index of the detector material, and  $E_z$  is the perpendicular field component inside the detector volume. According to the model, the quantum efficiency of the QWIP can be determined uniquely if the field distribution and absorption coefficient are known. In this thesis work, this model is used to explain the observed spectral behaviors.

The electromagnetic field distribution inside the detector pixel is solved using RF toolbox of COMSOL Multiphysics simulation software. In order to accurately model the geometry, actual pixel structure is investigated with scanning electron microscopy. In

**Figure 3.11** SEM pictures of actual pixel geometry and modelled geometry (bottom right) is shown.

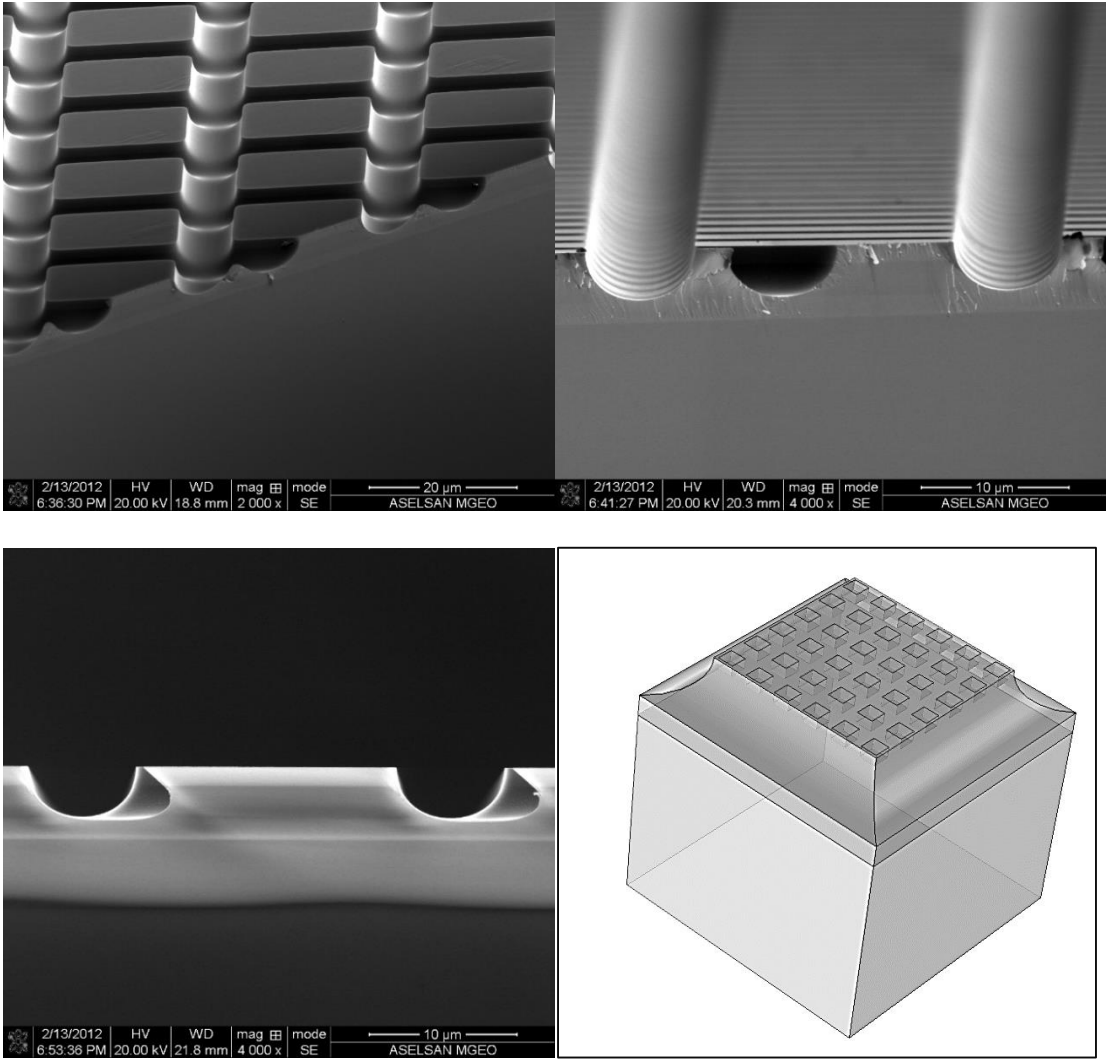


**Figure 3.11.** SEM pictures of the actual and modelled pixel geometry

The electromagnetic field inside the pixel was solved for the range of substrate thickness starting from 0.5 μm to 10 μm. The simulations were performed in frequency domain and repeated to cover a spectral the range of 6-12 μm. The periodic boundary conditions were used to simulate large arrays. Field extinction due to absorption was not taken into account. The following conclusions can be drawn from the results:

- The field distribution inside the pixel is sensitive to substrate thickness and sidewall profile. In **Figure 3.12**, center cross sections of field solutions are shown for 1  $\mu\text{m}$  and 5  $\mu\text{m}$  substrate thicknesses. At certain substrate thickness values, travelling modes appear decreasing the total field intensity in the active region and causing pixel-to-pixel cross-talk. However, these travelling modes contain significant  $|E_z|$  components which is crucial for QWIP absorption.

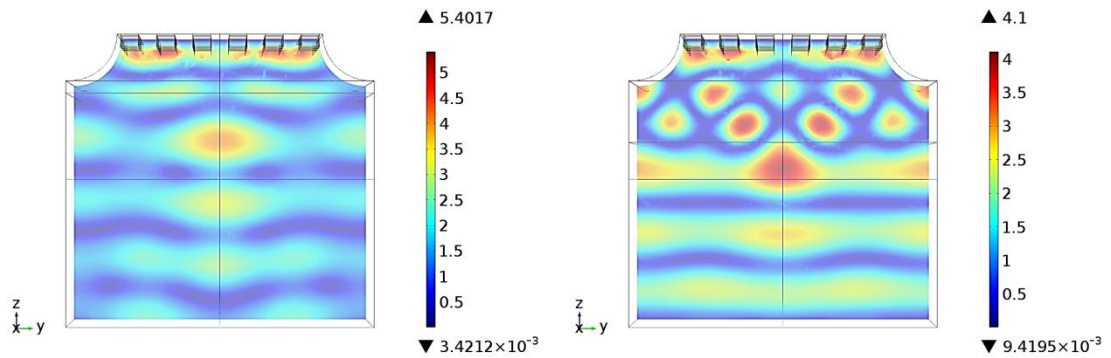


**Figure 3.12.** Field solutions for 1  $\mu\text{m}$  (left) and 5  $\mu\text{m}$  (right) substrate thickness

- Modes very quickly evolve with changing frequency, and very sharp resonance lines are present in the spectrum. Unless a structure is specifically designed for the purpose, it is not possible to find a broadband resonance with a comparable bandwidth to electronic absorption spectrum. In **Figure 3.13**, volume integration of  $|E_z|$  component is shown for changing substrate thicknesses between 0.5  $\mu\text{m}$  and 10  $\mu\text{m}$ . Although it is not easy to locate peak locations in this large amount of data, it is apparent that the peaks are very sharp both in wavelength and substrate thickness dimensions. **Figure 3.14** shows the cross section of **Figure 3.13** at 8.1  $\mu\text{m}$  and 9.1  $\mu\text{m}$  wavelengths, and is given to demonstrate that right at resonating points, the field strengths can be boosted to twice of their nominal values. This will certainly result in a significantly increased quantum efficiency and responsivity around a small

frequency range, as it is already observed in the spectral response of support pixels after the substrate removal as shown in **Figure 3.5**.

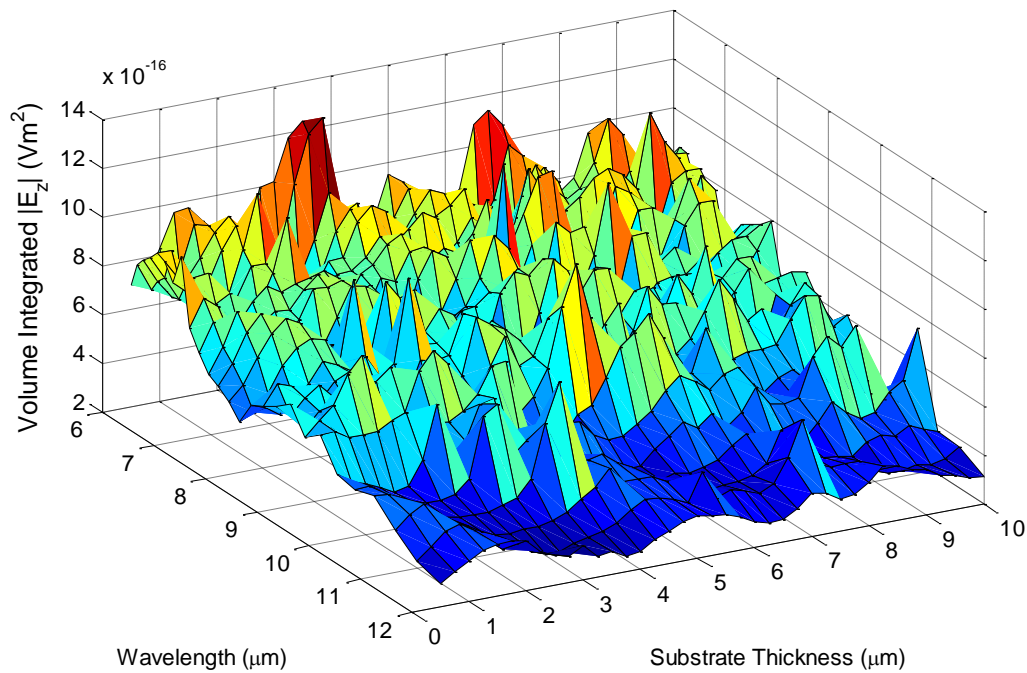


**Figure 3.13.** Parametric scan of substrate thickness in 6-12  $\mu\text{m}$  region

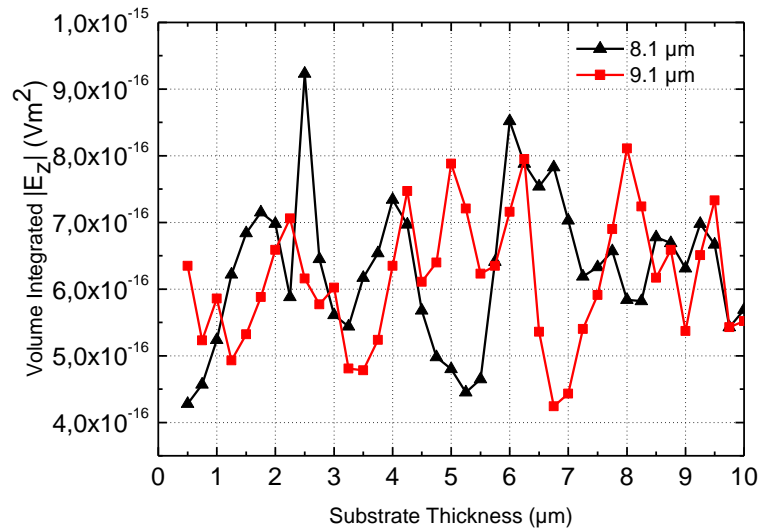


**Figure 3.14.** Volume integration of  $|E_z|$  for wavelengths 8.1  $\mu\text{m}$  and 9.1  $\mu\text{m}$

In this section, some of the factors effecting the performance of the QWIPs are treated from electromagnetic point of view. The experimental observations have been explained with the help of simulation tools and further experiments. The main conclusion of the aforementioned experiments and results is that there are strong electromagnetic effects which should be taken into account while designing better QWIP structures. The simulation models should be improved and used as a design tool. It is quite promising that the performance level of present QWIPs can be further improved with careful electromagnetic design.



## CHAPTER 4

### LWIR HgCdTe FOCAL PLANE ARRAYS

Being the leading IR detector material for high end applications, HgCdTe is a well understood material after many years of research. However, due to its strategic importance, growth and processing procedures are mostly left as proprietary information of manufacturers and developers. In this part of the thesis, our studies toward MBE growth of LWIR HgCdTe material and FPA implementation are described.

#### 4.1 MBE Growth of HgCdTe

MBE is the trending HgCdTe growth method being adopted by many manufacturers as it offers significant advantages including

- in-situ doping,
- multiple layer heterojunctions,
- alloy grading,
- sharp and controllable interfaces.

The MBE reactor for HgCdTe mainly consists of the components described in Section 2.5. The additional items and concepts specific to HgCdTe growth will be reviewed here in further depth.

### 4.1.1 Growth Dynamics

The MBE growth of HgCdTe is an extremely non-equilibrium process with very low tolerances. The growth rate and material composition is controlled tightly by material fluxes and substrate temperature. A very nice illustration by Bratt et. al. [116] describing the MBE process is shown in **Figure 4.1**.

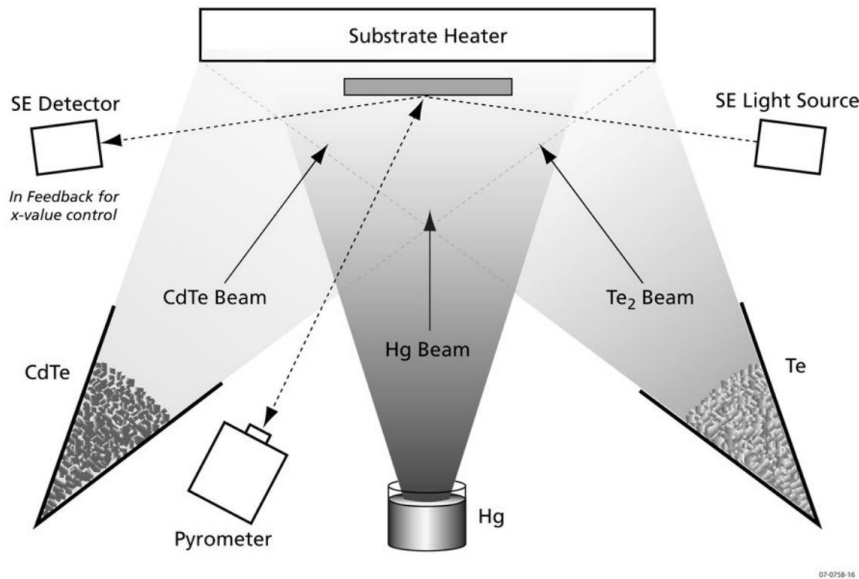


**Figure 4.1.** Simplified schematic of HgCdTe MBE process [116].

CdTe and Te<sub>2</sub> are supplied from solid sources in molecular form and mercury is evaporated from liquid phase. CdTe congruently evaporates from a Knudsen type effusion cell. Te is preferably used with a valved cracker type effusion cell (like As and P).

Since CdTe is used as the Cd source in the alloy, each Cd atom reaches the surface with an accompanying Te atom. The growth rate of CdTe in the alloy is then directly controlled by the flux of CdTe since it has unity sticking coefficient. However it is not the case for HgTe. Mercury has a very low sticking coefficient (1/300 at 180 °C) which is extremely dependent on temperature. At the optimum growth temperature, Hg is

supplied in excess and its incorporation to lattice is controlled by amount of free Te bonds available on the surface. Therefore ideally the HgTe growth rate is controlled by the flux of Te. The alloy composition is controlled by adjusting the CdTe/Te flux ratio at the optimum conditions. If the substrate temperature is slightly deviated from the optimum growth window in the downward direction, Hg starts incorporating interstitially due to increased rate of sticking and lack of Te supply, forming *twins*. On the other end, if the substrate temperature is higher than the optimum value, sticking rate drops severely creating Hg *voids* in the lattice. Other than the substrate temperature, the ratio of the supplied Hg and Te fluxes is equally important to keep the Hg-Te balance at the surface.

At the growth temperature of similar II-VI compounds without Hg (230-300 °C) and most III-V compounds (400-600 °C) there is significant re-evaporation of constituents creating a self-regulating surface stoichiometry. For example during the growth of III-As compounds, excess As atoms, which cannot make bonds to group-III elements, are re-evaporated from the surface unless the surface temperature is extremely low. In the HgCdTe case, if the temperature is slightly above the optimum growth window, Te tends to precipitate even in the presence of excess Hg flux. The growth temperature range of 175-195 °C provides enough surface mobility to the constituents, but is too low to support a self-regulating Te re-evaporation. From the practical point of view, the narrow optimum temperature window of  $185 \pm 5$  °C, as well as the relatively low growth temperature, make precise measurement and control difficult.

#### **4.1.2 MBE reactor for HgCdTe growth**

MBE growths in this thesis study were performed in a 3” Riber Compact 21 (C21) reactor assembled for HgCdTe growth. A picture of the system is given in **Figure 4.2**.



**Figure 4.2.** Riber C21 reactor used in HgCdTe growths

The most important difference of an HgCdTe MBE reactor is the accessories required for handling of Hg, which has a very high vapor pressure ( $\sim 2$  mTorr at 300 K). In each growth of  $\sim 10$   $\mu\text{m}$  epilayer of HgCdTe, approximately 300 g of Hg is released into the growth chamber. For this reason, significant amounts of Hg accumulated after several growths must be recovered from the growth chamber with a special procedure. In this recovery procedure, Hg is gradually immigrated to a dedicated compartment of the system where it is isolated from growth chamber. The whole reactor geometry is designed accounting for the liquid mercury presence in the chambers, moving with the gravity.

Due to the high vapor pressure of the Hg, liquid nitrogen supply to the cryopanel should not be interrupted while there is unrecovered Hg in the growth chamber. The HgCdTe growths were performed in campaigns consisting of 10-15 detector epilayer structure growths with continuous LN<sub>2</sub> supply.

The surfaces which are sensitive to Hg coating (viewports, ellipsometry ports, vacuum flanges with risky position) must be heated to avoid Hg depositions. Especially, coating of the ellipsometry ports makes it impossible to obtain healthy ellipsometry reading by decreasing the signal. In this work, special strain-free heatable quartz viewports heated to 250 °C were used for the M-2000 Spectral Ellipsometry (SE) from J. A. Woollam Co.

### **4.1.3 Growth Procedure**

More than 110 growths, including calibration layers and junctions, were done in this work for the establishment and amendment of the growth procedures. Main steps of the procedure followed are described in the sections given below.

#### **Substrate Preparation and Loading:**

In this work, mainly CdZnTe (211)B substrates were used. Since epi-ready CdZnTe substrates are not commercially available yet, each substrate has to go through a preparation step before it is loaded into the reactor. The substrate preparation and mounting is a critical step for achieving low defect density. While different substrate preparation procedures are available in the literature, most of them includes a solvent cleaning step and a Bromine-Methanol etching step with different etching times and concentrations [117]. The procedure adopted in this work consists of etching in Br:MeOH solution for several seconds, dipping in rinse solutions and N<sub>2</sub> blow drying.

The substrate is then mounted on a heated molybdenum block with a molten thin indium film. It is important to have uniformly thick indium film underneath the substrate to obtain a good temperature distribution across the substrate. The substrate is loaded into the reactor as quickly as possible after mounting.

**Flux Adjustment:**

Before the substrate is transferred to the growth chamber, effusion sources (CdTe, Te, In, As) are outgassed at temperatures slightly (10-20 °C) above the expected growth temperatures. The sources are then cooled to growth temperatures and flux values are adjusted to the desired values. The Hg flux is adjusted just before the growth starts.

**Substrate Degasing and Temperature Adjustment:**

After the flux adjustments, effusion sources are left at the growth temperatures with shutters closed, and the substrate is moved to the growth chamber for substrate thermal cleaning. The substrate is slowly heated with no incident flux. The surface condition of the substrate is closely monitored with RHEED pattern inspection during heating. At low surface temperatures (<140-150 °C), no crystalline structure is observed on the RHEED pattern due to excess Te atoms left on the surface by the Br:MeOH etch (**Figure 4.3**). The crystal structure appears on the streaky RHEED pattern with rods after evaporation of the excess Te atoms which corresponds to a surface temperature around 200 °C. The substrate is kept at ~300°C temperature for 30 minutes and cooled down to growth temperature under the adjusted Hg flux.

**Growth Start and RHEED Patterns:**

Growth is initiated with the opening of the shutters and the surface condition is closely followed with the evolution of the RHEED pattern. The RHEED pattern is the representation of the sample surface in the reciprocal space. Elongated streaks (lines in one dimension) on the RHEED pattern corresponds to two dimensional surface structures, i.e., flat and smooth crystal planes. Points and sharp bright spots (zero dimensional shapes) represent three dimensional structures, e.g. crater defects, hillocks and surface roughness. Common RHEED patterns and relevant growth conditions are described below using the illustrations by Sewell [118].

Immediately after loading, the substrate surface does not exhibit a crystalline behavior due to tellurium precipitates left after the Br:MeOH etch step. This atomic size Te

precipitates (thin metallic layer) is shown as random spots in the RHEED pattern as shown in **Figure 4.3**. These spots are visible at all azimuthal angles.

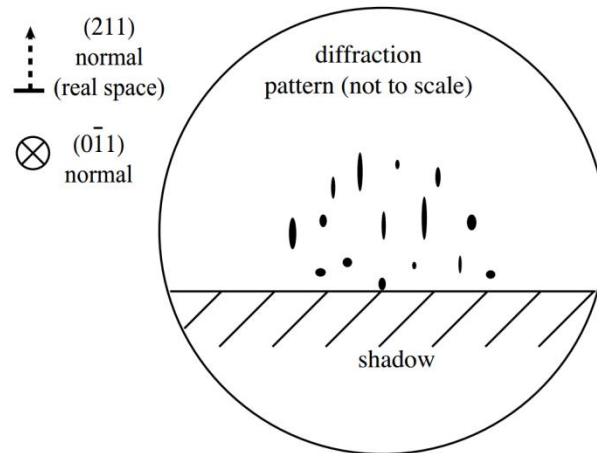


**Figure 4.3.** Initial spotty RHEED pattern due to excess tellurium [118]

As the substrate is heated, the excess tellurium is first mobilized then is evaporated from the surface, uncovering the crystalline structure of the substrate. The CdZnTe (211) surface containing steps gives a diffraction pattern as shown in **Figure 4.4**. Finite length rods appearing at certain azimuthal angles correspond to a surface containing terraces with limited flatness. Longer the rods, smoother is the surface. Surface flatness can be ameliorated by growing a thin CdTe layer at high temperatures.

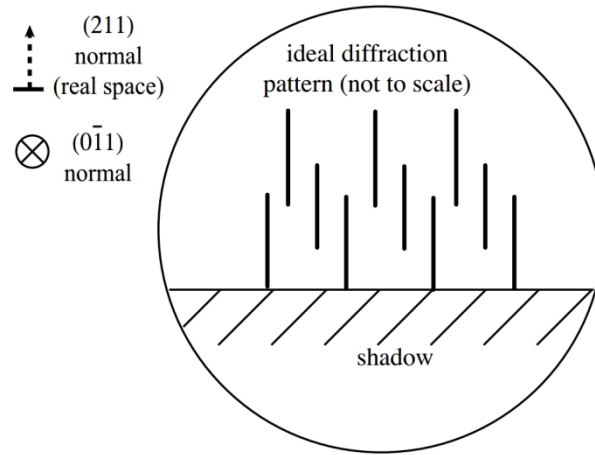


**Figure 4.4.** RHEED pattern from CdZnTe substrate after tellurium desorption [118]

There exists three MBE growth modes for growth on a planar surface. In Volmer –Weber mode, growth is irregular consisting of cavities and hillocks. In this mode, the surface is three dimensional with strong roughness. In Stranski–Krastinov mode, growth starts with formation of planes (2D) which later turn in to islands (3D) under the surface potentials. The ideal growth mode, Frank–van der Merwe, is the two dimensional growth mode where the growth front propagates layer by layer and each layer is completed before the next layer starts. The resulting two dimensional smooth surface leads to a long streaky pattern (**Figure 4.5**) which should be observed throughout the entire growth.

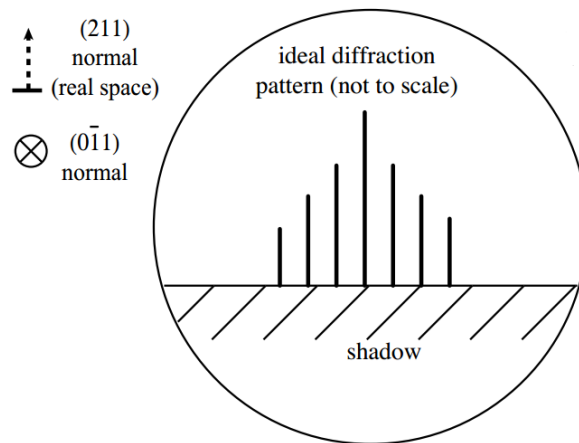


**Figure 4.5.** Ideal RHEED pattern during growth [118]

RHEED observation is very useful in HgCdTe growth since it allows instantaneous monitoring of the surface morphology while the film is still growing. The deviations from the optimum conditions immediately manifest themselves on the RHEED pattern in different ways. The most common situation is the disturbance of the Hg/Te balance by improper substrate temperature or inappropriate flux ratio. If there is too much Hg, adsorption induced by low substrate temperature and insufficient tellurium supply to accommodate incoming Hg flux, *crystal twinning* occurs due to interstitial adsorption of Hg. The twin boundaries appear as fine, extra streaks located at the tip of the elongated bright streaks as shown in **Figure 4.6**. In the early stages of twinning, twinned surface can be over grown and recovered, but growth conditions should be corrected as soon as possible by increasing the substrate temperature or decreasing Hg/Te flux ratio.

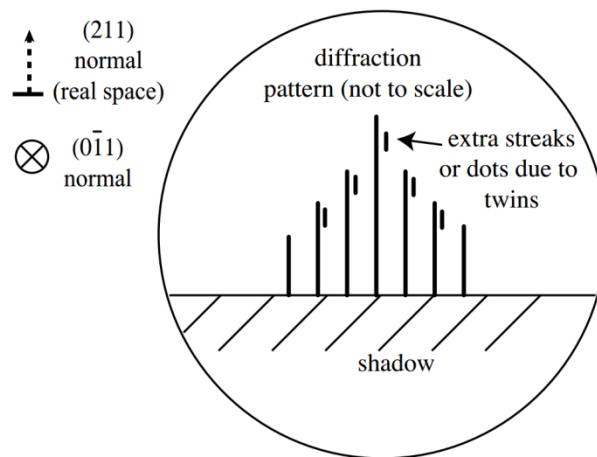


**Figure 4.6.** RHEED pattern from a twinned surface [118]

On the other side of the equilibrium, the surface may be short of Hg due to excessive re-evaporation induced by high substrate temperature or excessive Te arrival. In this case, RHEED pattern will be dim and will include step like rods caused by high Te precipitations in the layer (**Figure 4.7**).

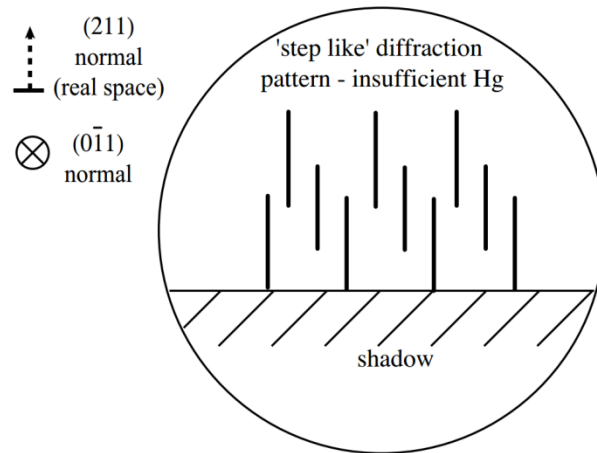


**Figure 4.7.** RHEED pattern induced by insufficient Hg [118]

This condition can be, as well, corrected by decreasing the substrate temperature or increasing the Hg flux. However prolonged growth in these non-optimal conditions leads to unrecoverable surface roughness or total loss of the crystal structure. In **Figure 4.8**, the RHEED pattern from a hopeless three dimensional surface condition is shown. This condition mostly occurs when low temperature growth continues for prolonged time. Streaks shorten and eventually are lost when the roughness is too high.

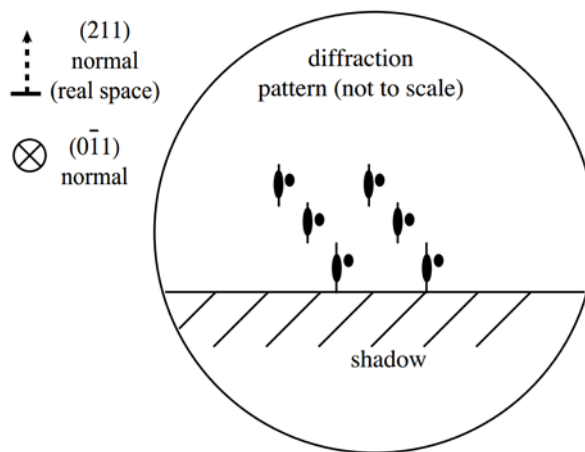


**Figure 4.8.** RHEED pattern from an unrecoverable rough surface [118]

If the growth conditions are far from ideal (as the case in **Figure 4.7**), single crystalline structure is lost, and the surface becomes very rough with polycrystalline domains. In this case, the RHEED pattern consists of circles in all azimuthal angles as shown **Figure 4.9**.

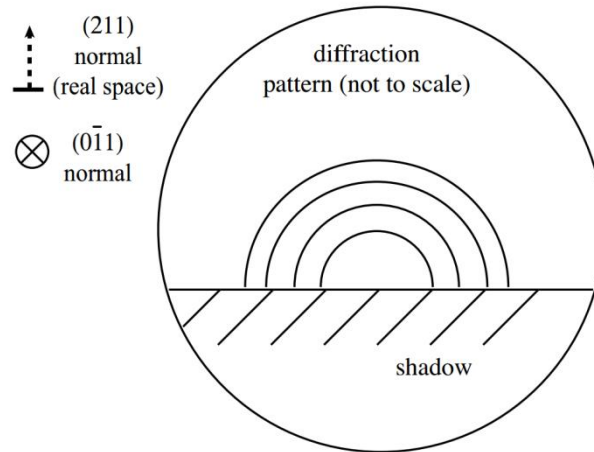


**Figure 4.9.** RHEED pattern from a polycrystalline surface [118]

### **Growth Monitoring and Spectral Ellipsometry Feedback:**

If the target epilayer design allows, it is more convenient to start with high Cd mole fraction for a better stabilization of the surface condition. As the Cd mole fraction increases, temperature sensitivity of the growth parameters decreases, favoring healthier growth initialization.

After the growth initialization, surface state and alloy composition is continuously monitored with SE. In the case of slight trend toward a deviation from target composition, required corrective action (flux increase/decrease) is immediately taken.

### **Growth End:**

After the completion of the epilayer structure growth is terminated by closing CdTe and Te shutters. The substrate is cooled down to room temperature under Hg flux. After the

removal of the substrate from the reactor, it is demounted from the Mo block by melting the indium on a hot plate. The remaining indium on the back side of the substrate is cleaned using HCl after masking the HgCdTe layer properly.

#### **4.1.4 Doping and Dopant Activation**

As grown HgCdTe layers exhibit p-type behavior due to Hg vacancies behaving as acceptor centers. Vacancy doped layers are sometimes used during p-n junction formations. However, vacancy doping is uncontrollable, unstable, and degrades the transport properties of the material. Hg vacancy density can be reduced down to values  $< 10^{13} \text{ cm}^{-3}$  after low temperature (220-250 °C) annealing under Hg overpressure [117].

Among the candidates for p-type dopants, Group I elements easily replace cation sites during optimally Te rich MBE growth conditions and results in excellent transport properties and minority carrier recombination times. However, their high diffusivity prevents their use in focal-plane array technology, since they diffuse out of the doped region during growth or post-growth annealing. As utilized in this work, more stable and controllable p-type layers can be achieved through extrinsic doping with low diffusivity Arsenic. The lattice incorporation and activation of As is not straightforward due to low sticking coefficient and site transfer requirement. Arsenic atoms adsorbed on the cation sites (which is favorable in Te rich growth conditions) need to be transferred to Te sites to behave as p-type dopants. This is realized with a short (20 min) high temperature annealing (430°C) under Hg overpressures. During this high temperature activation annealing, Te vacancies are created and arsenic is pushed towards these sites resulting in activation.

Stable and well controllable n-type doping is achieved by the in-situ indium incorporation. Indium does not require an activation process and easily replaces cation sites with high sticking coefficient insensitive to substrate temperature.

In this work, doping is performed with in-situ incorporations of As and In for p- and n-type dopants, respectively. The p-type dopant activation is performed with a relatively

short annealing at 430 °C which is followed by a vacancy filling annealing at 220-230 °C for a long duration.

## **4.2 HgCdTe Focal Plane Array Fabrication**

In this work, mesa architecture is adopted due to high controllability and simplicity of the process. The mesa architecture also reduces pixel-to-pixel cross talks improving image quality. The development of the processing steps and the related optimization work are described in the following sections.

### **4.2.1 Mesa Formation**

The mesa formation for isolated p-n junctions basically consists of etching of the HgCdTe layer down to n-type layer in a p-on-n structure as previously shown in **Figure 1.24**. Both wet chemical etching and plasma etching methods are investigated in this work to obtain the required mesa structure.

#### **Wet Etching:**

Wet chemical etching is the fundamental etching method free of surface damage and type conversion concerns. Available solutions for HgCdTe etching are alcoholic and acidic solutions of Br<sub>2</sub> in various compositions. The major drawbacks are large undercuts caused by perfectly isotropic etching, hard-to-achieve uniformity and repeatability. However up to 3 times better responsivity and lifetime values were reported when compared to CH<sub>4</sub>/H<sub>2</sub> Reactive ion etching method [119].

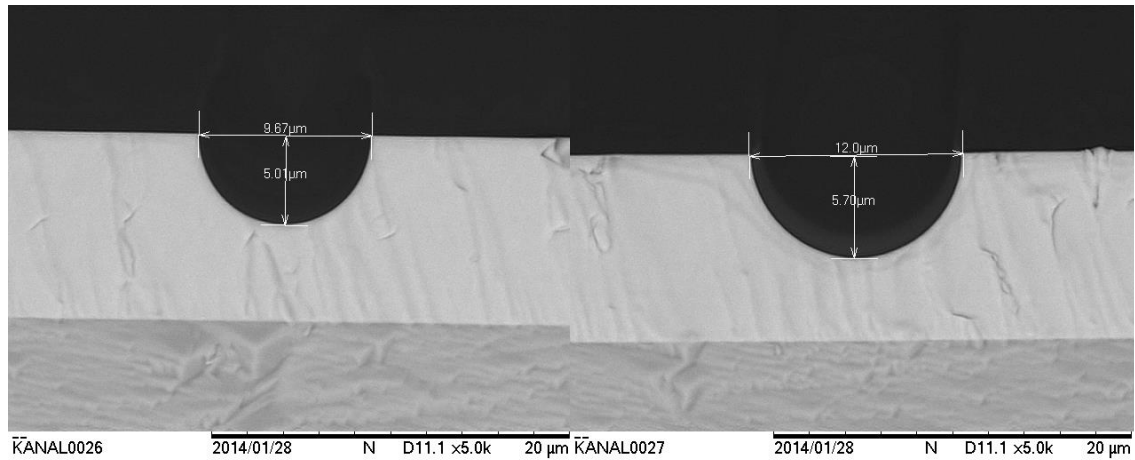
The solution preferred in this work is HBr:Br, since it is free of carbon contamination and easy to mask. The etching mechanism of this solution (and most of other possible solutions) is heavily diffusion controlled, and it is not possible to obtain a mechanism controlled by kinetics even at temperatures as low as -18 °C [120]. This diffusion limited nature of the etchant makes it harder to control the process, because the hydrodynamics and interface reactions govern the etch uniformity. During the fabrication of a focal plane

array, this results in a major problem since the inter-pixel area is less etched when compared to the other (open) areas. This is explained with the slower rate of renewal of species/reactants and the elimination of reaction products in the inter-pixel region with relatively narrow gaps between the pixels.

In order to quantify the etching behavior of the HBr:Br solution and establish process design rules for optimum etching uniformity, a systematic experiment was conducted in this work. In this experiment, 1, 2, 5, 10, 20, 50, 100, 200  $\mu\text{m}$  thick and 2mm long stripes with 200  $\mu\text{m}$  spacing were defined with photoresist on a LWIR HgCdTe thick layer with  $\sim 10$   $\mu\text{m}$  cut-off wavelength which was grown at the early stages of this thesis study. This pattern was etched with a freshly prepared HBr:Br solution. The sample was dipped into the solution with a horizontal holder and agitated with up/down motions in the beaker while the solution was stirred with a magnetic stirrer at the same time. After the etching, the sample was cleaved and the cross-sections of the stripes were inspected for etching profiles. The following results can be deduced after inspecting the etch profiles shown in **Figure 4.10**. These results are critically important while designing the process and lithography features.

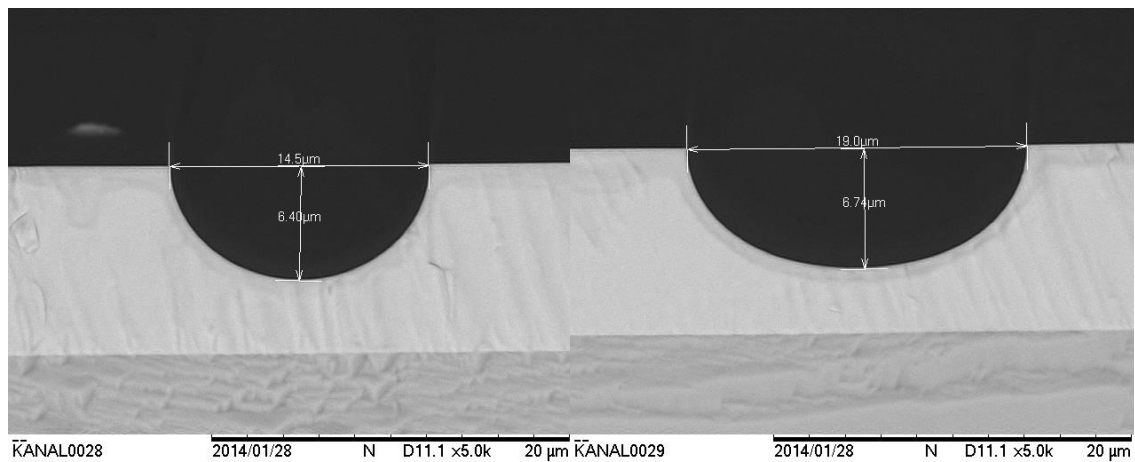
- The etching is perfectly isotropic leading to almost circular cross-sections at small stripe widths.
- The etch depth increases up to a stripe width of 10  $\mu\text{m}$ , then the etch depth saturates. For a rule of thumb, any orifice on photoresist smaller than 10  $\mu\text{m}$  will lead to a shallower etch than that of 10  $\mu\text{m}$  orifice.
- The elliptical etch profile is conserved up to stripe widths of 20  $\mu\text{m}$ . Beyond this stripe width, a loading effect from the large etched surface causes a decreased etch depth resulting a trench like profile near the sidewalls.
- When the etched area is large ( $>100$   $\mu\text{m}$ ) macroscopic scale hydrodynamics become effective (distance of the etching surface to the sample edge, agitating motion, holder shape, etc.). For example, the trench effect is heavier on the edge close to substrate boundary where there is a higher etchant flow.
- The etch depth achieved on the same sample can easily vary by  $\sim 30\%$  (5.0  $\mu\text{m}$  to 6.8 $\mu\text{m}$ ) depending on the lithography features.

- In order to achieve uniform etch depth across the sample, the ratio of etched/not-etched surfaces must be kept constant as much as possible by adding features to provide continuity of the uniformity.



(1  $\mu\text{m}$  stripe)

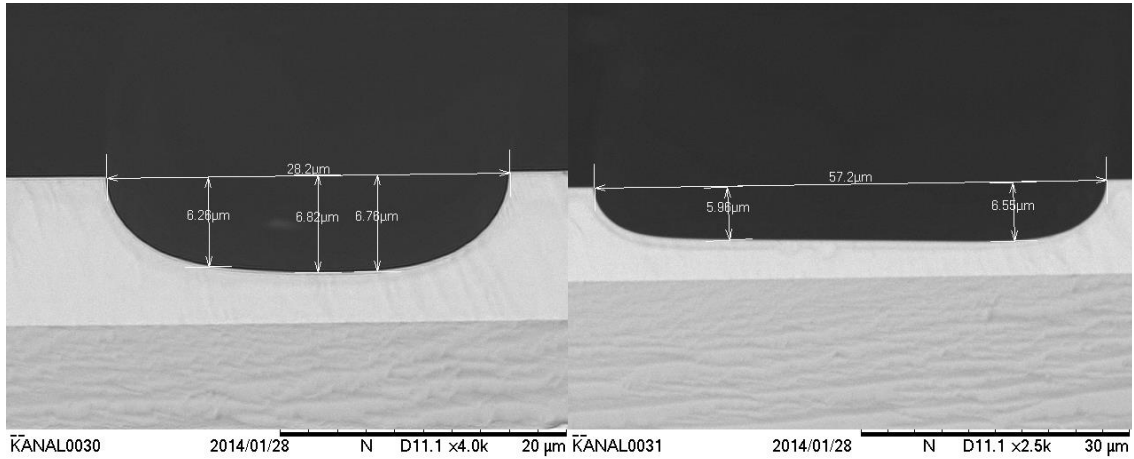
(2  $\mu\text{m}$  stripe)



(5  $\mu\text{m}$  stripe)

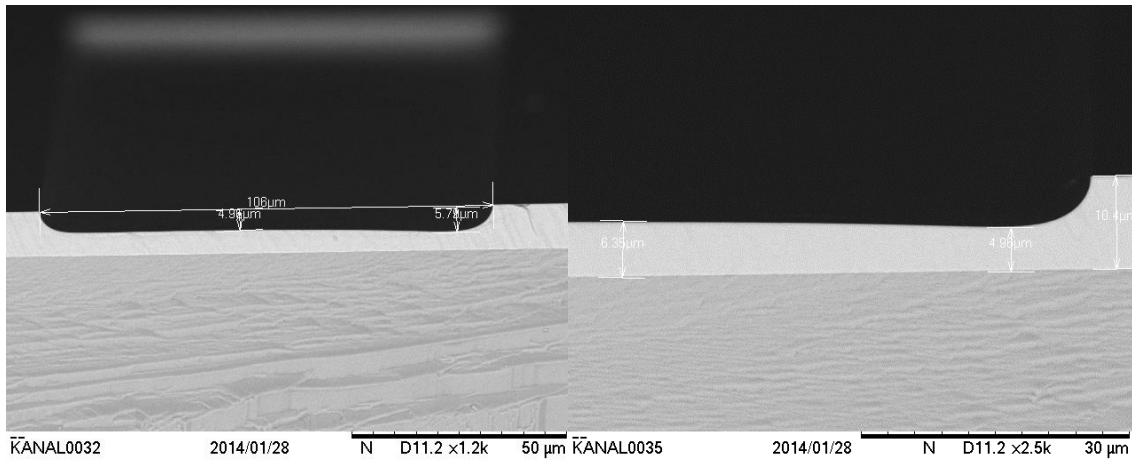
(10  $\mu\text{m}$  stripe)

**Figure 4.10.** Cross-sections of etched stripes with HBr:Br (stripe widths underneath)



(20 μm stripe)

(50 μm stripe)



(100 μm stripe)

(200 μm stripe)

**Figure 4.10** (Continued) Cross-sections of etched stripes with HBr:Br (stripe widths underneath)

In the light of the above observations and design rules, uniform mesa etching of multiple 640x512 format arrays on the same substrate (with a pitch as low as 15 μm) was obtained.

**Plasma Etching:**

In order to achieve higher aspect ratio required for smaller pixel pitch and/or deeper etches, development of plasma etching recipes is required. The Inductively Coupled

Plasma Reactive Ion Etching (ICP-RIE) method is known to provide smooth surfaces with low damage due to high density plasma with low ion energy [119]. Three different chemistry were used to etch HgCdTe in this work.

**CH<sub>4</sub>/H<sub>2</sub>/Ar:**

This chemistry is widely used by many groups. It is possible to obtain good surface roughness and nearly vertical sidewall. The drawback of this chemistry is the polymer by products formed during etching. These by products may lead to contamination of the system as well as forming thin layer depositions on the etched surface.

**BCl<sub>3</sub>/N<sub>2</sub>:**

Chlorine chemistry is relatively cleaner than CH<sub>4</sub>, and it possible obtain etching at lower ion energies. The etching profiles obtained with this chemistry are demonstrated in **Figure 4.11**.

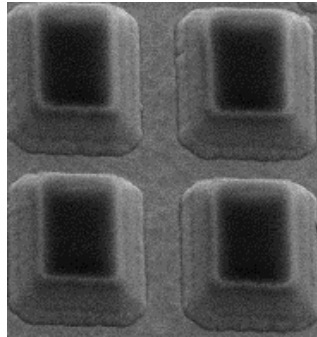


**Figure 4.11.** Etching profile obtained with BCl<sub>3</sub>/N<sub>2</sub> chemistry

**Ar:**

Taking the advantage of high ion density provided by ICP-RIE, pure physical etching of the HgCdTe with low energy argon sputter was also investigated. Smooth surfaces and sidewalls obtained with photoresist masked Ar sputter are shown in **Figure 4.12**. The angled sidewalls are desirable for more conformal passivation coating.

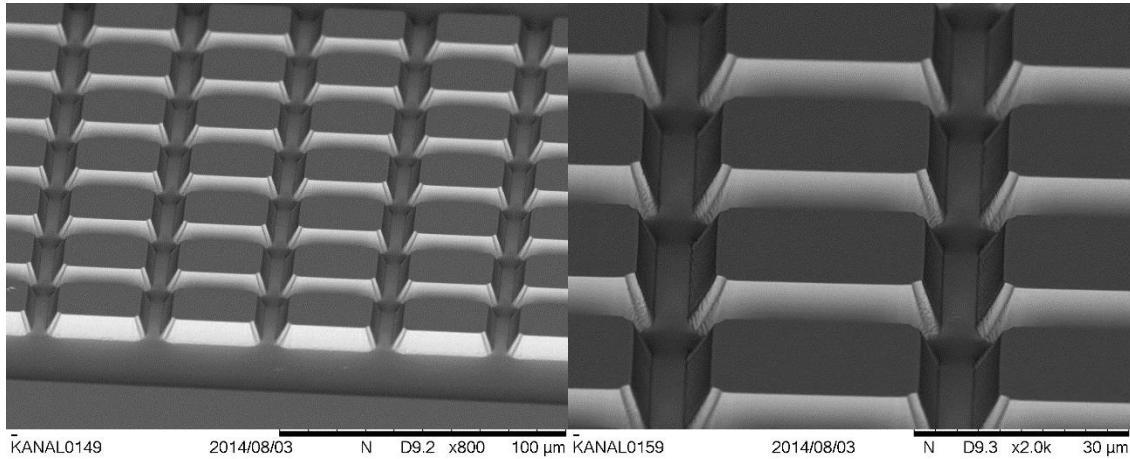


**Figure 4.12.** Etching profiles obtained with low energy argon sputter

As mentioned before, wet etching with  $\text{HBr}:\text{Br}_2$  was preferred in the fabrication of the photodiode arrays in this work, while several plasma etching methods were developed as well.

#### 4.2.2 Passivation

There are numerous methods reported in the literature on the passivation of  $\text{HgCdTe}$  including dielectric coatings, electrochemical depositions and anodic oxidations. Apart from research studies,  $\text{CdTe}$  is the common choice of passivation material for  $\text{HgCdTe}$  as accepted by the community. As the surface passivation is a performance limiting factor in most cases, the details of the passivation process are kept as a proprietary information by the detector manufacturers. In this work, evaporated  $\text{CdTe}$  coating is adopted as the surface passivation method. 6N purity  $\text{CdTe}$  is evaporated on the substrate immediately after mesa etching.

### **4.2.3 Ohmic Contact**

Ohmic contact formation was performed separately for n-type and p-type layers. In order to establish the ohmic contacts to the p-type cap layer, all epilayer structures were finalized with a thin (0.2  $\mu\text{m}$ ) semi-metallic HgTe layer.

### **4.2.4 UBM, Indium Bump Formation and Hybridization**

Under bump metallization and indium bump formations were performed using the lift-off method as previously described in QWIP fabrication. It is important to have sufficiently large photoresist thickness and proper sidewall profile in order to achieve uniform bump shape, especially when the pixel pitch is small ( $< 25 \mu\text{m}$ ). Otherwise, non-uniform bump heights with irregular bump shapes may result.

Temperatures used during the hybridization step of the of the HgCdTe detector arrays in this work were below those destroying the characteristics of HgCdTe. The substrate (ROIC) made of Si is heated more in order to introduce a slight stress in the indium bumps. This stress is introduced in a way to compensate for the stress that will arise when the hybrid is cooled to cryogenic temperatures. This technique can still be called cold compression since indium remains in the solid phase.

## **4.3 Achieved Results and Discussions**

LWIR HgCdTe epilayer structures were grown and scanning and staring FPAs were fabricated in this work using the procedures described up to here. In the following sections, properties of the epilayer structures and photodiodes will be presented.

### **4.3.1 Epilayer Structures**

A detailed numerical simulation for HgCdTe detectors was implemented in the content of a PhD study by another member of our group [121]. The results of the extensive simulations on LWIR HgCdTe photodiodes provided important information on the

performance limiting mechanisms of these photodetectors. It was shown that the most effective trap level degrading the detector performance was located at  $0.7E_g$  instead of  $0.5E_g$  which is generally believed to be the most efficient G-R level [121]. Additionally, the simulation results showed that for longer wavelengths ( $\lambda_c > 11 \mu\text{m}$ ), the detector performance is significantly affected by the trap assisted tunneling induced  $1/f$  noise for typically observed trap densities [121]. Furthermore, it was shown that Auger suppression had a twofold effect on the sensitivity of the detector by decreasing the dark current and increasing the photocurrent [122]. **Figure 4.13** shows the dependency of the responsivity on the absorber layer thickness as determined by the above mentioned study. The inset shows the effect of Auger recombination on the generated photocurrent. The predicted optimum absorber layer thickness value in the range  $8\text{-}10 \mu\text{m}$  (providing maximum responsivity) is in agreement with the typically used absorber layer thicknesses and the results from other groups [123].

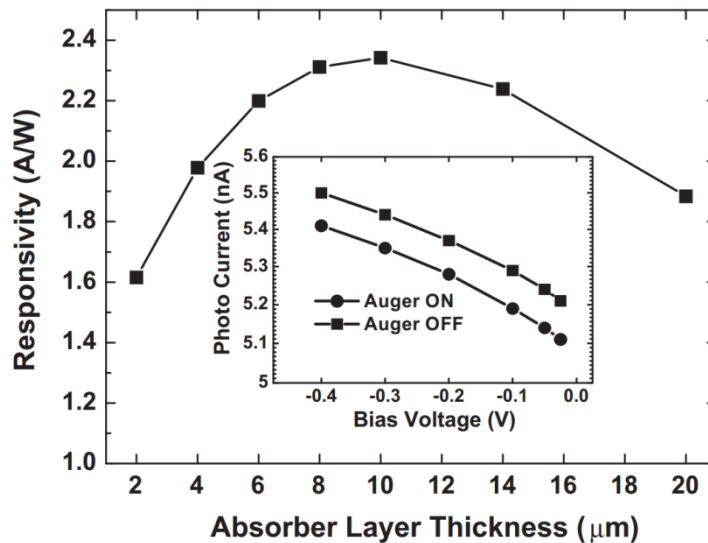


**Figure 4.13.** Responsivity versus absorber layer thickness ( $\lambda_c=10 \mu\text{m}$ , 77 K) [122]

One of the p-on-n heterojunction epilayer structures utilized in this work for LWIR mesa type photodiodes is shown in **Figure 4.14**.

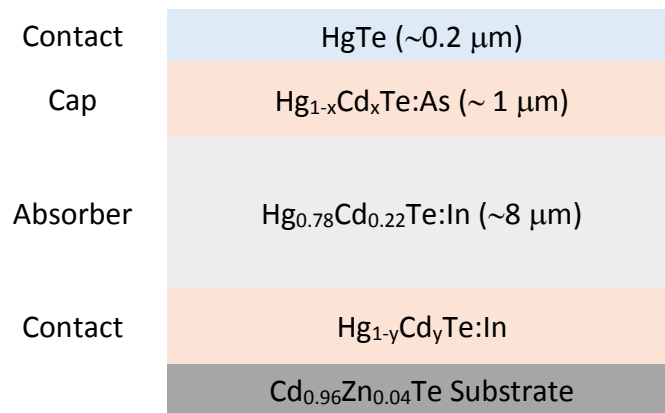


**Figure 4.14.** LWIR HgCdTe epilayer structure

The growth of the epilayer structure starts with an n-type doped Cd rich HgCdTe layer. High doping and Cd content in this layer decreases diffusion length along the common node and suppresses the pixel-to-pixel cross-talk. Additionally, higher Cd content in this layer facilitates growth initialization by decreasing temperature sensitivity of the growth conditions. The epilayer structure continues with the absorber layer, composition of which is precisely adjusted to the desired cut-off wavelength and continuously monitored with SE. The cap layer starts after switching of the dopant cells. The composition in the cap layer is higher than that of the absorber to minimize the contribution of the p-side to the dark current. Finally, CdTe and arsenic shutters are closed and a thin HgTe layer is grown for the facilitation of ohmic contacts.

After unloading the grown wafer and cleaning of the mounting indium, the room temperature FTIR transmission measurement was performed in order to check the absorber composition. The typical transmission curves for two different wafers (normalized to similar peak transmission) are shown in **Figure 4.15**. As reflected by this data, controllable and reproducible growth conditions were achieved in this work as indicated by the quite close cut-off wavelengths of the materials obtained in different growths.

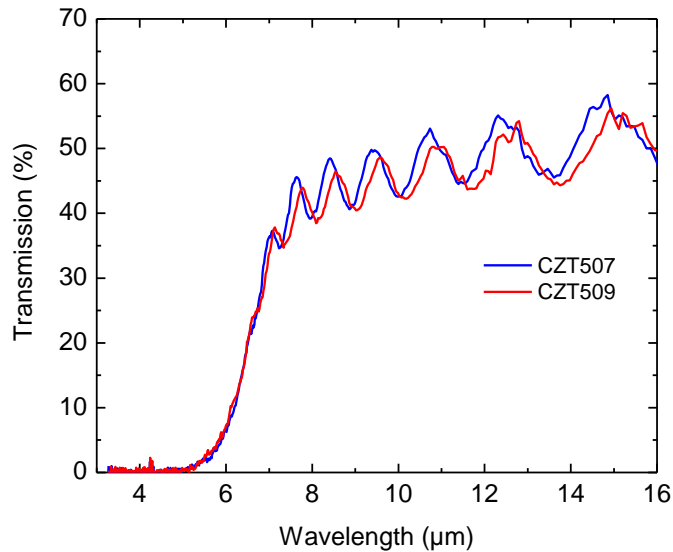


**Figure 4.15.** 300 K FTIR transmission of typical LWIR HgCdTe epilayers

### 4.3.2 FPA Implementation and Characterization

Linear and staring (2D) focal plane arrays were fabricated in this work using the epilayer structures grown on CdZnTe substrates (**Figure 4.14**) in our laboratory as well as those structures grown on Si substrates. The pixel level characterization was performed by flip-chip bonding pixel arrays to Si fan-out substrates. This configuration allows direct electrical access to some of the pixels on the array and facilitates optical and electrical characterization without the interaction of the pixels with the ROIC. The optical characterization was performed with a blackbody source integrated with a chopper, a transimpedance preamplifier, a lock in amplifier and an FTIR system. The detector was mounted inside an LN<sub>2</sub> dewar for the measurements.

Electrical characterization of the pixels of a linear array on CdZnTe substrate with a cut-off wavelength of  $\sim 10 \mu\text{m}$  yielded the following (**Figure 4.16**) I-V characteristics in the reverse bias range typically used for these detectors. The  $R_{DA}$  (dynamic resistance-area product) of the pixels is as high as  $\sim 2000 \Omega\text{-cm}^2$  near 50 mV reverse bias at 78 K. The pixels are 92% BLIP (300 K background) with  $f/2$  optics at 78 K. The peak responsivity

of the pixels are  $\sim 7.4$  A/W corresponding to a quantum efficiency of  $\sim 90\%$ . The peak detectivity of the pixels is as high as  $1.28 \times 10^{11} \text{ cm}\sqrt{\text{Hz}}/\text{W}$  with f/1 optics which is comparable to those of the best LWIR HgCdTe detectors with similar cut-off wavelength supplied by the well known manufacturers. The detector noise was measured at 2 kHz which is well below the Nyquist frequency of a typical HgCdTe imaging system. It should be noted that the pixel detectivity will further improve when measured with larger f-number apertures. The above results demonstrate successful design and implementation of the material growth and FPA fabrication processes. Detector properties achieved in this work meet the requirements of the high performance imaging systems.

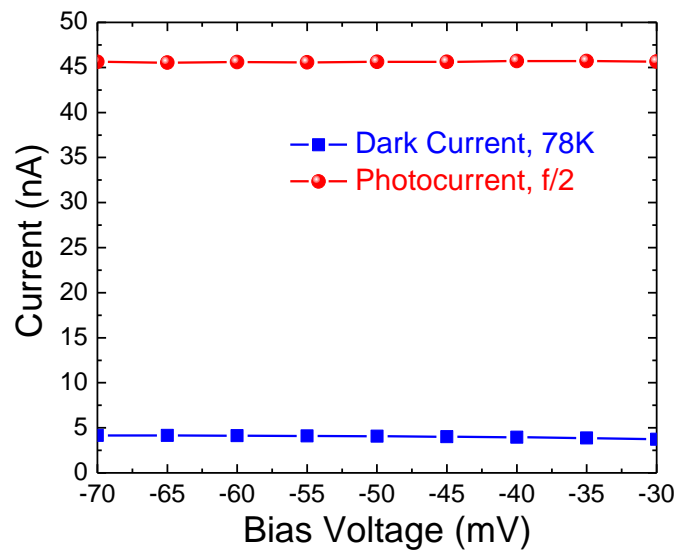


**Figure 4.16.** Dark and photocurrents of  $\sim 10 \mu\text{m}$  cut-off LWIR photodiode

We have also fabricated staring LWIR HgCdTe FPAs on CdZnTe and Si substrates in this work. The picture of a 320x256 format FPA hybridized to the ROIC is presented in **Figure 4.17**. Test detectors (including pixel arrays identical to the FPA pixels) were fabricated with the FPA and hybridized to Si fan-out circuits for detailed electrical and optical characterization. The characteristics of the staring FPA pixels on CdZnTe

substrates are similar to those of the linear array presented above. A thermal image recorded with a 320x256 LWIR HgCdTe FPA on Si substrate is shown in **Figure 4.18**. Most of the pixels of the FPA are operable in spite of the very large lattice mismatch between Si and HgCdTe making the growth of detector quality material extremely difficult.



**Figure 4.17.** 320x256 HgCdTe FPA hybridized with ROIC



**Figure 4.18.** Thermal image recorded with 320x256 FPA fabricated with LWIR HgCdTe detector epilayer structure grown on Si substrate

## CHAPTER 5

### EXTENDED WAVELENGTH InGaAs SWIR FOCAL PLANE ARRAYS

This part of the thesis describes our studies toward the implementation and characterization of solid source MBE grown large format (640x512) extended short wavelength infrared (SWIR) InGaAs FPA with  $\sim 2.7 \mu\text{m}$  room temperature cut off wavelength. While being among the best performance (if not the best) reported extended InGaAs FPAs with similar cut off wavelengths, the FPA yielded very good response linearity, as well as impressively low responsivity nonuniformity and excellent pixel operability of 5.5% and 99.8%, respectively, in spite of the large lattice mismatch (2%) between the InGaAs absorber layer and the InP substrate. The remarkable results presented in this chapter serve as an invaluable guide for further development of this important SWIR sensor technology as an alternative to costly HgCdTe detectors.

#### 5.1 Introduction

There has been huge improvement in the  $\text{In}_x\text{Ga}_{1-x}\text{As}$  sensor technology lattice matched to InP ( $x=0.53$ ) utilized mainly for night vision [124-128]. The room temperature dark current density of these detectors has been reduced to the order of  $\text{nA/cm}^2$  allowing imaging under very low flux levels. This advancement is also promising for the development of extended wavelength InGaAs sensors with cut-off wavelengths beyond  $1.7 \mu\text{m}$  as an alternative to short wavelength infrared (SWIR) HgCdTe technology with,

presumably, higher production cost. Wider availability of III-V material growth infrastructure and the relative ease of access to these facilities establish a higher potential for the rapid development of III-V sensors when compared with their II-VI counterparts. The main difficulty encountered in obtaining detector quality extended wavelength  $\text{In}_x\text{Ga}_{1-x}\text{As}$  material is the lattice mismatch with the matured substrates such as InP and GaAs. Having a smaller degree of lattice mismatch with  $\text{In}_x\text{Ga}_{1-x}\text{As}$  at the compositions of interest, InP is more promising as the substrate material even though GaAs technology allows larger substrate sizes. Lattice mismatch of  $\text{In}_x\text{Ga}_{1-x}\text{As}$  (with InP) increases as  $x$  deviates from 0.53 and reaches  $\sim 2\%$  at the composition corresponding to a room temperature cut-off wavelength of  $\sim 2.7 \mu\text{m}$ . As displayed by the previous studies on other lattice mismatched semiconductor systems, this degree of lattice mismatch is high enough to severely degrade the properties of the detector unless the epilayer structure is carefully designed and grown in order to confine the defects to the buffer layers and obtain a reasonably good quality absorber layer which has low enough electrically active defect density. The main objective of this study is to demonstrate the feasibility of large format extended InGaAs FPA implementation with very good imaging performance with a cut-off wavelength as high as  $\sim 2.7 \mu\text{m}$ , as well as identifying the origin of the performance limiting mechanisms in these detectors. In order to shed light on the development of the technology, a short survey of the achievements reported to date on the extended InGaAs detectors on InP substrates with the emphasis on cut-off wavelengths near  $2.5 \mu\text{m}$  at  $\sim 200 \text{ K}$ , is reported below.

Earlier work on the growth of extended InGaAs detectors utilized the hydride vapor phase epitaxy technique with InGaAs [129] or InAsP [130-132] buffers on InP substrates. Martinelli *et al.* [129] obtained room temperature dark current density of  $18.2 \text{ mA/cm}^2$  (bulk generated) under  $0.5 \text{ V}$  reverse bias in mesa type photodetectors with graded  $\text{In}_x\text{Ga}_{1-x}\text{As}$  buffer layer and  $5 \mu\text{m}$  thick n-type ( $N_D=2 \times 10^{15} \text{ cm}^{-3}$ )  $\text{In}_{0.82}\text{Ga}_{0.18}\text{As}$  absorber layer ( $\sim 2.6 \mu\text{m}$  room temperature cut-off wavelength). The detectors yielded a quantum efficiency of 75% ( $2.55 \mu\text{m}$ ) with front side illumination. Olsen *et al.* [130] used step graded  $\text{InAs}_y\text{P}_{1-y}$  buffer layers with  $3 \mu\text{m}$  thick  $\text{In}_{0.82}\text{Ga}_{0.18}\text{As}$  absorber layer in a planar type detector structure and obtained a room temperature dark current density of  $11.5$

$\text{mA/cm}^2$  (1 V reverse bias) with 1 A/W responsivity at 2.5  $\mu\text{m}$ . Linga *et al.* [131] used a similar approach with 3  $\mu\text{m}$  thick  $\text{In}_{0.82}\text{Ga}_{0.18}\text{As}$  absorber layer and obtained room temperature dark current density of  $9.7 \text{ mA/cm}^2$  (5 V reverse bias) and 1.1 A/W responsivity (2.38  $\mu\text{m}$ ) corresponding to an external quantum efficiency of 60%. Joshi *et al.* [132] employed hydride vapor phase epitaxy technique to grow InGaAs detector (planar type) epilayer structure with various cut-off wavelengths and step graded InAsP buffer layers. The grading was adjusted to keep the lattice mismatch below 0.13% between the neighboring layers. The detectors with cut-off wavelength of 2.2  $\mu\text{m}$  yielded a room temperature dark current density of  $4 \text{ }\mu\text{A/cm}^2$  (10 mV reverse bias). When the absorber layer ( $\text{In}_{0.71}\text{Ga}_{0.29}\text{As}$ ) doping density was increased from  $5 \times 10^{15}$  to  $5 \times 10^{17} \text{ cm}^{-3}$ , the dark current was decreased by a factor of four. The authors attributed this observation to a decrease in the G-R current as a results of the decrease in the depletion width.

Recent studies concentrated on growth techniques such as molecular beam epitaxy (MBE) and metal organic chemical vapor deposition (MOCVD) which are more promising toward obtaining better uniformity over a large area [133]. Kochhar *et al.* [133] used MBE technique to grow 2.2  $\mu\text{m}$  cut-off detectors with 1  $\mu\text{m}$  thick  $\text{In}_{0.74}\text{Ga}_{0.26}\text{As}$  absorber layer and a linearly graded InGaAs buffer layer. The detectors yielded room temperature dark current density of  $1.8 \text{ mA/cm}^2$  (1 V reverse bias) and responsivity of  $\sim 0.75 \text{ A/W}$ .

D'Hondt *et al.* [134] investigated the MOCVD grown  $\text{In}_{0.82}\text{Ga}_{0.18}\text{As}$  detectors with  $\text{InAs}_y\text{P}_{1-y}$  and  $\text{In}_x\text{Ga}_{1-x}\text{As}$  buffer layers. The InAsP buffer seemed to perform better than InGaAs in terms of detector  $R_0A$  product and crystal quality while linear grading in the buffer layer seemed to be better than step grading. It was also shown that the mesa type detectors (when compared with planar-type) had a larger dark current arising from the mesa surface. Room temperature  $R_0A$  product as high as  $2.04 \text{ }\Omega\text{-cm}^2$  was provided by a detector grown on  $2^\circ$  off InP substrate with a thick (7  $\mu\text{m}$ ) step graded InAsP buffer. D'Hondt *et al.* [135] also investigated the absorber layer doping density on the dark current of MOCVD grown planar type  $\text{In}_{0.82}\text{Ga}_{0.18}\text{As}$  detectors with step graded InAsP buffer layers. While the lowest room temperature dark current was achieved with n-type

absorber layer doping density of  $1\text{-}2 \times 10^{17} \text{ cm}^{-3}$ , the lowest dark current density ( $1 \times 10^{-9} \text{ A/cm}^2$ ) at low temperature (150 K) was exhibited by the detector with absorber layer doping density of  $5 \times 10^{16} \text{ cm}^{-3}$  with the dark current dominated by G-R and tunneling components. The highest quantum efficiency (66% at  $2 \text{ }\mu\text{m}$ ) was achieved with the detector with the unintentionally doped absorber layer, while the detectors with absorber layer doping density of  $1 \times 10^{17}$  and  $2 \times 10^{17} \text{ cm}^{-3}$  yielded quantum efficiencies lower by 15% and 50%, respectively. This observation was attributed to the reduction in the depletion width with increasing absorber layer doping density.

Nelson *et al.* [136] tested a  $512 \times 512 \text{ In}_{0.83}\text{Ga}_{0.17}\text{As}$  FPA with  $27 \text{ }\mu\text{m}$  pitch and measured pixel dark current of  $2.6 \text{ e}^-/\text{sec}$  at 80 K. The pixels yielded  $\sim 70\%$  quantum efficiency with  $\sim 2.3 \text{ }\mu\text{m}$  cut-off wavelength. The histogram of the pixel response (to flat field) yielded a full width at half maximum (FWHM) of  $\sim 8\%$  with 95% of the pixels displaying similar behavior.

Zhao-Bing *et al.* [137] investigated the characteristics of gas source molecular beam epitaxy (GSMBE) grown InGaAs detectors with  $2.66 \text{ }\mu\text{m}$  room temperature cut-off wavelength. A linearly graded  $n^+ \text{-In}_x\text{Al}_{1-x}\text{As}$  ( $x: 0.52 \rightarrow 0.85$ ) buffer layer,  $2.5 \text{ }\mu\text{m}$  thick  $n^- \text{-In}_{0.85}\text{Ga}_{0.15}\text{As}$  absorber layer and  $0.6 \text{ }\mu\text{m}$  thick  $p^+ \text{In}_{0.85}\text{Al}_{0.15}\text{As}$  cap layer was included in the detector epilayer structure on InP substrate. The mesa type detectors with PECVD (plasma enhanced chemical vapor deposition)  $\text{Si}_3\text{N}_4$  passivation yielded  $R_oA$  values of 0.94 and  $24.3 \text{ }\Omega\text{-cm}^2$  at 290 and 150 K, respectively. The dark current densities were  $\sim 1 \times 10^{-2}$  and  $\sim 4 \times 10^{-4} \text{ A/cm}^2$  at 290 and 150 K under 10 mV reverse bias voltage with dark current activation energy of 0.182 eV in the temperature range 210-300 K. The detectors exhibited peak detectivity of  $4.96 \times 10^9 \text{ cmHz}^{1/2}/\text{W}$  at room temperature.

Yuan *et al.* [138] reported MOCVD grown (with InAsP buffer) extended InGaAs FPA with  $320 \times 256$  format and  $30 \text{ }\mu\text{m}$  pitch. The pixel quantum efficiencies were  $\sim 80\%$  and  $\sim 50\%$  at  $2.0$  and  $2.4 \text{ }\mu\text{m}$ , and the decrease in quantum efficiency with increasing wavelength was attributed to the free carrier absorption in the  $n^+$  buffer layers and the substrate.

Li *et al.* [139] reported the characteristics of GSMBE grown p on n InGaAs detectors with 2.88  $\mu\text{m}$  room temperature cut-off wavelength. The detector epilayer structure included 2.4  $\mu\text{m}$  thick linearly graded  $n^+ \text{-In}_x\text{Al}_{1-x}\text{As}$  ( $x$ : 0.52 $\rightarrow$ 0.90) buffer layer, 2.0  $\mu\text{m}$  thick (lightly Si doped)  $n^- \text{-In}_{0.90}\text{Ga}_{0.10}\text{As}$  absorber layer and 0.6  $\mu\text{m}$  thick  $p^+ \text{-In}_{0.90}\text{Al}_{0.10}\text{As}$  cap layer on InP substrate. The mesa type detectors with PECVD (plasma enhanced chemical vapor deposition)  $\text{Si}_3\text{N}_4$  passivation yielded  $R_0A$  values of 3.2 and 17  $\Omega\text{-cm}^2$  at 290 and 250 K, respectively.

The dark current densities were  $\sim 3 \times 10^{-3}$  and  $\sim 2 \times 10^{-4}$   $\text{A/cm}^2$  at 290 and 250 K under 10 mV reverse bias voltage. Due to the presence of tunneling related dark current components below 250 K, the authors concluded that it might not be possible to significantly enhance the performance of these detectors by lowering the operation temperature. The detectors exhibited peak detectivity of  $6.6 \times 10^9$   $\text{cmHz}^{1/2}/\text{W}$  at room temperature.

Li *et al.* [140] compared the characteristics of GSMBE grown mesa and planar type  $\text{In}_{0.83}\text{Ga}_{0.17}\text{As}$  detectors with linearly graded  $n^+ \text{-In}_x\text{Al}_{1-x}\text{As}$  buffer layers, doping density of  $3 \times 10^{16}$   $\text{cm}^{-3}$  in the 1.5  $\mu\text{m}$  thick absorber and 200 K cut-off wavelength of  $\sim 2.45$   $\mu\text{m}$ . While planar type detectors exhibited higher responsivity when compared with mesa type detectors with conventional passivation (PECVD  $\text{SiN}_x$ ), the mesa type detectors with ICP-CVD (inductively coupled plasma chemical vapor deposition)  $\text{SiN}_x$  passivation exhibited the largest responsivity and lowest dark current. The authors attributed this observation to the larger minority carrier lifetime in the ICP-CVD  $\text{SiN}_x$  detector due to better passivated mesa surface.

While there exist numerous applications calling for 2D imaging in the SWIR band, there have been very few reports [136, 138] on the staring FPA fabrication of extended InGaAs detectors.

Based on the above presented survey, it can be concluded that the current status of the extended InGaAs detector technology with room temperature cut off near 2.7  $\mu\text{m}$  (200 K cut off  $\sim 2.5$   $\mu\text{m}$ ) offers dark current densities in the order of  $\text{mA/cm}^2$  near room temperature and  $\mu\text{A/cm}^2$  at  $\sim 200$  K which can be reached by Peltier coolers allowing a

wider utilization area in comparison to other (cryogenic) cooling techniques. It is not perfectly clear yet whether the mesa or planar type detectors offer the best available performance. While the mesa type detector has potential to generate somewhat higher surface leakage, diffusion (in the planar structure) into material with relatively high defect density may result in unexpected characteristics as well. Considering the fact that majority of the previous work reports bulk generated dark current, one can say that initial efforts toward  $R_0A$  improvement should be concentrated on the reduction of the bulk defect density instead of dealing heavily with better passivation of the mesa side walls. Reduction of the bulk generated dark current calls for purer material with lower defect density in order to obtain reasonably low G-R component in the dark current. There have been efforts to decrease the effects of G-R mechanism in extended InGaAs detectors by intentionally doping the absorber layer. However, noting that it does not seem to be possible to use these detectors with extended cut-off wavelengths near room temperature for imaging (cooling is necessary), introduction of relatively temperature independent current components such as tunneling (in order to decrease the G-R component) should be avoided, since the G-R current decreases, at least, in proportion to the intrinsic carrier concentration. Additionally, it has been shown that tunneling currents such trap assisted tunneling in low bandgap semiconductor detectors may be a considerable source of  $1/f$  noise even before they become visible in the dark current [141]. It may not be feasible to avoid these currents (with doped absorbers) by decreasing the reverse bias voltage to several millivolts in which case nonuniform bias voltage distribution on the pixels of a large format FPA will presumably be more disturbing. The presumably low diffusion length of the minority carriers (limiting the quantum efficiency) is another issue that should be considered while intentionally doping the absorber layer.

The information in the literature relating the epilayer quality to the buffer layer has not reached yet to a level sufficient to draw any definite conclusions about the optimum buffer material and thickness. However, it is clear that graded  $\text{InAs}_y\text{P}_{1-y}$  is not a proper buffer material for MBE growth due to the difficulty in precisely controlling the fluxes of two group V elements in this growth technique [131]. Regarding  $\text{In}_x\text{Ga}_{1-x}\text{As}$  and  $\text{Al}_y\text{In}_{1-y}\text{As}$ , there does not seem to be any definite reason to select  $\text{In}_x\text{Ga}_{1-x}\text{As}$  while

$\text{Al}_y\text{In}_{1-y}\text{As}$ , with a larger energy bandgap offers less absorption by the buffer layer as well as providing a proper cap layer with a low enough Al mole fraction [137, 139, 140]

In this section, the detailed characteristics of a solid source MBE grown 640x512 FPA with  $\text{In}_{0.83}\text{Ga}_{0.17}\text{As}$  absorber, linearly graded  $\text{In}_y\text{Al}_{1-y}\text{As}$  buffer layer and  $\text{In}_{0.83}\text{Al}_{0.17}\text{As}$  cap layer are presented. The results show that this technology has potential to compete with the SWIR staring HgCdTe FPA technology in terms of large format FPA level uniformity, pixel operability and sensitivity.

## 5.2 Epilayer Structure and MBE Growth

The detector epilayers were home-grown on semi-insulating (100) InP substrates in a Riber Epineat System with the structure shown in **Figure 5.1**. After the growth of a thin InGaAs lattice matched layer, the buffer layer was grown at constant growth rate ( $\sim 1.2\mu\text{m/h}$ ) by linearly shifting the indium and aluminum fluxes towards indium rich side. The temperature reading of the optical pyrometer during the buffer layer was kept around 460-465 °C, which is approximately 15 °C higher than absorber growth temperature. During the growth of the buffer layer, RHEED patterns were carefully monitored for indications of surface conditions and other crystallographic situations (e.g. crystal tilting [142]). The linearly graded (1.5  $\mu\text{m}$  thick)  $\text{In}_y\text{Al}_{1-y}\text{As}$  buffer ( $y: 0.52 \rightarrow 0.83$ ) was doped with Si at a concentration of  $N_D \sim 1 \times 10^{18} \text{ cm}^{-3}$ , while the 2.5  $\mu\text{m}$  thick  $\text{In}_{0.83}\text{Ga}_{0.17}\text{As}$  absorber was unintentionally doped. The  $\text{In}_{0.83}\text{Al}_{0.17}\text{As}$  cap and  $\text{In}_{0.83}\text{Ga}_{0.17}\text{As}$  contact layers were doped with Be at a density of  $N_A = 3 \times 10^{18} \text{ cm}^{-3}$ .

$\text{In}_{0.83}\text{Ga}_{0.17}\text{As}:\text{Be}$ , $t=0.2\ \mu\text{m}$
$\text{In}_{0.83}\text{Al}_{0.17}\text{As}:\text{Be}$ , $t=0.5\ \mu\text{m}$
$\text{In}_{0.83}\text{Ga}_{0.17}\text{As}:\text{undoped}$ , $t=2.5\ \mu\text{m}$
$\text{In}_{0.83}\text{Al}_{0.17}\text{As}:\text{Si}$ , $t=0.5\ \mu\text{m}$
$\text{In}_{0.52\rightarrow 0.83}\text{Al}_{0.48\rightarrow 0.17}\text{As}:\text{Si}$ , $t=1.5\ \mu\text{m}$
$\text{In}_{0.53}\text{Ga}_{0.47}\text{As}:\text{Si}$ , $t=0.2\ \mu\text{m}$
InP Substrate

**Figure 5.1.** Detector epilayer structure

The X-ray diffraction characterization of the grown wafer (including InAlAs and InGaAs epilayers lattice mismatched to the InP substrate) yielded a rocking curve (shown in Figure 5.2) FWHM of  $\sim 1000$  arc-sec which is close to the structural quality obtained with the other growth techniques [137]. The micrograph indicating the surface morphology of the epilayer is shown in Figure 5.3 which is similar to the previous observations by other groups [143]. The degradation in the surface morphology (when compared with lattice matched epilayers) is probably caused by the propagation of the roughness generated by the misfit dislocations up to the surface as the epilayers are grown [143]. The resultant thickness variation on the wafer surface is in the order of nanometers not considerably disturbing the fabrication of a large format FPA.

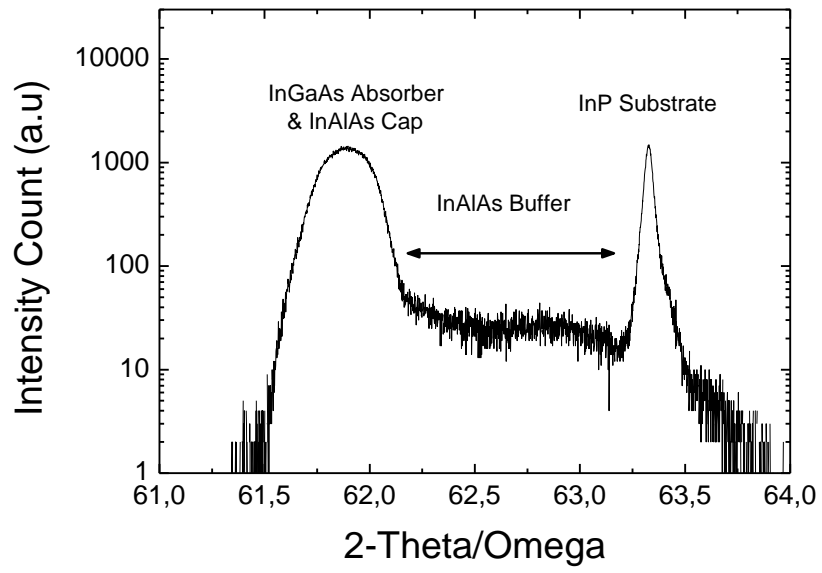


**Figure 5.2.** Rocking curve of detector epilayer structure

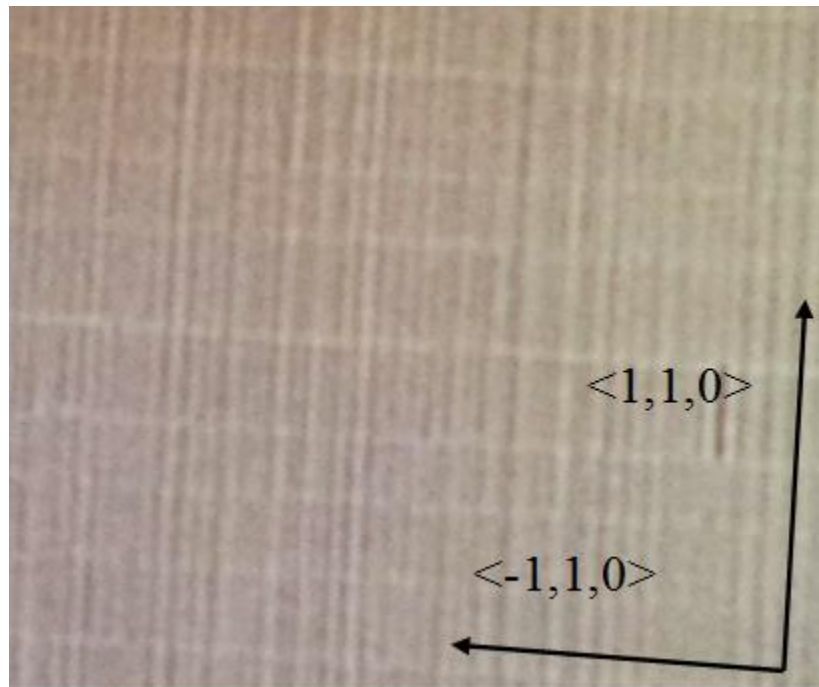


**Figure 5.3.** Surface morphology of a lattice mismatched extended InGaAs photodiode epilayer structure.

### 5.3 FPA Fabrication and Detailed Characterization

C-V measurements on the diode structures yielded a doping density of  $N_D=9 \times 10^{14} \text{ cm}^{-3}$  in the absorber layer. As demonstrated below, this doping density is low enough to suppress the tunneling currents under low and moderately large reverse bias voltages down to the typical operating temperature ( $\sim 200 \text{ K}$ ) of these detectors.

The FPA (640x512) pixel mesas (25  $\mu\text{m}$  pitch) were fabricated by wet etching after the formation of the ohmic contacts. Following passivation, under bump metallization and the formation of the In bumps, the FPA was flip-chip bonded to a read-out integrated circuit (ROIC) which is optimized for InGaAs detectors with a CTIA (capacitance transimpedance amplifier) input stage. After hybridizing with ROIC and underfilling, the substrate of the FPA was thinned to several tens of micrometers.

In order to perform pixel level characterization, test detectors identical to FPA pixels (in all aspects) were fabricated with the FPA. The test detector array was hybridized to a fan-out substrate by flip chip bonding and optical characterization was performed by back side illumination. In order to facilitate reliable electrical and optical measurements, 75 test pixels with similar properties were connected in shunt on the test pixel array/fan out hybrid. This arrangement allows the direct electrical and optical characterization of the FPA pixels without interacting with an ROIC

**Figure 5.4** shows the I-V characteristics of the pixels ( $\sim 20 \times 20 \mu\text{m}^2$ ) recorded at various temperatures in the range between 160-300 K. The dark current density at 180 K under 25 mV reverse bias voltage is  $0.48 \mu\text{A}/\text{cm}^2$  which is nearly three orders of magnitude lower than the previous results reported (at 150 K, 10 mV reverse bias) on GSMBE grown mesa-type large diameter (300  $\mu\text{m}$ ) detectors with InAlAs buffer and similar cut-off wavelength [137]. When compared with very recent results by Shi *et al.* [144] employing an improved passivation technique with ICP-CVD  $\text{SiN}_x$  to fabricate extended InGaAs detectors of similar cut-off wavelength, the dark current density (0.1 V reverse bias) achieved in this work is higher by a factor of  $\sim 2$  near room temperature and lower by a factor of  $\sim 13$  at 200 K.

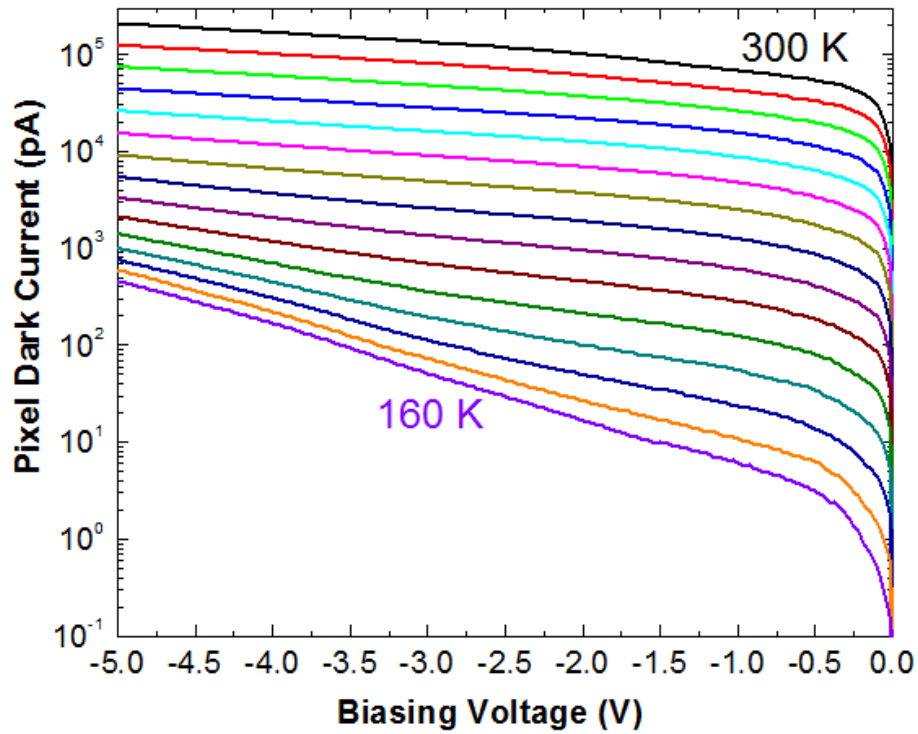


**Figure 5.4.** I-V characteristics of FPA pixels in the temperature range 160-300 K (10 K steps)

Dark current measurements on test detectors with different areas reflected mostly bulk generated dark currents. **Figure 5.5** shows the dark current activation energy displaying no considerable tunneling component above 200 K up to a reverse bias voltage of 3 V which can be attributed to the low unintentional doping density in the absorber layer. This characteristic facilitates improvement in the imaging performance (considerable dark current reduction) as the FPA is cooled down to ~200 K under low/moderate reverse bias voltage and below 200 K under low bias voltages, as well as avoiding the degrading effects of trap assisted tunneling in terms of adding additional noise mechanism. The activation energy being considerably below  $E_g/kT$  is an indication showing that the dominant dark current mechanism is not diffusion at or below room temperature.

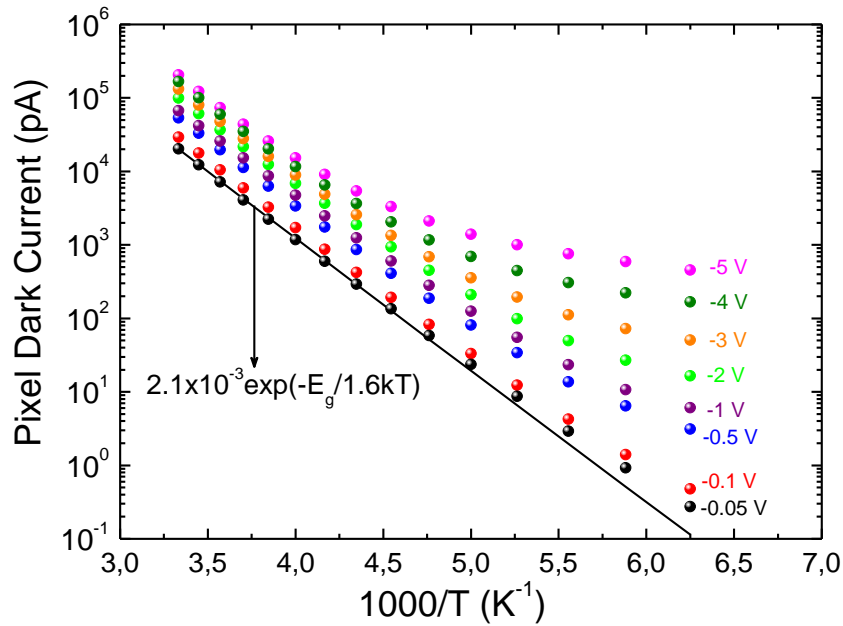


**Figure 5.5.** Dark current activation energy of FPA pixels

**Figure 5.6** shows the variation of the  $R_oA$  product with temperature. The activation energy is close to  $E_g/2$  suggesting that the dark current is dominated by the G-R mechanism near zero bias.  $R_oA$  activation energies as low as  $E_g/4$  were observed in HgCdTe detectors with high dislocation density ( $1 \times 10^7 \text{ cm}^{-2}$ ) [145]. The low reverse bias (25-50 mV) dynamic resistance-area product ( $R_d.A$ ) of the FPA pixels at 180 K reaches  $\sim 1 \times 10^5 \text{ } \Omega\text{-cm}^2$  which is high enough to offer sufficiently low Johnson noise and good enough injection efficiency in the FPA/ROIC hybrid.

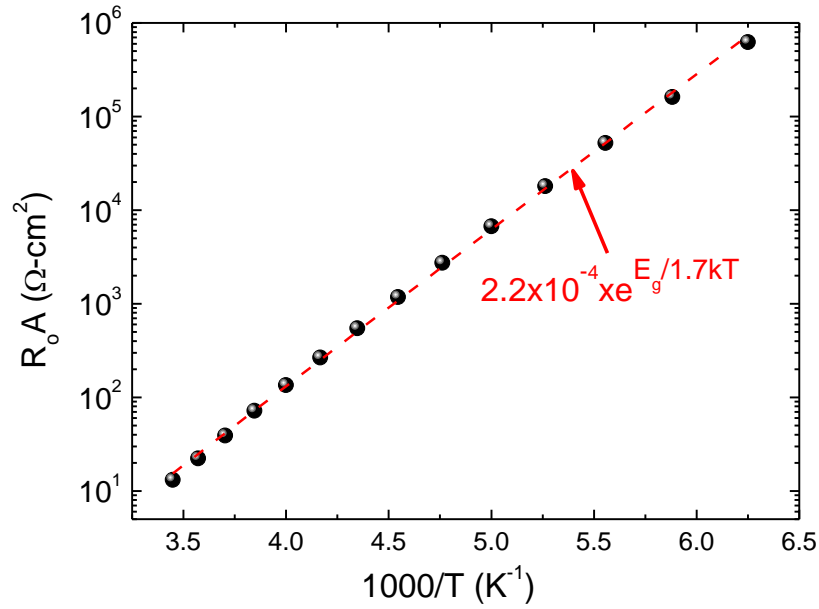


**Figure 5.6.** Variation of the  $R_oA$  product with temperature

In order to identify the dark current generation mechanisms, the dark current components at 300 and 200 K are given in **Figure 5.7** and **Figure 5.8** as determined through fitting the well-known expressions for the G-R, diffusion and shunt leakage mechanisms to the measured data. In terms of the effective G-R lifetime,  $\tau$ , the G-R current due to generation in the depletion region under sufficiently large reverse bias ( $|V| \gg kT/q$ ) can be expressed as

$$I_{GR} = q \frac{n_i W_{dep}}{\tau} A \quad (5.1)$$

where  $n_i$ ,  $W_{dep}$  and  $A$  are the intrinsic carrier concentration, depletion region width and the junction area. The shunt (ohmic) leakage exhibiting linear dependence on the applied bias voltage is known to be related with defects originating from lattice mismatch. It should be noted that  $R_{shunt}$  in these figures is the shunt resistance forming due to ohmic leakage component of the dark current (it is not the overall dynamic resistance of the detector). As can be seen from **Figure 5.7** and **Figure 5.8**,  $R_{shunt}$  is sufficiently high to make the G-R mechanism dominant component of the dark current under low reverse bias voltages (with a reasonably high effective G-R lifetime,  $\tau$ ). Therefore, the

dislocations degrade the detector performance under typical operating conditions mainly by limiting the G-R lifetime.

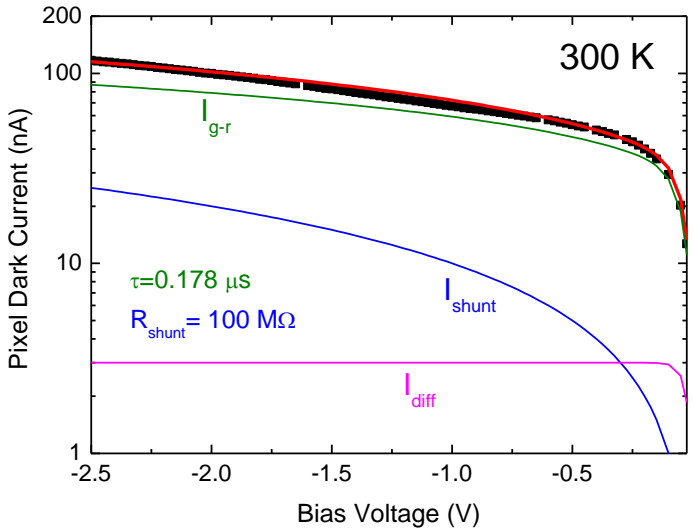


Figure 5.7. Dark current components at 300 K operation temperature.

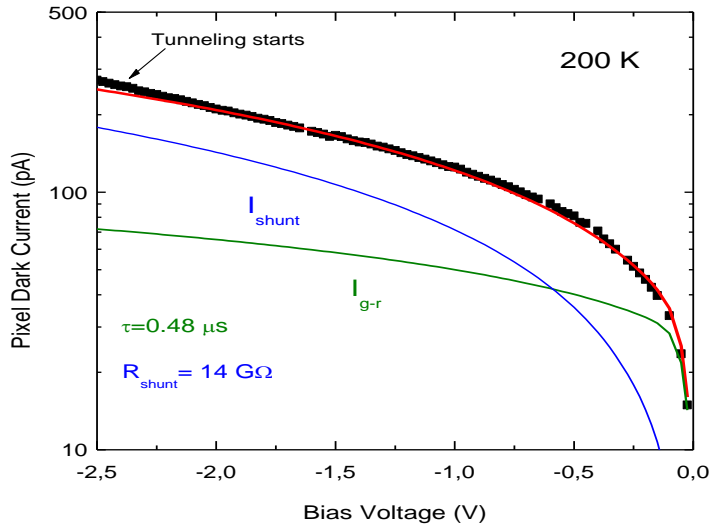
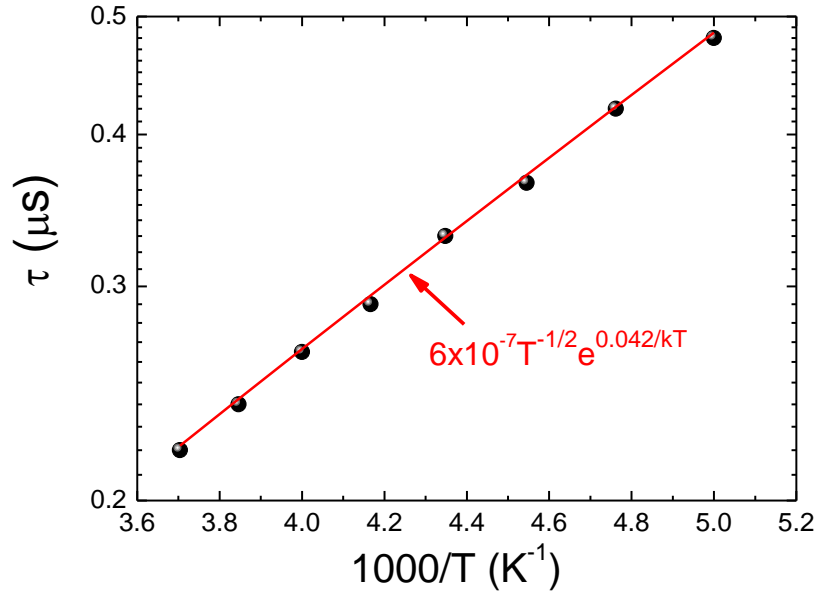


Figure 5.8. Dark current components at 200 K operation temperature

**Figure 5.9** presents the variation of the effective G-R lifetime with temperature. Note that the effective G-R lifetime ( $\tau$ ) expression includes both electron and hole lifetimes ( $\tau_n$  and  $\tau_p$ ). In case, a dominant trap state exists,  $\tau$  can be expressed as [146]

$$\tau = \frac{1}{\sigma_t v_{th} N_t} e^{\frac{E_t - E_i}{kT}} \quad (5.2)$$

where  $\sigma_t$  is the dominant capture cross section,  $v_{th}$  is the thermal velocity (proportional to  $T^{1/2}$ ),  $N_t$  is the trap density, and  $E_t$  is the dominant trap level energy with respect to the intrinsic level  $E_i$ . The fit to the measured data shown in **Figure 5.9** suggests (under the above assumption) that the dominant trap level (measured relative to  $E_i$ ) is 42 meV which is close to the midgap position. In the case of a dominant electron or hole trap, the carrier lifetime ( $1/\sigma_t v_{th} N_t$ ) at 200 K can be estimated to be around 40 ns. Further study involving deep level transient spectroscopy is needed to identify the detailed characteristics of the trapping sites. The effective G-R lifetime ( $\tau$ ) in our detectors is in the same order with the effective lifetime (0.82  $\mu$ s at 150 K) observed in the linear array detectors of the channel 8 in scanning imaging absorption spectrometer for atmospheric cartography (SCIAMACHY) [146]. More precisely, an effective G-R lifetime of 1.3  $\mu$ s can be estimated when the data in **Figure 5.9** is extrapolated to 150 K suggesting better material quality.



**Figure 5.9.** Variation of G-R lifetime with temperature

In **Figure 5.10**, the dark current components are shown in the 220-270 K operation temperature range. The ohmic leakage component becomes more effective in the high bias region as the temperature is decreased.

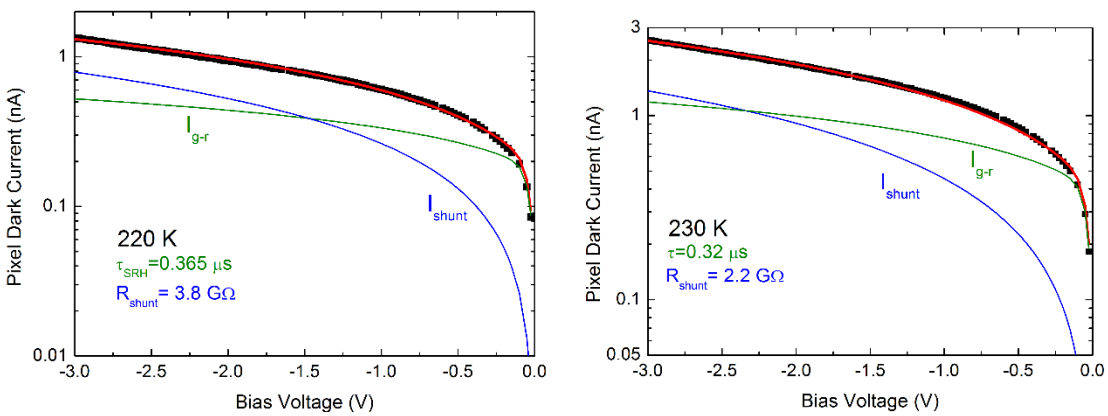


**Figure 5.10.** Dark current components between temperatures 220-270 K

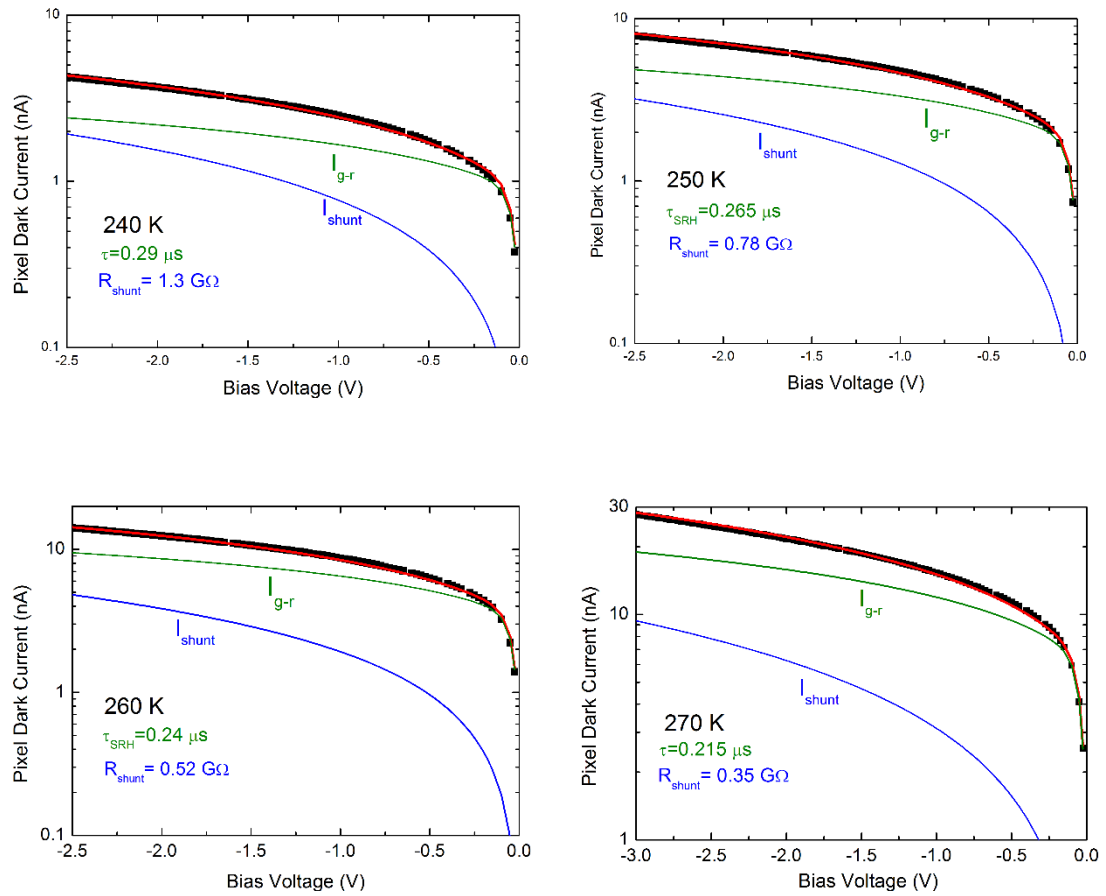


**Figure 5.10** (Continued) Dark current components between temperatures 220-270 K

**Figure 5.11** shows the variation of the shunt resistance with temperature. The activation energy being close to  $E_g/2$  suggests that ohmic leakage current due to dislocations increases roughly in proportion with  $n_i$  as predicted by the theoretical models [147].

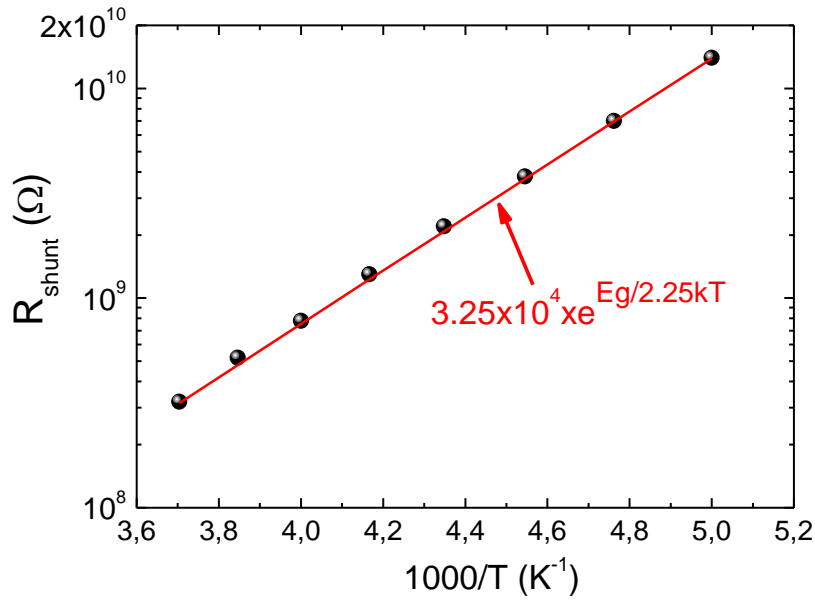


**Figure 5.11.** Variation of shunt resistance with temperature

The spectral quantum efficiency and detectivity of the FPA pixels at room temperature are shown in **Figure 5.12** and **Figure 5.13**. Since the detectors were not anti-reflection coated, the measured data was corrected to account for the surface reflection loss. The peak quantum efficiency is ~90% showing that 2.5 μm absorber layer thickness is sufficient to provide reasonably high absorption. The decrease in the quantum efficiency (with increasing wavelength) in the 1.75-2.5 μm wavelength interval is similar to the previous observations [138]. The room temperature peak detectivity near the cut-off wavelength is above  $2 \times 10^{10}$  cmHz<sup>1/2</sup>/W being close to the theoretical limit set by the Johnson noise of the detectors.

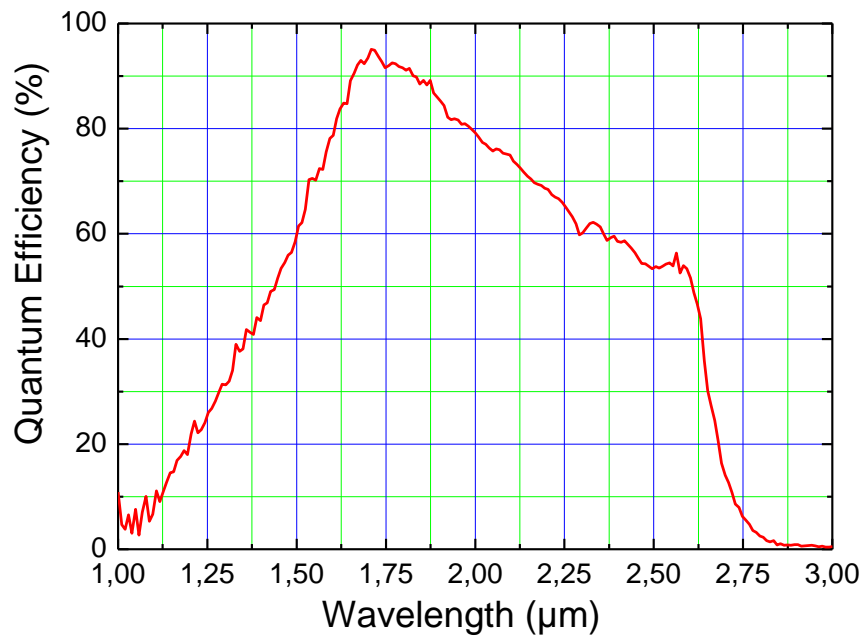


**Figure 5.12.** Spectral quantum efficiency of the FPA pixels

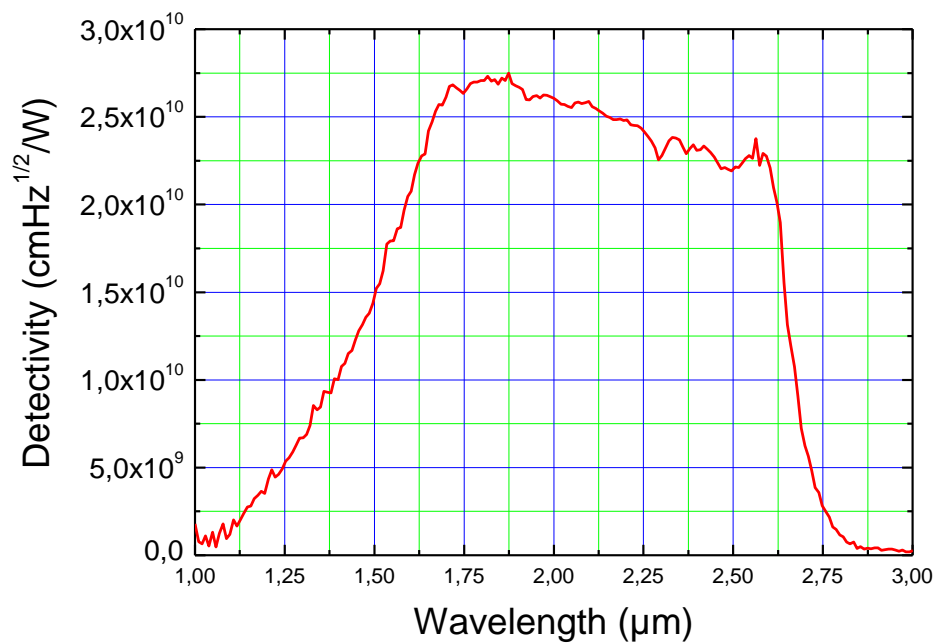


**Figure 5.13.** Spectral detectivity of the FPA pixels

Noise current spectral density of the FPA pixels (recorded with a dynamic signal analyzer) at 200 K operation temperature under 30 mV reverse bias is shown in **Figure 5.14** displaying no 1/f noise even under very low frequencies. The measured noise is equivalent to the Johnson noise of the pixel which exhibits a resistance of  $\sim 1.7 \text{ G}\Omega$  at the same operation temperature and biasing condition. This observation is another indication displaying that the FPA pixels under the given conditions do not suffer from dark current mechanisms such as tunneling currents creating 1/f noise and degrading the sensitivity of the pixels at the Nyquist frequency of the imager. The peak detectivity of the pixels is  $\sim 1 \times 10^{12} \text{ cmHz}^{1/2}/\text{W}$  showing a factor of  $\sim 40$  increase in the sensitivity when the detector is cooled from room temperature to 200 K. If the FPA is cooled to 180 K, additional increase in the detectivity by a factor  $\sim 3$  can be obtained.

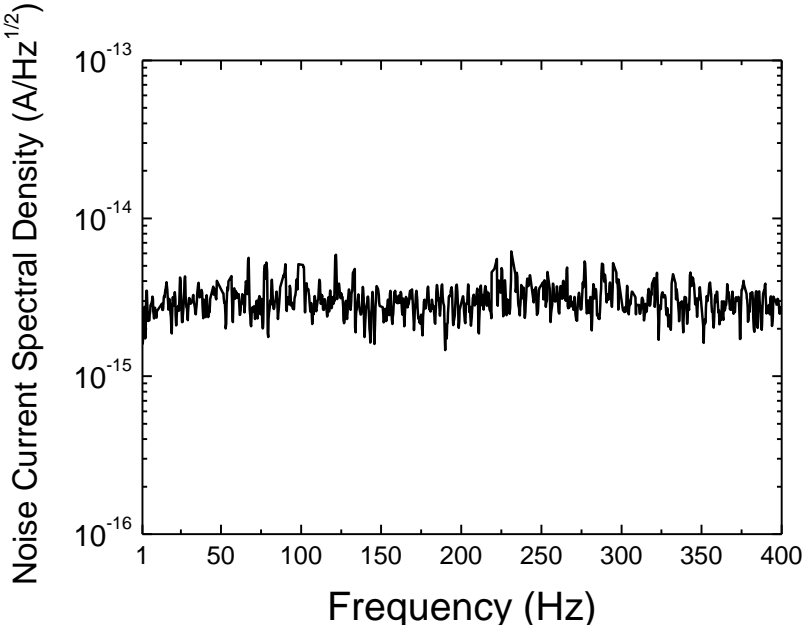


**Figure 5.14.** Noise current spectral density of the FPA pixels at 200 K under 30 mV reverse bias

The FPA level performance of the sensor was tested in a dewar with BK-7 window. The responsivity histogram (without field of view correction) of the FPA pixels with

responsivities within  $\pm 30\%$  of the mean responsivity is shown in **Figure 5.15** demonstrating excellent uniformity and 99.8% pixel operability. More than 95% of the pixels yield responsivities deviating by less than 10% from the mean responsivity. The operability of the FPA pixels is considerably better than the previous results on extended InGaAs linear FPAs in the planar structure with similar cut-off wavelengths [136]. While other explanations are possible, this can be attributed to the distorted p-type diffusion (due to dislocations) into the epilayers of the planar detector structure creating high electric-field regions opening channels for tunneling as explained by Hoogeveen *et al.* [146].

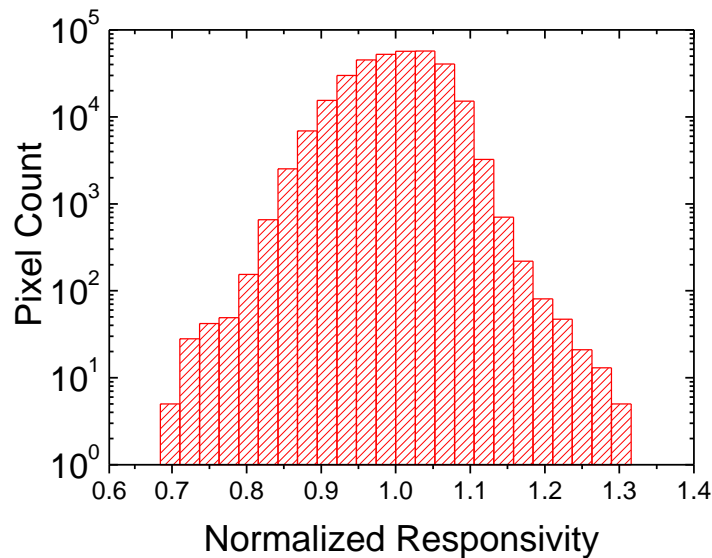


**Figure 5.15.** Responsivity histogram of the FPA pixels

**Figure 5.16** shows the filled capacity (%) of the ROIC versus the source radiance demonstrating the excellent linearity of the pixel responsivity. Two snap-shot images recorded with the FPA (without bad pixel correction) are shown in **Figure 5.17** demonstrating excellent imaging even with 1 point nonuniformity correction.

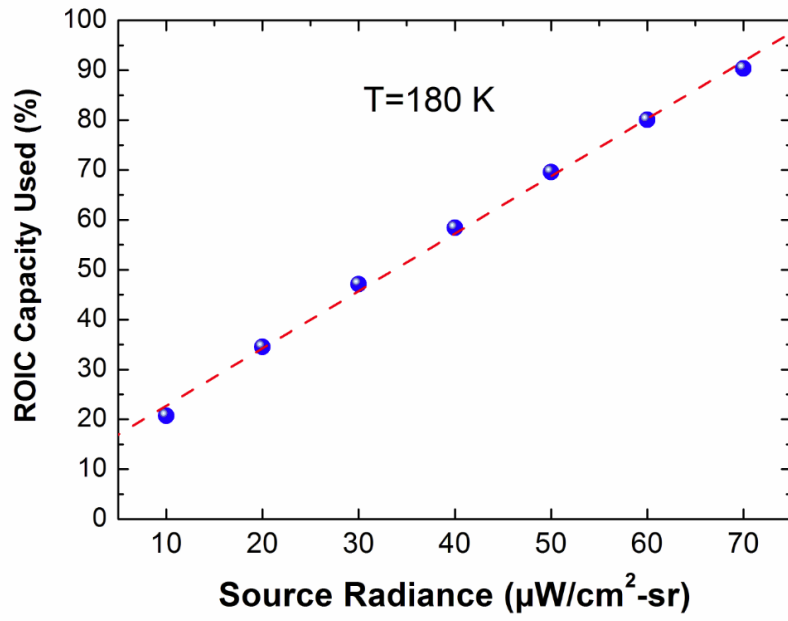


**Figure 5.16.** Filled ROIC capacity versus source radiance

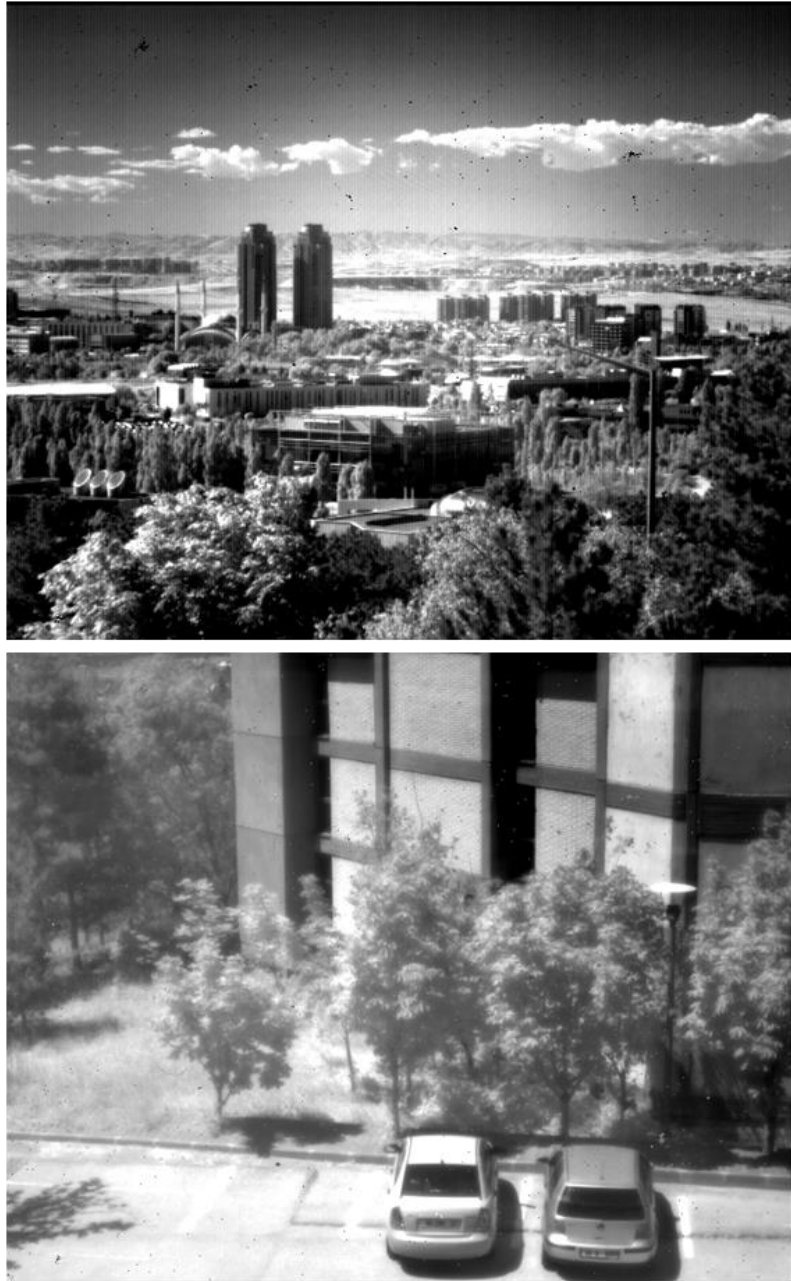


**Figure 5.17.** Snapshot images yielded by the FPA (at ~180 K) with 1 point nonuniformity correction and without bad pixel replacement

## 5.4 Conclusion

In this section the characteristics of 640x512 extended InGaAs FPA with room temperature cut-off wavelength of  $\sim 2.7 \mu\text{m}$  are presented. The results clearly show the feasibility of the large format staring array extended InGaAs detector technology up to this cut off wavelength. In the present work, sub-pico amper dark current levels achievable in the state of the art SWIR HgCdTe FPAs (with similar cut-off wavelength) at 200 K are obtained around the same temperature with low (several mV) reverse bias voltages, while the sensitivity, linearity and the uniformity of the FPA are remarkably good in spite of the large lattice mismatch. Since the sensitivity of the FPA pixels is limited by the Johnson noise, the initial steps for further performance improvement should include studies toward increasing the dynamic resistance of the pixels through the optimization of the buffer structure. While the planar structure may have potential for improvement to some degree, it should be noted that the mesa structure, presumably offers better modulation transfer function and flexibility to engineer the optical structure of the pixel [148]. The most important conclusion that should be drawn from this work is that desirable (comparable to SWIR HgCdTe) FPA performance is achievable with the extended InGaAs FPA technology with the mesa structure, solid source MBE growth technique and AlInAs which are not widely adapted by the extended InGaAs detector manufacturers.

## CHAPTER 6

### CONCLUSIONS AND FURTHER WORK

The principal objective of this thesis work was to provide significant contributions to the infrared photon detector technology through extensive studies targeting performance improvements in three different infrared FPA technologies: Quantum Well Infrared Photodetectors (QWIPs), HgCdTe sensors and extended InGaAs SWIR photodetectors. The work covers all stages of the focal plane array implementation including

- Design, synthesis and characterization of the detector material,
- Discrete detector and focal plane array microfabrications/hybridization
- Detailed characterization at both FPA and pixel levels

It has been nearly three decades since extensive research on quantum well infrared photodetectors (QWIPs) started. The initial results were encouraging in the sense that QWIP focal plane arrays (FPAs) displayed excellent uniformity, stability, reproducibility and high pixel operability which were more difficult to achieve with the HgCdTe sensor technology especially in the long- and very long-wavelength portion of the infrared band. However, the results also displayed the device as a low quantum ( $\eta$ ) and conversion ( $\eta.g$ ) efficiency photodetector which was unable to compete with HgCdTe sensors in terms of the ability to handle low background/short integration time applications. The low quantum efficiency has also kept the long-wavelength infrared (LWIR) QWIP operation temperature (60-65 K) considerably below that of a HgCdTe detector (77 K). These problems have not allowed widespread utilization of this technology in the field in spite

of the virtually unbeatable uniformity and stability it has offered. Due to this reason, HgCdTe sensors have remained in the field and market as the main solution to high end thermal imaging applications in the LWIR band while QWIP FPAs have continued to offer similar sensitivity levels at extended integration times and lower operation temperatures. In spite of this deficiency, LWIR QWIP FPAs were commercialized and successfully integrated into forward looking infrared (FLIR) systems thanks to its superiority in terms of uniformity, thermal cycling stability and low cost.

The objective of this thesis work toward the improvement of the QWIP technology has successfully been reached by demonstrating high enough pixel quantum efficiency (31%) and an adjustable gain in a wide range to provide the flexibility of adopting the sensor to different scene/imaging conditions. The achieved conversion gain is an order of magnitude larger than the typical gain obtained with the standard AlGaAs/QWIP FPA pixel. These results will serve as an invaluable guide for overcoming the limitations of this very important field-proven thermal imaging sensor technology.

HgCdTe is still the most widely utilized material to build the sensors of high-end infrared imaging systems. In this work, the production cycles of HgCdTe focal plane arrays were developed. Reproducible high quality material and desirable FPA pixel performance obtained have demonstrated the viability of the MBE growth technique which has recently started to be adopted by the detector manufacturers.

The objective of this thesis work related with the extended InGaAs SWIR sensor technology has also been reached with scientifically and technologically important results. Due to the large lattice mismatch even with the most promising substrate material, InP, it is generally believed that it is hard to achieve desirable FPA performance with the extended InGaAs sensors with cut-off wavelengths beyond 2.5  $\mu\text{m}$ . Indeed, some of the previous studies reported results which are not highly motivating toward the development of this sensor technology in the above described wavelength range. While, we have been able to implement and demonstrate a solid source (MBE) grown large format (640x512) extended short wavelength infrared (SWIR)  $\text{In}_{0.83}\text{Ga}_{0.17}\text{As}$  sensor with impressive performance at both pixel and FPA levels, we have also shown the feasibility

of the mesa structure, solid source MBE growth technique and AlInAs which are not widely adopted by the extended InGaAs detector manufacturers. These results will definitely strengthen the motivation toward the development of this technology as an alternative to HgCdTe SWIR FPA technology which calls for access to more restricted II-VI material infrastructure with higher production cost.

The subjects listed below are worth further investigation:

- Detailed theoretical study on the origin of the relatively high quantum efficiency observed in InP/InGaAs QWIP structures may open new doors for overcoming the main bottleneck of this sensor technology by investigating the other heterostructure semiconductor material systems which may offer even higher efficiencies.
- Complete electromagnetic modeling of the QWIP pixel geometry will be an extremely useful tool for optimization of the detector structures. These simulations will provide an understanding of the detector operation from electromagnetics point of view as well.
- The crystal tilting phenomena which may be encountered during lattice mismatched growth of extended InGaAs epilayers should be considered further. Hence, it may be an efficient way of lattice relaxation leading to a reduction in dislocation density which will probably result in a decrease in the G-R dark current component and an increase in the dynamic resistance of the detectors.



## REFERENCES

- [1] S. W. Herschel, "Experiments on the Refrangibility of the Invisible Rays of the Sun," *Philos. Trans. R. Soc. London*, vol. 90, pp. 284-292, 1800.
- [2] E. S. Barr, "The Infrared Pioneers - I. Sir William Herschel," *Infrared Phys.*, vol. 1, pp. 1-4, 1961.
- [3] T. Seebeck, in *Magnetische Polarisation der Metalle und Erze durch Temperatur-Differenz*, Berlin, Abh. Deutsch. Akad. Wiss., 1822, pp. 265-373.
- [4] E. S. Barr, "The Infrared Pioneers - II. Macedonio Melonni," *Infrared Phys.*, vol. 2, pp. 67-73, 1962.
- [5] E. S. Barr, "The Infrared Pioneers - III. Samuel Pierpoint Langley," *Infrared Phys.*, vol. 3, pp. 195-206, 1963.
- [6] W. Smith, "Effect of Light on Selenium During the Passage of an Electric Current," *Nature*, vol. 7, p. 303, 1873.
- [7] T. W. Case, "Notes on the change of resistance of certain substrates in light," *Phys. Rev.*, vol. 9, pp. 305-310, 1917.
- [8] W. D. Lawson, S. Nielsen, E. Putley and A. Young, "Preparation and Properties of HgTe and Mixed Crystals of HgTe-CdTe," *J. Phys. Chem. Solids*, vol. 9, pp. 325-329, 1959.

- [9] L. M. Birberman and R. L. Sendall, "Introduction: A Brief History of Imaging Devices for Night Vision," in *Electro-Optical Imaging: System Performance and Modeling*, Bellingham, SPIE Press, 2000, pp. 1-26.
- [10] L. Esaki and R. Tsu, "Superlattice and Negative Differential Conductivity in Semiconductors," *IBM J. Res. Dev.*, vol. 14, pp. 61-65, 1970.
- [11] L. Chang, L. Esaki and G. A. SaiHalaz, *IBM Tech. Discl. Bull.*, vol. 20, p. 2019, 1977.
- [12] L. Esaki and H. Sakaki, *IBM Tech Discl. Bull.*, vol. 20, p. 2456, 1977.
- [13] D. D. Coon and R. Karunasiri, "New Mode of IR Detection Using Quantum Wells," *Appl. Phys. Lett.*, vol. 45, pp. 649-651, 1984.
- [14] L. Chiu, J. Smith, S. Margalit, A. Yariv and A. Cho, "Application of Internal Photoemission from Quantum-well and Heterojunction Supperlattices to Infrared Detectors," *Infrared Phys.*, vol. 23, no. 2, pp. 93-97, 1983.
- [15] L. C. West and S. J. Eglash, "First Observation of an Extremely Large-dipole Infrared Transition Within the Conduction Band of a GaAs Quantum Well," *Appl. Phys. Lett.*, vol. 46, no. 12, pp. 1156-1158, 1985.
- [16] B. F. Levine, K. K. Choi, C. G. Bethea, J. Walker and R. J. Malik, "New 10  $\mu\text{m}$  infrared detector using intersubband absorption in resonant tunnelling GaAlAs superlattices," *Appl. Phys. Lett.*, vol. 50, no. 16, p. 1092, 1987.
- [17] G. A. SaiHalazs, R. Tsu and L. Esaki, "A new semiconductor superlattice," *Appl. Phys. Lett.*, vol. 30, no. 12, p. 651, 1977.

- [18] G. SaiHalazs, L. Chang, J. Welter, C. Chang and L. Esaki, "Optical Absorption of InGaAs-GaSbAs Superlattices," *Solid State Commun.*, vol. 27, no. 10, pp. 935-937, 1978.
- [19] D. Z.-Y. Ting, A. Soibel, L. Höglund, J. Nguyen, C. J. Hill, A. Khoshakhlagh and S. D. Gunapala, "Type-II Superlattice Infrared Detectors," in *Advances in Infrared Photodetectors*, S. D. Gunapala, D. R. Rhiger and C. Jagadish, Eds., London, Elsevier, 2011, p. 3.
- [20] M. J. E. Golay, "A Pneumatic Infrared Detector," *Rev. Sci. Instr.* , vol. 18, no. 5, pp. 357-362, 1947.
- [21] E. M. Wormser, "Properties of Thermistor Infrared Detectors," *J. Opt. Soc. Amer.*, vol. 43, no. 1, pp. 15-21, 1953.
- [22] R. W. Astheimer, "Thermistor Infrared Detectors," *Proc. SPIE.* , vol. 443, pp. 95-109, 1983.
- [23] G. W. McDaniel and D. Robinson, "Thermal Imaging by Means of the Evaporograph," *Appl. Opt.*, vol. 1, no. 3, pp. 311-324, 1962.
- [24] C. Hilsum and W. R. Harding, "The Theory of Thermal Imaging, and Its Application to The Absorption Edge Image-Tube," *Infrared Phys.*, vol. 1, pp. 67-93, 1961.
- [25] A. Gross, "The Pyroelectric Vidicon - A Review," *Proc. SPIE*, vol. 807, pp. 25-32, 1987.
- [26] A. Rogalski, "History of infrared detectors," *Opto-Electro. Rev.*, vol. 20, no. 3, 2012.

- [27] Wikipedia, 1 1 2014. [Online]. Available: <http://en.wikipedia.org/wiki/Infrared>.
- [28] IPAC-Caltech, 1 1 2014. [Online]. Available: <http://www.ipac.caltech.edu/outreach/Edu/importance.html>.
- [29] R. Hudson, *Infrared System Engineering*, New York: Wiley, 1969.
- [30] S. Özer, "InSb and InAsSb Infrared Photodiodes on Alternative Substrates and InP/InGaAs Quantum Well Infrared Photodetectors: Pixel and Focal Plane Array Performance," *PhD Dissertation*, Middle East Technical University, Electrical and Electronics Engineering, 2005.
- [31] R. G. Driggers, R. Vollmerhausen, J. P. Reynolds, J. Fanning and G. C. Holst, "Infrared detector size: how low should you go?," *Opt. Eng.*, vol. 51, no. 6, p. 063202, 2012.
- [32] J. T. Longo, D. T. Cheung, A. M. Andrews, C. C. Wang and J. M. Tracy, "Infrared Focal Planes in Intrinsic Semiconductors," *IEEE Trans. Electron Devices*, Vols. ED-25, no. 2, pp. 213-232, 1978.
- [33] P. Felix, M. Moulin, B. Munier, J. Portmann and J.-P. Reboul, "CCD Readout of Infrared Hybrid Focal-Plane Arrays," *IEEE Trans. Electron Devices*, Vols. ED-27, pp. 175-188, 1980.
- [34] A. Rogalski, *Infrared Detectors*, 2nd ed., Boca Raton: CRC Press, 2011, pp. 662-665.
- [35] P. R. Norton, "Infrared detectors in the next millenium," *Proc. SPIE*, vol. 3698, pp. 652-665, 1999.

- [36] R. C. Jones, Performance of Detectors for Visible and Infrared Radiation, L. Morton, Ed., New York: Academic Press, 1952.
- [37] R. C. Jones, "Phenomenological Description of the Response and Detecting Ability of Radiation Detectors," *Proc. IRE*, vol. 47, pp. 1495-1502, 1959.
- [38] H. Schneider and H. C. Liu, Quantum Well Infrared Photodetectors, Physics and Applications, Heidelberg: Springer-Verlag, 2007.
- [39] B. F. Levine, "Quantum well infrared photodetectors," *J. Appl. Phys.*, vol. 74, no. 8, pp. R1-R81, 1993.
- [40] J. L. Pan and C. G. Fonstad Jr., "Theory, fabrication and characterization of quantum well infrared photodetectors," *Mat. Sci. Eng.*, vol. 28, pp. 65-147, 2000.
- [41] S. D. Gunapala, S. Bandara, J. Liu, E. Luong, S. Rafol, J. Mumolo, D. Ting, J. Bock, M. Ressler, M. Werner, P. LeVan, R. Chehayeb, C. Kukkonen, M. Levy, P. LeVan and M. Fauci, "Quantum well infrared photodetector reearch and development at Jet Propulsion Laboratory," *Infrared Phys. Technol.*, vol. 42, pp. 267-282, 2001.
- [42] Y. Fu, M. Willander, W. Lu, W. L. Xu, N. Li, N. Li, Q. Liu, Y. D. Chen and S. C. Shen, "Near-field coupling effect in normal-incidence absorption of quantum-well infrared photodetectors," *J. Appl. Phys.*, vol. 85, no. 2, pp. 1237-1239, 1999.
- [43] S. Y. Wang and C. P. Lee, "Doping effect on normal incident InGaAs/GaAs long-wavelength quantum well infrared photodetectors," *J. Appl. Phys.*, vol. 82, no. 5, pp. 2680-2683, September 1997.

- [44] M. Helm, "The Basic Physics of Intersubband Transitions," in *Intersubband Transitions in Quantum Wells - Physics and Device Applications I*, H. C. Liu and F. Capasso, Eds., Academic Press, 2000, pp. 54-59.
- [45] K. Tsai, C. P. Lee, J. S. Tsang, H. R. Chen and K. Chang, "Two-Dimensional Bi-Periodic Grating Coupled One- and Two- Color Quantum Well Infrared Photodetector," *IEEE Electron Device Lett.*, vol. 16, no. 2, pp. 49-51, February 1995.
- [46] A. Nedelcu, H. Facoetti, E. Costard and P. Bois, "Small pitch, large format long-wave infrared QWIP focal plane arrays for polarimetric imagery," *Proc. SPIE*, vol. 6542, 2007.
- [47] J. Y. Andersson and L. Lundqvist, "Grating coupled quantum well infrared detectors: Theory and performance," *J. Appl. Phys.*, vol. 71, no. 7, pp. 3600-3610, April 1992.
- [48] A. De Rossi, E. Costard, N. Guerineau and S. Rommeluere, "Effect of finite pixel size on optical coupling in QWIPs," *Infrared Phys. Technol.*, vol. 44, pp. 325-330, 2003.
- [49] K. K. Choi, C. Monroy, A. Goldberg, G. Dang, M. Jhabvala, A. La, T. Tamir, K. M. Leung, A. Majumdar, J. Li and D. Tsui, "Designs and applications of corrugated QWIPs," *Infrared Phys. Technol.*, vol. 47, pp. 76-90, 2005.
- [50] K. K. Choi, C. Monroy, V. Swaminathan, T. Tamir, M. Leung, J. Devitt, D. Forrai and D. Endres, "Optimization of corrugated-QWIPs for large format, high quantum efficiency, and multi-color FPAs," *Infrared Phys. Technol.*, vol. 50, pp. 124-135, 2007.

- [51] K. Choi, M. D. Jhabvala, D. Forrai, A. Waczynski, J. Sun and R. Jones, "Electromagnetic modeling of QWIP FPA pixels," *Proc. SPIE*, vol. 8012, 2011.
- [52] K. K. Choi, D. P. Forrai, D. Endres, J. P. P. Sun and J. W. Devitt, "C-QWIP focal plane arrays," *Infrared Phys. Technol.*, vol. 52, pp. 364-370, 2009.
- [53] W. A. Beck and M. S. Mirotznik, "Microstrip antenna coupling for quantum-well infrared photodetectors," *Infrared Phys. Technol.*, vol. 42, pp. 189-198, 2001.
- [54] W. Wu, A. Bonakdar and H. Mohseni, "Plasmonic enhanced quantum well infrared photodetector with high detectivity," *Appl. Phys. Lett.*, vol. 96, no. 161107, 2010.
- [55] W. Wu, A. Bonakdar, R. Gelfand and H. Mohseni, "A normal-incident quantum well infrared photodetector enhanced by surface plasmon resonance," *Proc. SPIE*, vol. 7780, 2010.
- [56] S. Kalchmair, H. Dets, G. D. Cole, A. M. Andrews, P. Klang, M. Nobile, R. Gansch, C. Ostermaier, Schrenk and G. Strasser, "Photonic crystal slab quantum well infrared photodetector," *Appl. Phys. Lett.*, vol. 98, no. 011105, 2011.
- [57] K. K. Choi, M. D. Jhabvala, J. Sun, C. A. Jhabvala, A. Waczynski and K. Olver, "Resonator-quantum well infrared photodetectors," *Appl. Phys. Lett.*, vol. 103, no. 201113, 2013.
- [58] J. Sun, K. K. Choi and A. Olver, "Fabrication of resonator-quantum well infrared photodetector test devices," *J. Micro/Nanolith. MEMS MOEMS*, vol. 31, no. 013004, 2014.

- [59] S. Gunapala, B. F. Levine, D. Ritter, R. Hamm and M. B. Panish, "InGaAs/InP long wavelength quantum well infrared photodetectors," *Appl. Phys. Lett.*, vol. 58, pp. 2024-2026, 1991.
- [60] Y. Gusakov, E. Finkman, G. Bahir and D. Ritter, "The effect of strain in InP/InGaAs quantum-well infrared photodetectors on the operating wavelength," *Appl. Phys. Lett.*, vol. 79, pp. 2508-2510, 2001.
- [61] B. F. Levine, A. Y. Cho, J. Walker, R. J. Malik, D. A. Kleinman and D. L. Sivco, "InGaAs/InAlAs multiquantum well intersubband absorption at a wavelength of 4.4  $\mu\text{m}$ ," *Appl. Phys. Lett.*, vol. 52, no. 18, p. 1481, 1988.
- [62] S. Ozer, U. Tumkaya and C. Besikci, "Large Format AllInAs-InGaAs Quantum Well Infrared Photodetector Focal Plane Array for Midwavelength Infrared Thermal Imaging," *IEEE Photon. Technol. Lett.*, vol. 19, no. 18, pp. 1371-1373, Sept. 2007.
- [63] S. Gunapala, B. F. Levine, D. Ritter, R. Hamm and M. B. Panish, "Lattice matched InGaAsP/InP longwavelength quantum well infrared photodetectors," *Appl. Phys. Lett.*, vol. 60, pp. 636-638, 1992.
- [64] S. D. Gunapala, B. F. Levine, D. Ritter, D. Hamm and M. B. Panish, "InP-based quantum-well infrared photodetectors," *Proc. SPIE*, vol. 1541, pp. 11-23, Nov. 1991.
- [65] S. Ozer, U. Tumkaya, B. Asici and C. Besikci, "Demonstration and Performance Assessment of Large Format InP-InGaAsP Quantum-Well Infrared Photodetector Focal Plane Array," *IEEE J. Quantum Electron.*, vol. 43, no. 8, pp. 709-713, 2007.

- [66] C. Jelen, S. Slivken, J. Hoff, M. Razeghi and G. J. Brown, "Aluminum free GaInP/GaAs quantum well infrared photodetectors for long wavelength detection," *Appl. Phys. Lett.*, vol. 70, no. 3, p. 360, 1997.
- [67] S. D. Gunapala, B. F. Levine, R. A. Logan, T. Tanbun-Ek and D. A. Humphrey, "GaAs/GaInP multiquantum well long-wavelength infrared detector using bound-to-continuum state absorption," *Appl. Phys. Lett.*, vol. 57, no. 17, p. 1802, 1990.
- [68] H. C. Liu, "Quantum Well Infrared Photodetector Physics and Novel Devices," in *Intersubband Transitions in Quantum Wells - Physics and Device Applications I*, H. C. Liu and F. Capasso, Eds., Academic Press, 2000, pp. 129-278.
- [69] M. Kaldirim, S. U. Eker, Y. Arslan, U. Tumkaya and C. Besikci, "Large-Format Voltage-Tunable Dual-Color Midwavelength Infrared Quantum-Well Infrared Photodetector Focal Plane Array," *IEEE Photonics Technol. Lett.*, vol. 20, no. 9, pp. 709-711, May 2008.
- [70] B. F. Levine, S. D. Gunapala, J. M. Kuo, S. S. Pei and S. Hui, "Normal incidence hole intersubband absorption long wavelength GaAs/AlGaAs quantum well infrared photodetectors," *Appl. Phys. Lett.*, vol. 59, no. 15, p. 1864, 1991.
- [71] S. D. Gunapala, B. F. Levine, D. Ritter, R. Hamm and M. B. Panish, "InGaAs/InP hole intersubband normal incidence quantum well infrared photodetector," *J. Appl. Phys.*, vol. 71, no. 5, p. 2458, 1992.
- [72] S. U. Eker, Y. Arslan, M. Kaldirim and C. Besikci, "QWIP FPAs on InP Substrates for Single and Dual Band Thermal Imagers," *Infrared Phys. Technol.*, vol. 52, 385-390 2009.

- [73] K. K. Choi, M. D. Jhabvala and R. J. Peralta, "Voltage-Tunable Two-Color Corrugated-QWIP Focal Plane Arrays," *IEEE Electron Device Lett.*, vol. 29, no. 9, pp. 1011-1013, Sept. 2008.
- [74] S. D. Gunapala, S. V. Bandara, J. K. Liu, J. M. Mumolo, D. Z. Ting, C. Hill, J. Nyguen, B. Simolon, J. Woolaway, S. C. Wang, W. Li, P. D. LeVan and M. Tidrow, "Demonstration of Megapixel Dual-Band QWIP Focal Plane Array," *IEEE J. Quantum Electron.*, vol. 46, no. 2, Feb. 2010.
- [75] G. L. Hansen, J. L. Schmit and T. N. Casselman, "Energy gap versus alloy composition and temperature in  $\text{Hg}_{1-x}\text{Cd}_x\text{Te}$ ," *J. Appl. Phys.*, vol. 53, no. 10, pp. 7099-7101, 1982.
- [76] W. M. Higgins, G. N. Pults, R. G. Roy, R. A. Lancaster and J. L. Schmit, "Standard relationships in the properties of  $\text{Hg}_{1-x}\text{Cd}_x\text{Te}$ ," *J. Vac. Sci. Technol. A*, vol. 7, no. 2, pp. 271-275, 1989.
- [77] P. Norton, "HgCdTe Infrared Detector," *Opto-Electron. Review*, vol. 10, no. 3, pp. 159-174, 2002.
- [78] M. A. Kinch, *Fundamentals of Infrared Detector Materials*, Bellingham: SPIE, 2007.
- [79] A. Rogalski, "HgCdTe infrared detector material: history, status and outlook," *Rep. Prog. Phys.*, vol. 68, p. 2267-2336, 2005.
- [80] F. Aqariden, P. D. Dreiske, M. Kinch, P. K. Liao, T. Murphy, H. F. Schaake, T. Shafer, H. Shih and T. Teherani, "Development of Molecular Beam Epitaxially Grown HgCdTe for High-Density Vertically-Integrated Photodiode-Based Focal Plane Arrays," *J. Electron. Mater.*, vol. 36, no. 8, pp. 900-904, 2007.

- [81] J. M. Armstrong, M. R. Skokan, M. A. Kinch and J. D. Luttmer, "HDVIP five-micron pitch HgCdTe focal plane arrays," *Proc. SPIE*, vol. 9070, p. 907033, 2014.
- [82] E. P. G. Smith, R. E. Bornfreund, I. Kasai, L. Phan, E. Pattern, J. M. Peterson, J. A. Roth, B. Z. Nosh, T. J. DeLyon, J. Jensen, J. W. Bangs, S. M. Johnson and W. A. Radford, "Status of Two-Color and Large Format HgCdTe FPA Technology at Raytheon Vision Systems," *Proc. SPIE*, vol. 6127, 2007.
- [83] M. F. Vilela, K. R. Olsson, E. M. Norton, J. M. Peterson, K. Rybnicek, D. R. Rhiger, C. W. Fulk, J. W. Bangs, D. D. Lofgreen and S. M. Johnson, "High-Performance M/LWIR Dual-Band HgCdTe/Si Focal-Plane Arrays," *J. Electron. Mater.*, vol. 42, no. 11, pp. 3231-3238, 2013.
- [84] P. Tribolet, G. Destefanis, P. Ballet, J. Baylet, O. Gravrand and J. Rothman, "Advanced HgCdTe Technologies and Dual-band Developments," *Proc. SPIE*, vol. 6940, 2008.
- [85] Y. Reibel, N. Pere-Laperne, T. Augey, L. Rubaldo, G. Decaens, M. Bourqui, A. Manissadjian and D. Billon-Lanfrey, "Getting Small, new 10  $\mu\text{m}$  pixel pitch cooled infrared products," *Proc. SPIE*, vol. 9070, 2014.
- [86] J. Ziegler, J. Wenisch, R. Breiter, D. Eich, H. Figgemeieri, P. Fries, H. Lutz and R. Wollrab, "Improvements of MCT MBE Growth on GaAs," *J. Electron. Mater.*, vol. 43, no. 8, pp. 2935-2940, 2014.
- [87] G. Gaussorgues, *Infrared Thermography*, Chapman and Hall, 1994.
- [88] H. Schneider, M. Walther, C. Schöbein, R. Rehm, J. Fleissner, W. Pletschen, J. Braunstein, P. Koidl, G. Weimann, J. Ziegler and W. Cabanski, "QWIP FPAs for high performance thermal imaging," *Physica E*, vol. 7, pp. 101-107, 2000.

- [89] S. U. Eker, Y. Arslan and C. Besikci, "High speed QWIP FPAs on InP substrates," *Infrared Phys. Technol.*, vol. 54, pp. 209-214, 2011.
- [90] O. O. Cellek, S. Memis, U. Bostanci, S. Ozer and C. Besikci, "Gain and transient photoresponse of quantum well infrared photodetectors: a detailed ensemble Monte Carlo study," *Physica E*, vol. 24, pp. 318-327, 2004.
- [91] B. F. Levine, A. Zussman, J. Kuo and J. J. de, "19  $\mu\text{m}$  cutoff ong-wavelength GaAs/ $\text{Al}_x\text{Ga}_{1-x}\text{As}$  quantum-well infrared photodetectors," *J. Appl. Phys.*, vol. 71, pp. 5130-5135, 1992.
- [92] H. Schneider, C. Mermelstein, R. Rehm, C. Schöbein, A. Sa'ar and M. Walther, "Optically induced electric-field domains by bound-to-continuum transitions in n-type multiple quantum wells," *Phys. Rev. B*, vol. 57, pp. R15096-R15099, 1998.
- [93] R. Rehm, H. Schneider, M. Walther and P. Koidl, "Influence of the recharging process on the dark current noise in quantum-well infrared photodetector," *Appl. Phys. Lett.*, vol. 80, no. 5, pp. 862-864, 2002.
- [94] C. Jelen and M. Razeghi, " $\text{Al}_x\text{Ga}_y\text{In}_{1-x-y}\text{As}/\text{InP}$ -based quantum well infrared photodetectors," *Opto-Electronics Rev.*, vol. 7, pp. 1-17, 1999.
- [95] S. U. Eker, Y. Arslan, A. E. Onuk and C. Besikci, "High Conversion Efficiency InP/InGaAs Strained Quantum Well Infrared Photodetector Focal Plane Array With 9.7  $\mu\text{m}$  Cut-Off for High-Speed Thermal Imaging," *IEEE J. Quantum Electron.*, vol. 46, no. 2, pp. 164-168, Feb. 2010.
- [96] O. O. Cellek and C. Besikci, "Detailed investigation of electron transport, capture and gain in  $\text{Al}_{0.3}\text{Ga}_{0.7}\text{As}/\text{GaAs}$  quantum-well infrared photodetectors," *Semicond. Sci. Technol.*, vol. 19, pp. 183-190, 2004.

- [97] H. Schneider, "Theory of avalanche multiplication and excess noise in quantum-well infrared photodetectors," *Appl. Phys. Lett.*, vol. 82, pp. 4376-4378, 2003.
- [98] J. Jiang, K. Mi, R. McClintock, M. Razeghi, G. J. Brown and C. Jelen, "Demonstration of 256x256 focal plane array based on Al-Free GaInAs-InP QWIP," *IEEE Photon. Technol. Lett.*, vol. 15, no. 9, pp. 1273-1275, 2003.
- [99] O. Celtek, S. Ozer and C. Besikci, "High Responsivity InP/InGaAs Quantum Well Infrared Photodetectors: Characteristics and Focal Plane Array Performance," *IEEE J. Quantum Electron.*, vol. 41, no. 7, pp. 980-985, Jul 2005.
- [100] Y. Arslan, T. Çolakoglu, G. Torunoglu, O. Aktas and C. Besikci, "Enhanced performance QWIP FPAs," *Infrared Phys. Technol.*, vol. 59, pp. 108-111, 2013.
- [101] M. Kaldirim, S. Eker, Y. Arslan and C. Besikci, "Lattice matched AlInAs-InGaAs mid-wavelength infrared QWIPs: characteristics and focal plane array performance," *Semicond. Sci. Technol.*, vol. 23, no. 085007, 2008.
- [102] V. Trinité, E. Ouerghemmi, V. Guériaux, M. Carras, A. Nedelcu, E. Costard and J. Nagle, "Modelling of electronic transport in Quantum Well Infrared Photodetectors," *Infrared Phy. Technol.*, vol. 54, pp. 204-208, 2011.
- [103] M. Erdtmann, A. Matlis, C. Jelen, M. Razeghi and G. Brown, "High-responsivity GaInAs/InP quantum well infrared photodetectors grown by low-pressure metalorganic chemical vapor deposition," *Proc. SPIE*, vol. 3948, pp. 220-226, 2000.
- [104] A. Cho, "Morphology of Epitaxial Growth of GaAs by a Molecular Beam Method: The Observation of Surface Structures," *J. Appl. Phys.*, vol. 41, p. 2780, 1970.

- [105] M. Kaldırım, "Dual and Single Color Mid-wavelength Infrared Quantum Well Photodetectors," *MSc. Thesis*, Middle East Technical University, Electrical and Electronics Department, 2008.
- [106] S. Franchi, "Molecular beam epitaxy: fundamentals, historical background and future prospects," in *Molecular Beam Epitaxy - From research to mass production*, Waltham, Elsevier, 2013, pp. 1-38.
- [107] J. N. Baillargeon, A. Y. Cho, R. Fischer, P. J. Pearah and K. Y. Cheng, "Electrical characteristics of InP grown by molecular beam epitaxy using a valved phosphorus cracking cell," *J. Vac. Sci. Technol. B*, vol. 12, no. 2, pp. 1106-1109, 1994.
- [108] Y. Arslan, T. Colakoglu and C. Besikci, " Diffraction-Grating-Coupled High Quantum Efficiency InP/InGaAs Quantum Well Infrared Photodetector Focal Plane Array," *IEEE J. Quantum Electron.*, vol. 49, no. 2, pp. 186-195, 2012.
- [109] J. Y. Andersson, L. Lundqvist, Z. F. Paska and K. W. J. Streubel, "Long-wavelength quantum-well infrared detectors based on intersubband transitions in InGaAs/InP quantum wells," *Proc. SPIE*, vol. 1762, pp. 216-226, 1992.
- [110] K. Choi, *The Physics of Quantum Well Infrared Photodetectors*, vol. 7, World Scientific, 1997.
- [111] V. Donchev, J. Bourgoïn and P. Bois, "Dark current through GaAs/AlGaAs multiple quantum wells," *Semicond. Sci. Technol.*, vol. 17, pp. 621-624, 2002.
- [112] D. Rosenfeld and G. Bahir, "A model for the trap-assisted tunneling mechanism in diffused n-p and implanted n+-p HgCdTe photodiodes," *IEEE Trans. Electron Dev.*, vol. 39, no. 7, pp. 1638-1645, 1992.

- [113] L. Gendron, V. Berger, B. Vinter, E. Costard, M. N. A. Carras and P. Bois, "Impact ionization processes in quantum well infrared photodetector structures," *Semicond. Sci. Technol.*, vol. 19, pp. 219-223, 2004.
- [114] R. Rehm, H. Schneider, M. Walther, P. Koidl and G. Weimann, "Avalanche multiplication due to impact ionization in quantum-well infrared photodetectors: a quantitative approach," *Appl. Phys. Lett.*, vol. 82, pp. 2907-2909, 2003.
- [115] B. Aslan, H. C. Liu, A. Bezinger, P. J. Poole, M. Buchanan, R. Rehm and H. Schneider, "High responsivity, dual-band response and intraband avalanche multiplication in InGaAs/InP quantum well photodetectors," *Semicond. Sci. Technol.*, vol. 19, pp. 442-445, 2004.
- [116] P. R. Bratt, S. M. Johnson, D. R. Rhiger, T. Tung, M. H. Kalisher, W. A. Radford, G. A. Garwood and C. A. Cockrum, "Historical perspectives on HgCdTe material and device development at Raytheon Vision Systems," *Proc. SPIE*, vol. 7298, 2009.
- [117] J. Garland, "MBE Growth of Mercury Cadmium Telluride," in *Mercury Cadmium Telluride Growth, Properties and Applications*, P. Capper and J. Garland, Eds., West Sussex, Wiley, 2011, pp. 131-151.
- [118] R. H. Sewell, "Investigation of mercury cadmium telluride heterostructures grown by molecular beam epitaxy," *PhD. Dissertation*, University of Western Australia, Electrical - Electronic and Computer Engineering, 2005.
- [119] V. Srivastav, R. Pal and H. P. Vyas, "Overview of etching technologies used for HgCdTe," *Opto-Electron. Rev.*, vol. 13, no. 3, pp. 197-211, 2005.

- [120] A. Causier, I. Gerard, M. Bouttemy, A. Etcheberry, C. Pautet, J. Baylet and L. Mollard, "Wet Etching of HgCdTe in Aqueous Bromine Solutions: a Quantitative Chemical Approach," *J. Electron. Mater.*, vol. 40, no. 8, pp. 1823-1829, 2011.
- [121] H. Koçer, "Numerical Modeling and Optimization of HgCdTe Infrared Photodetectors for Thermal Imaging," *PhD Dissertation*, Middle East Technical University, Electrical and Electronics Engineering, 2011.
- [122] H. Kocer, Y. Arslan and C. Besikci, "Numerical analysis of long wavelength infrared HgCdTe photodiodes," *Infrared Phys. Technol.*, vol. 55, pp. 49-55, 2012.
- [123] M. Karimi, M. Kalafi and A. Asgari, "Numerical optimization of an extracted HgCdTe IR-photodiodes for 10.6  $\mu\text{m}$  spectral region operating at room temperature," *Microelectron. J.*, vol. 38, pp. 216-221, 2007.
- [124] F. Guellec, S. Dubois, E. de Borniol, P. Castelein, S. Martin, R. Guiguet, M. Tchagaspanian, A. Rouvie and P. Bois, "A low-noise, 15  $\mu\text{m}$  pixel-pitch, 640x512 hybrid InGaAs image sensor for night vision," *Proc. SPIE*, vol. 8298, pp. 82980c-1-8, 2012.
- [125] A. Hood, M. H. MacDougal, J. Manzo, D. Follman and J. C. Geske, "Large-format InGaAs focal plane arrays for SWIR imaging," *Proc. SPIE*, vol. 8353, pp. 83530A-1-7, 2012.
- [126] H. Yuan, M. Meixell, J. Zhang, P. Bey, J. Kimchi and L. C. Kilmer, "Low Dark Current Small Pixel Large Format InGaAs 2D Photodetector Array Development at Teledyne Judson Technologies," *Proc. SPIE*, vol. 8353, pp. 835309-1-8, 2012.
- [127] J. Nazemi, J. Battaglia, R. Brubaker, M. Delamere and C. Martin, "A Low Power TEC-less 1280x1024 Compact SWIR Camera with Temperature Dependent Non-Uniformity Corrections," *Proc. SPIE*, vol. 8353, pp. 83530B1-10, 2012.

- [128] T. Li, J. Cheng, X. Shao, H. Deng, Y. Chen, H. Tang, X. Li and H. Gong, "Performance of Low Dark Current InGaAs Shortwave Infrared Detector," *Proc. SPIE*, vol. 8419, pp. 841907-1-6, 2012.
- [129] R. U. Martinelli, T. J. Zamerowski and P. A. Longeway, "2.6  $\mu\text{m}$  InGaAs photodiodes," *Appl. Phys. Lett.*, vol. 53, pp. 989-991, 1988.
- [130] G. H. Olsen, A. M. Joshi, S. Mason, K. M. Woodruff, E. Mykietyn, V. S. Ban, M. J. Lange, J. Hladky, G. C. Erickson and G. A. Gasparian, "Room-temperature InGaAs detector arrays for 2.5  $\mu\text{m}$ ," *Proc. SPIE*, vol. 1157, pp. 276-282, 1989.
- [131] K. R. Linga, G. H. Olsen, V. S. Ban, A. M. Joshi and W. F. Kosonocky, "Dark Current Analysis and Characterization of  $\text{In}_x\text{Ga}_{1-x}\text{As}/\text{InAs}_y\text{P}_{1-y}$  Graded Photodiodes with  $x > 0.53$  for Response to Longer Wavelengths ( $> 1.7 \mu\text{m}$ )," *J. lightwave Technol.*, vol. 10, pp. 1050-1055, 1992.
- [132] A. M. Joshi, G. H. Olsen, S. Mason, M. Lange and V. S. Ban, "Near-Infrared (1-3  $\mu\text{m}$ ) InGaAs detectors and arrays: crystal growth, leakage current and reliability," *Proc. SPIE*, vol. 1715, pp. 585-593, 1992.
- [133] R. Kochhar, W. Y. Hwang, M. Micovic, T. S. Mayer, D. L. Miller and S. M. Lord, "Development of 2.2- $\mu\text{m}$  InGaAs photodetectors using molecular beam epitaxy," in *Lasers and Electro-Optics*, Anaheim, CA, USA, 1996.
- [134] M. D'Hondt, I. Moerman, P. V. Daele and P. Demeester, "Influence of buffer layer and processing on the dark current of 2.5  $\mu\text{m}$  wavelength 2% mismatched InGaAs photodetectors," *IEE Proc.: Optoelectron*, vol. 144, pp. 277-282, 1997.
- [135] M. D'Hondt, I. Moerman and P. Demeester, "Dark current optimisation of 2.5  $\mu\text{m}$  wavelength, 2% mismatched InGaAs photodetectors on InP," in *10th Intern. Conf. on Indium Phosphide and Related Materials*, Tsukuba, Japan, 1998.

- [136] M. J. Nelson, M. F. Skrutskie, S. Kanneganti and C. Park, "High sensitivity infrared extended wavelength response InGaAs detectors," *Proc. SPIE*, vol. 7021, 2008.
- [137] T. Zhao-Bing, G. Yi, W. Kai and Z. Yong-Gang, "Gas source MBE-grown metamorphic InGaAs photodetectors using InAlAs buffer and caplayers with cut-off wavelength up to 2.7  $\mu\text{m}$ ," *Chin. Phys. Lett.*, vol. 25, pp. 2292-2295, 2008.
- [138] H. Yuan, G. Apgar, J. Kim, J. Laquindanum, V. Nalavade, P. Beer, J. Kimchi and T. Wong, "FPA development: from InGaAs, InSb, to HgCdTe," *Proc. SPIE*, vol. 6940, pp. 69403C-1-11, 2008.
- [139] C. Li, Y. Zhang, K. Wang, Y. Gu, H. Li and Y. Li, "Distinction investigation of InGaAs photodetectors cutoff at 2.9  $\mu\text{m}$ ," *Infrared Phys. Technol.*, vol. 53, pp. 173-176, 2010.
- [140] T. Li, S. Deng, X. Li, X. Shao, H. Tang and H. Gong, "Responsivity Performance of Extended Wavelength InGaAs Shortwave Infrared Detector Arrays," *Proc. SPIE*, vol. 9100, pp. 9100U-1-7, 2014.
- [141] Y. Nemirovsky and A. Unikovsky, "Tunneling and 1/f noise currents in HgCdTe photodiodes," *J. Vac. Sci. Technol. B*, vol. 10, pp. 1602-1610, 1992.
- [142] J. E. Ayers and S. K. Ghandi, "Crystallographic tilting of heteroepitaxial layers," *J. Cryst. Growth*, vol. 113, pp. 430-440, 1991.
- [143] D. Kim, S. R. Forrest, M. J. Lange, M. J. Cohen, G. H. Olsen, R. J. Menna and R. J. Paff, "Study of  $\text{In}_x\text{Ga}_{1-x}\text{As}/\text{InAs}_y\text{P}_{1-y}$  structures lattice mismatched to InP substrates.," *J. Appl. Phys.*, vol. 80, pp. 6229-6234, 1996.

- [144] M. Shi, X. Shao, H. Tang, T. Li, Y. Wang, X. Li and H. Gong, "Inductively coupled plasma chemical vapor deposition silicon nitride for passivation of  $\text{In}_{0.83}\text{Ga}_{0.17}\text{As}$  photodiodes," *Infrared Phys. Technol.*, vol. 67, pp. 197-201, 2014.
- [145] S. M. Johnson, D. R. Rhiger, J. P. Rosbeck, J. M. Peterson, S. M. Taylor and M. E. Boyd, "Effect of dislocations on the electrical and optical properties of long-wavelength infrared HgCdTe photovoltaic detectors," *J. Vac. Sci. Technol. B*, vol. 10, pp. 1499-1506, 1992.
- [146] R. W. M. Hoogeveen, R. J. van der A and A. P. H. Goede, "Extended wavelength InGaAs infrared (1.0-2.4  $\mu\text{m}$ ) detector arrays on SCIAMACHY for space-based spectrometry of the Earth atmosphere," *Infrared Phys. Technol.*, vol. 42, pp. 1-16, 2001.
- [147] V. Gopal and S. Gupta, "Effect of dislocations on the zero-bias resistance-area product, quantum efficiency, and spectral response of LWIR HgCdTe photovoltaic detectors," *IEEE Trans. Electron Devices*, vol. 50, pp. 1220-1226, 2003.
- [148] L. G. Hipwood, N. Shorrocks, C. Maxey, D. Atkinson and N. Bezawada, "SWIR and NIR MCT arrays grown by MOVPE for astronomy applications," *Proc. SPIE*, vol. 8353, pp. 83532M-1-8, 2012.



## CURRICULUM VITAE

### PERSONAL INFORMATION

Surname, Name: Arslan, Yetkin  
Nationality: Turkish (TC)  
Date and Place of Birth: 15 February 1985, İstanbul  
Marital Status: Married to Irmak Özgür Arslan  
Phone: +90 312 210 45 33  
Fax: +90 312 210 12 61  
e-mail: yetkin.arslan@gmail.com

### EDUCATION

Degree	Institution	Year of Graduation
MS	METU Electrical and Electronics Engineering	2009
BS	METU Electrical and Electronics Engineering	2007
High School	İstanbul Atatürk Fen Lisesi, İstanbul	2003

### WORK EXPERIENCE

Year	Place	Enrollment
2006-Present	METU Department of Electrical and Electronics Engineering	Research Engineer

### FOREIGN LANGUAGES

Advanced English, French

### SELECTED (JOURNAL) PUBLICATIONS

1. Y. Arslan, F. Oguz, C. Beşikci, "640x512 Extended Short Wavelength Infrared  $\text{In}_{0.83}\text{Ga}_{0.17}\text{As}$  Focal Plane Array", Submitted for publication, 2014.

2. Y. Arslan, F. Oguz, C. Beşikci, "Extended Wavelength SWIR InGaAs Focal Plane Array: Characteristics and Limitations," Submitted for publication, 2014.
3. Y. Arslan, T. Colakoglu, and C. Besikci, "Diffraction-Grating-Coupled High Quantum Efficiency InP/InGaAs Quantum Well Infrared Photodetector Focal Plane Array," *IEEE J. Quantum Electron.*, vol. 49, no. 2, pp. 186-195, 2013.
4. Y. Arslan, T. Çolakoglu, G. Torunoglu, O. Aktas, and C. Besikci, "Enhanced performance QWIP FPAs," *Infrared Phys. Technol.*, vol. 59, pp. 108-111, 2013.
5. H. Koçer Y. Arslan and C. Beşikci, "Numerical Analysis of Long Wavelength Infrared HgCdTe Photodiodes", *Infrared Phys. Technol.*, vol. 55, pp. 49-55, 2012.
6. S. U. Eker, Y. Arslan, and C. Besikci, "High speed QWIP FPAs on InP substrates," *Infrared Phys. Technol.*, vol. 54, pp. 209-214, 2011.
7. S. U. Eker, Y. Arslan, A. E. Onuk and C. Beşikci, "High Conversion efficiency InP/InGaAs Strained Quantum Well Infrared Photodetector Focal Plane Array with 9.7  $\mu\text{m}$  Cut-off for High Speed Thermal Imaging", *IEEE J. Quantum Electron.*, vol. 46, no. 2, pp. 164-168, Feb. 2010.
8. S. U. Eker, Y. Arslan, M. Kaldırım, and C. Besikci, "QWIP FPAs on InP Substrates for Single and Dual Band Thermal Imagers," *Infrared Phys. Technol.*, vol. 52, 385-390 2009
9. Y. Arslan, S. U. Eker, M. Kaldırım and C. Besikci, "Large Format Voltage Tunable Dual-Band QWIP FPAs", *Infrared Phys. Technol.*, vol 52, pp.399-402, 2009
10. S. U. Eker, M. Kaldırım, Y. Arslan and C. Besikci, "Large-Format Voltage-Tunable Dual-Band Quantum-Well Infrared Photodetector Focal Plane Array for Third-Generation Thermal Imagers," *IEEE Electron Device Lett.*, vol. 29, no. 10, pp. 1121-1123, 2008.
11. M. Kaldırım, Y. Arslan, S. U. Eker and C. Beşikci, "Lattice-matched AlInAs-InGaAs mid-wavelength infrared QWIPs: characteristics and focal plane array performance," *Semicond. Sci. Technol.*, vol. 23, 085007, 2008.
12. M. Kaldırım, S. U. Eker, Y. Arslan, U. Tumkaya and C. Besikci, "Large Format Voltage Tunable Dual Color Midwavelength Infrared Quantum Well Infrared Photodetector Focal Plane Array", *IEEE Photonics Technol. Lett.*, vol. 20, pp.709-711, 2008

## HOBBIES

Sports, Reading, Sightseeing